Characterisation of the Lithium-Solid Electrolyte Interface in Solid State Batteries



Yvonne Antonia Chart

Linacre College

University of Oxford

A thesis submitted for the degree of

Doctor of Philosophy

Michaelmas 2024

This thesis is dedicated to my parents,
Marjorie Mascolino and Richard Chart,
for always believing in me even when I don't believe in myself.

To my sister Maria Chart,
for being the greatest cheerleader and partner in crime I could have ever asked for.

And to Paul Caine and John Knowles,
for encouraging me to excel both athletically and academically.

I hope I have made you proud.

Acknowledgements

I would like to thank my supervisor Mauro Pasta, for giving me the opportunity to work in such a prestigious and well-funded lab and for his helpful input throughout my DPhil. I have learned so much and am so grateful for the opportunities joining this group has afforded me. I would also like to thank Johannes Ihli, for going above and beyond to support myself and others within the group. This thesis would certainly be of significantly lower quality, if it was completed at all, without your encouragement and guidance. In addition, I would like to thank the others who have taken the time to give me feedback on this thesis, your thoughts have been invaluable: Matthew Burton, Christopher Allen, Yige Sun, and Jack Aspinall.

Working with the Pasta group has provided me with a number of opportunities that I would never have otherwise experienced. I would like to thank each and every group member I have worked with over the last four years, you have made these past 4 years infinitely better and I feel so lucky to have been able to meet you. In particular I would like to thank Zack Brown, Jack Fawdon, and Isaac Capone for taking me under your wings during my first year. I appreciate your efforts to guide my research journey while navigating the difficulties of COVID! Sudarshan Narayanan and Soochan Kim provided later support and encouragement, including allowing me to contribute to your work, seeing you in the lab always made my day brighter. Junhao Li and Hua Guo, I enjoyed working on the LiSTAR project with you. From overly-delicate thin solid electrolytes to perfecting ratios in S cathodes, your systematic approach to research taught me so much. Thank you to Hyeon Jeong Lee and Xiaoxiao Liu for inviting me to contribute to your work on solid-state cathodes, it was interesting to work on a project in a slightly different area of batteries! Stephen Turrell, thank you for being my desk buddy and putting up with the constantly expanding piles of papers on my desk. Your scientific insights and calm demeanour made everything feel much more manageable.

To my fellow DPhils in the Pasta group, thank you for making each day a little bit better than it would have otherwise been. Giulia - thank you for being a wonderful friend and genuine source of positive energy; we will play tennis together one day finally! Shobhan - thank you for encouraging us all to be a bit more social and your encouragement to work with OCS, it was genuinely a highlight of my Oxford experience. Max - you are one of the kindest people I have met, I am so

glad we got to work together and I only wish we had had more time hanging out and less working! Jack - I always appreciate you checking in and your enthusiasm for science; I look forward to seeing you get Arabella into running too! Brigita - thank you for the lovely chats, I always appreciate your sense of humour. Po-Yuan - thank you for suffering through microscopy with me, I look forward to never seeing each on microscopes at 1 am again. Yi - thank you for being such a good friend, it's been a tough 4 years but we've gotten through together. Lorenz - your drive and enthusiasm are inspirational, best of luck taking on the world, if anyone can do it you can. Emily - you are a great friend, thank you for being you and for being in my life. Yiming - thank you for your help and support over the last year, you're going to have a great DPhil.

Deep thanks to all those at the DCCEM in Oxford, Gareth Hughes, Neil Young, Graham Wyatt, Ian Griffiths, and Phani Karamched. Numerous times I have come to you with questions, concerns, or just a chat, whether scientific or about life in general, I can always rely on you to help despite the heavy demands on your time. You have all truly made a difference in my PhD experience and I will always remember our coffee chats in the Holder cafe.

On a similar note, to Christopher Allen and Jinseok Ryu at ePSIC, we did not work together for long but I have learned so much from you. Your constant patience and kindness as I tried to speed-learn 4D-STEM analysis reminded me how wonderful scientists can be and allowed me to be comfortable asking clarifying questions.

Thank you to Esther Townsend for being a great friend and for keeping the lab running. I know how thankless it can be but you do a great job.

Thank you to the Faraday Institution for funding my DPhil and providing me with the opportunities to broaden my horizons beyond the narrow scope of what I specifically am studying. I am particularly grateful to my cohort, seeing you all at the trainings was a highlight of the DPhil and always left me feeling far more energised when I had to go back. I would particularly like to thank the LiSTARs: Georgia, Tayeba, Sam, and Lizzy, hanging out at the LiSTAR meetings was always so much fun. In addition, thanks to Halima for her witty comments, support, and occasional lifts back to Oxford. Finally, to Hollie and Rory, for making me laugh across the room with nothing more than a look and being such wonderful friends. I am grateful for you all.

Outside of batteries, I would like to thank OUFC for being a home-away-from-home and distracting me from DPhil work. In particular, thanks to W1, my champion ladies, going undefeated in the league three years in a row was amazing, even if it meant I had to swing around a sabre.

Finally, and most importantly, I would like to thank my family. For all the love, support, and encouragement you have provided over the years. I would not

be who I am today or have made it through this degree without you. Mom and Dad - you are my greatest support system and I am infinitely grateful for all you have done for me over the years. Maria - my baby sister and biggest cheerleader, thank you for keeping my grounded and encouraging me to look after myself. Will - my rock, the best thing to have happened to me over these past 4 years. I am so lucky to have met you and have you in my life. Thank you for being there for me through thick and thin. I love you all!

Abstract

All-solid-state batteries (ASSBs) with a Li-metal negative electrode have the potential to drastically improve on state-of-the-art energy densities. Improved understanding failure mechanisms is needed to reach commercialisation, but physical characterisation is challenging. In this thesis, I will investigate the use of electron microscopy as a tool to better understand degradation mechanisms at the interfaces between solid-state electrolytes (SSEs) and Li. First, plasma focused-ion beam (PFIB) and scanning electron microscopy (SEM) are used to access and image the interface between Li-based electrodes and a LI_6PS_5Cl electrolyte with minimal artifact introduction. Li alloys are found to be more stable to ion milling than pure Li, allowing Li-Mg to be used as a characterisation proxy for Li metal, and the microstructure of the Li-In reference electrode to be interpreted. Cryo-PFIB is then used to investigate the Li deposition structure with more complex SSEs; a composite, thin SSE and a SSE combined with a C-Ag interlayer. To investigate the morphology of the thin ($\approx$ 10 - 100s nm), air- and electron-beam- sensitive solid electrolyte interphase (SEI) layer, a sample preparation technique is developed to reliably produce electron-transparent samples incorporating the SSE-SEI-Li interface. This is combined with low-dose 4D-scanning transmission electron microscopy, which enables spatio-compositional mapping of the interface without beam damage. Analysis reveals information on the crystallite size and distribution across the SEI. Statistical analysis of the SEI component spatial relationships demonstrates a complex structure with component intermixing. This is also shown to be the case with $Li_{5.5}PS_{4.5}Cl_{0.75}Br_{0.75}$ (LPSClBr), despite the differing morphology leading to smaller SEI component domain sizes. This information helps better understand the degradation processes at ASSB interfaces and, in particular, enables improved characterisation of the SEI.

Publication List

1. Chart, Y. A., Ihli, J., Ryu, J., Liang, Y., Huang, P., Hopkinson, D., Hughes, G., Xu, Y., Allen, C., Pasta, M. Spatio-Compositional Characterization of the Solid Electrolyte Interphase in Solid-State Batteries via Nanobeam Electron Diffraction *In preparation.*

   Content from this paper makes up Chapters 4 and 5.

2. Guo, H., Li, Burton, M., J., Cattermull, J., Liang, Y., Chart, Y. A., Rees, G., Aspinall, J., Pasta, M. High-entropy sulphide argyrodite electrolytes for all-solid-state lithium-sulfur batteries. *Cell Reports Physical Science* **102228** (2024).

3. Chart, Y. A., Aspinall, J., Pasta, M. 6| Zero-Excess Lithium Batteries - 2024 Sustainable Batteries Roadmap. Titirici, M., Johansson, P. et al. *Journal of Physics: Energy* **6**, 041502 (2024).

4. Aspinall, J., Sada, K., Guo, H., Kotakadi, S., Narayanan, S., Chart, Y. A., Jagger, B., Milan, E., Brassart, L., Armstrong, D., Pasta, M. The impact of magnesium content on lithium-magnesium alloy electrode performance with argyrodite solid electrolyte. *Nature Communications* **15**, 4511 (2024).

   Candidate contributions to this paper are included in Chapter 3.

5. Li, J.*, Kim, S.*, Mezzomo, L.*, Chart, Y. A., Aspinall, J., Ruffo, R., Pasta, M. Processing-structure-property relationships in practical thin solid-electrolyte separator for all-solid-state batteries. *Journal of Physics: Energy* **6**, 025023 (2024).

6. Aspinall, J., Chart, Y. A., Guo, H., Pasta, M. Microstructure optimisation of indium lithium alloys as a counter and reference electrode for solid-state batteries. *ACS Energy Letters* **9**, 578-585 (2023).

   Candidate contributions to this paper are included in Chapter 3.

7. Galatolo, G., Alshangiti, O., Di Mino, C., Matthews, G., Xiao, A., Rees, G., Chart, Y. A., Olbrich, Lorenz F., Pasta, M. Advancing fluoride-ion batteries with a Pb-PbF_2 counter electrode and a diluted liquid electrolyte. *ACS Energy Letters* **9**, 85-92 (2023).

8. Darminto, B., Rees, G., Catermull, J., Hashi, K., Diaz-Lopez, M., Kuwata, N., Turrell, S., Milan, E., Chart, Y. A., Di Mino, C., Lee, H. J., Goodwin A., Pasta, M. On the Origin of the Non-Arrhenius Na-ion Conductivity in Na_3OBr. *Angewandte Chemie Inernational Edition* **135**, 51 (2023).

9. Kim, S., Chart, Y. A., Narayanan, S., Pasta, M. Thin Solid Electrolyte Separators for Solid-State Lithium-Sulfur Batteries. *NanoLetters* **22**, 10176-10183 (2022).

   Candidate contributions to this paper are included in Chapter 3.

10. Narayanan, S., Ulissis, U., Gibson, J. S., Chart, Y. A., Weatherup, R. S., Pasta, M. Effect of current density on the solid electrolyte interphase formation at the lithium-Li_6PS_5Cl interface. *Nature Communications* **13**, 7237 (2022).

11. Lee, H. J., Liu, X., Chart, Y. A., Teng, P., Bae, J-G., Narayanan, S., Lee, J. H., Potter, R. J., Sun, Y., Pasta, M. $LiNi_{0.5}Mn_{1.5}O_4$ Cathode Microstructure for All-Solid-State Batteries. *NanoLetters* **22**, 7477-7483 (2022).

12. Lee, H. J., Darminto, B., Narayanan, S., Diaz-Lopez, M., Xiao, A. W., Chart, Y. A., Lee, J. H., Dawson, J. A., Pasta, M. Li-ion conductivity in $Li_2OHCl_{1-x}Br_x$ solid electrolytes: grains, grain boundaries and interfaces. *Journal of Materials Chemistry A* **10**, 11574 (2022).

Candidate confirms that the contributions stated above are accurate and all work done in the following thesis is her own unless stated otherwise.

Contents

Publication List **xi**

1 Introduction and Background **1**
1.1 Motivation . . . 2
1.2 Battery Context . . . 3
1.2.1 Battery Fundamentals . . . 3
1.2.2 Battery Metrics . . . 6
1.2.3 Battery Materials . . . 8
1.3 Lithium Metal Anodes . . . 10
1.3.1 Dendrite Nucleation and Growth . . . 11
1.3.2 Solid Electrolyte Interphase . . . 14
1.3.3 Performance Improvements . . . 17
1.4 Solid-state Batteries . . . 21
1.4.1 Solid-State Electrolyte Materials . . . 21
1.4.2 Areas for Future Work . . . 25
1.5 Characterisation of the Li-SSE Interface . . . 26
1.5.1 Limitations of Electrochemical Characterisation . . . 26
1.5.2 Sample Preparation Challenges . . . 27
1.5.3 Morphological Characterisation . . . 28
1.5.4 Compositional Characterisation . . . 31
1.6 Thesis Objectives . . . 34

2 Methods Fundamentals **37**
2.1 Electron Microscopy . . . 38
2.1.1 Optics . . . 38
2.1.2 Scanning Electron Microscopy . . . 40
2.1.3 Transmission Electron Microscopy . . . 43
2.1.4 Energy Dispersive X-ray Analysis . . . 46
2.1.5 Focused Ion Beam Microscopy . . . 47
2.1.6 Cryogenic Microsocopy . . . 51
2.1.7 Beam Damage . . . 52
2.2 X-Ray Techniques . . . 55

2.2.1 X-Ray Diffraction 55
2.2.2 X-Ray Photoelectron Spectroscopy 56
2.3 Electrochemical Techniques 56
2.3.1 Electrochemical Impedance Spectroscopy 56
2.3.2 Chronopotiometry 57

3 Insights into the Solid Electrolyte - Li-based Electrode Interface from Plasma Focused-Ion Beam Microscopy 59
3.1 Abstract 60
3.2 Introduction 60
3.3 Results and Discussion 63
3.3.1 Li-Mg Alloy: Alternative to Li metal? 63
3.3.2 Li-Mg - Solid Electrolyte Interface 67
3.3.3 Microstructural Changes in Li-In Alloys 72
3.3.4 Developing Thin Solid Electrolytes 78
3.3.5 Effect of Interlayers and Temperature on Li morphology . . 84
3.4 Conclusion 87
3.5 Experimental Detail 88
3.5.1 Plasma Focused Ion Beam - Scanning Electron Microscopy . 88
3.5.2 Energy Dispersive X-Ray Spectroscopy 89
3.5.3 Transmission Electron Microscopy 89
3.5.4 Sample Preparation 89

4 Technique Development for Nano-structural Analysis of the Li-Solid Electrolyte Interphase in Solid State Batteries 93
4.1 Abstract 94
4.2 Introduction 94
4.3 Results and Discussion 95
4.3.1 Sample Extraction 95
4.3.2 Sample Thinning 100
4.3.3 Microscope Workflow 103
4.3.4 4D-STEM Validation 104
4.4 Conclusion 108
4.5 Experimental Detail 109
4.5.1 Materials 109
4.5.2 Cell Preparation 109
4.5.3 Electrochemistry 110
4.5.4 Focused-Ion Beam Thinning 110
4.5.5 4D-STEM 110

5 Characterisation of the Li-Solid Electrolyte Interphase formed with Sulphide Argyrodites **113**
5.1 Abstract . . . 114
5.2 Introduction . . . 114
5.3 Results and Discussion . . . 116
5.3.1 Set-up and Calibration . . . 116
5.3.2 Component Matching . . . 116
5.3.3 Algorithm Choice . . . 119
5.3.4 Spatial and Compositional Analysis . . . 121
5.3.5 Comparison with LPSClBr . . . 125
5.4 Conclusion . . . 127
5.5 Experimental Details . . . 127
5.5.1 Materials . . . 127
5.5.2 Sample Preparation . . . 128
5.5.3 4D-Scanning Transmission Electron Microscopy . . . 129
5.5.4 Calibration . . . 129
5.5.5 Electron Diffraction Image Analysis . . . 129
5.5.6 Virtual Electrode Plating - X-Ray Photoelectron Spectroscopy (VEP - XPS) . . . 131

6 Conclusions and Future Work **133**
6.1 Conclusions . . . 133
6.2 Future Work . . . 134

Appendices

A 4D-STEM Analysis code **139**
A.1 1D Spectrum Matching Algorithm . . . 140
A.2 Spatial Separation Analysis Algorithm . . . 148

References **169**

Acronyms

AFM Atomic Force Microscopy

AOI Area of interest

ASSBs All-solid-state batteries

BCC Body-centred cubic

BE Binding energy

BF Bright Field

BSE Back-scattered electrons

CBED Convergent-Beam Electron Diffraction

CC Current collector

CCD Critical Current Density

CE Coulombic Efficiency

CEI Cathode electrolyte interphase

CTTA Coulometric Titration Time Analysis

CV Cyclic Voltammetry

DBSCAN Density-Based Spatial Clustering of Applications with Noise

DF Dark Field

DFT Density Functional Theory

DP Diffraction pattern

EBSD Electron Backscatter Diffraction Spectroscopy

EDX Energy Dispersive X-ray Spectroscopy

EELS Electron Energy Loss Spectroscopy

EIS Electrochemical Impedance Spectroscopy

EM Electron microscopy

ESW Electrochemical Stability Window

FFT Fast Fourier Transform

FIB Focused-Ion Beam

FOV field of view

GIS Gas Injection System

HAADF High-angle annular dark field

HCEs Highly concentrated electrolytes

ICP Inductively Coupled Plasma

LAGP $Li_{1.4}Al_{0.4}Ge_{1.6}(PO_4)_3$

LCO $LiCoO_2$

LFP $LiFePO_4$

LGPS $Li_{10}GeP_2S_{12}$

LHCEs Locally highly concentrated electrolytes

LiPON Lithium phosphorous oxynitride

LLZO $Li_7La_3Zr_2O_{12}$

LMIS Liquid Metal Ion Source

LMO $LiMn_2O_4$

LNMO $LiNi_{0.5}M_{1.5}O_4$

LPS $Li_7P_3S_{11}$

LPSCl Li_6PS_5Cl

LPSClBr $Li_{5.5}PS_{4.5}Cl_{0.75}Br_{0.75}$

MCI Mixed-Conducting Interphase

MD Molecular Dynamics

NBED Nano-Beam Electron Diffraction

NCA $LiNi_xCo_yAl_zO_2$

NMC $LiNi_xMn_yCo_zO_2$

NMF Non-negative matrix factorisation

NMR Nuclear Magnetic Resonance

OCV Open Current Voltage

OPTICS Ordering points to identify the clustering structure

PCA Principal component analysis

PEEK Polyether ether ketone

PEO Polyethylene oxide

PFIB Plasma Focused-Ion Beam

PVdF Polyvinylidene fluoride

R Range

$\mathbf{R}_p$ Projected Range

S(E) Stopping Power

SAED Selected Area Electron Diffraction

SE Secondary electrons

SEI Solid Electrolyte Interphase

SEM Scanning electron microscopy

SHE Standard hydrogen electrode

SI Secondary Ion

SSE Solid State Electrolyte

STEM Scanning Transmission Electron Microscopy

TEM Transmission Electron Microscopy

ToF-SIMS Time of Flight - Secondary Ion Mass Spectrometry

TSE Thin Solid Electrolyte

UHV Ultra high vacuum

X_s Implantation Depth

XNBR Carboxylated nitrile butadiene rubber

XPS X-Ray photoelectron spectroscopy

XRD X-Ray diffraction

XRT X-Ray Tomography

Z Atomic number

Science is about asking the right questions, not just accepting the easy answers.

— Rosalind Franklin, Chemist and Crystallographer

1 Introduction and Background

Contents

1.1 Motivation 2
1.2 Battery Context 3
1.2.1 Battery Fundamentals 3
1.2.2 Battery Metrics 6
1.2.3 Battery Materials 8
1.3 Lithium Metal Anodes 10
1.3.1 Dendrite Nucleation and Growth 11
1.3.2 Solid Electrolyte Interphase 14
1.3.3 Performance Improvements 17
1.4 Solid-state Batteries 21
1.4.1 Solid-State Electrolyte Materials 21
1.4.2 Areas for Future Work 25
1.5 Characterisation of the Li-SSE Interface 26
1.5.1 Limitations of Electrochemical Characterisation 26
1.5.2 Sample Preparation Challenges 27
1.5.3 Morphological Characterisation 28
1.5.4 Compositional Characterisation 31
1.6 Thesis Objectives 34

1.1 Motivation

This thesis focuses on the characterisation of the Lithium (Li) - Solid State Electrolyte (SSE) interface in All-solid-state batteries (ASSBs). Batteries are key to combating climate change due to their potential to reduce the use of fossil fuels. They enable intermittent renewable energy sources by balancing the grid [1] and electric transportation powered by the same clean sources. [2, 3] While Li-ion batteries have already been applied in these applications, they are reaching the practical limits of energy density. New chemistries are required to achieve the electric vehicle ranges desired by users.[2, 4] Li metal has long been suggested to be the "holy grail" of battery technology due to its high specific capacity of 3862 mAh g^{-1}, while SSEs have been touted as the enabling factor by removing the highly flammable liquid electrolyte and mechanically preventing the growth of dendrites, which lead to disastrous short-circuits. However, solid-state Li metal batteries have not yet seen wide application. To understand why they have not reached their full potential, intense characterisation efforts are required, including the development of novel techniques.

This chapter provides the necessary background to delve into the characterisation of the Li-Solid Electrolyte Interphase (SEI) in ASSBs. Initially, context around the electrochemistry of batteries is given. This is followed by an introduction into the potential impact Li metal and ASSBs could have and why they have not yet been widely implemented. Finally, the difficulties surrounding the characterisation of Li metal and ASSBs are explored, with a particular focus on physical characterisation of their failure mechanisms.

1.2 Battery Context

This section will provide the necessary context to the batteries being investigated in this thesis. It will start with a discussion of some of the fundamentals of battery science, before moving into some of the more practical metrics used to compare battery performance. Finally, it will briefly summarise some common battery materials.

1.2.1 Battery Fundamentals

A battery is an electrochemical storage device which consists of a series of electrochemical cells. These cells contain a positive and negative electrode, commonly referred to as the cathode and anode respectively, with an electrolyte between them. This is shown schematically in Figure 1.1. In Li-ion batteries, one Li^+ ion crosses the electrolyte for each electron which travels around an external circuit. On discharge, Li is oxidised at the anode, Li^+ ions travel across the electrolyte and are reduced at the cathode.[5] Therefore, two half-reactions occur in a battery cell, separated by an electrolyte. Equations 1.1 and 1.2 show a pair of generalised half reactions in a Li-ion battery at the negative and positive electrode, respectively, during discharge.

$$LiC_6 \rightarrow Li^+ + e^- + 6C \tag{1.1}$$

$$Li_{(1-x)}MO_2 + xe^- + xLi^+ \rightarrow LiMO_2 \tag{1.2}$$

Where M is a generalised transition metal or metals. Note that the two equations are not balanced with each other because the positive electrodes generally cannot be charged to the extent that they do not contain any Li because this damages their crystal structure, leading to irreversible capacity loss.

The theoretical cell potential is the driving force behind the two half reactions taking place in the cell, also referred to as the cell voltage. It is related to the change in the Gibbs Free Energy (ΔG^0) between the reactants and products of the reaction, as a reaction with a negative ΔG^0 will be spontaneous and drive electrons around the external circuit. By dividing ΔG^0 by z, the number of electrons

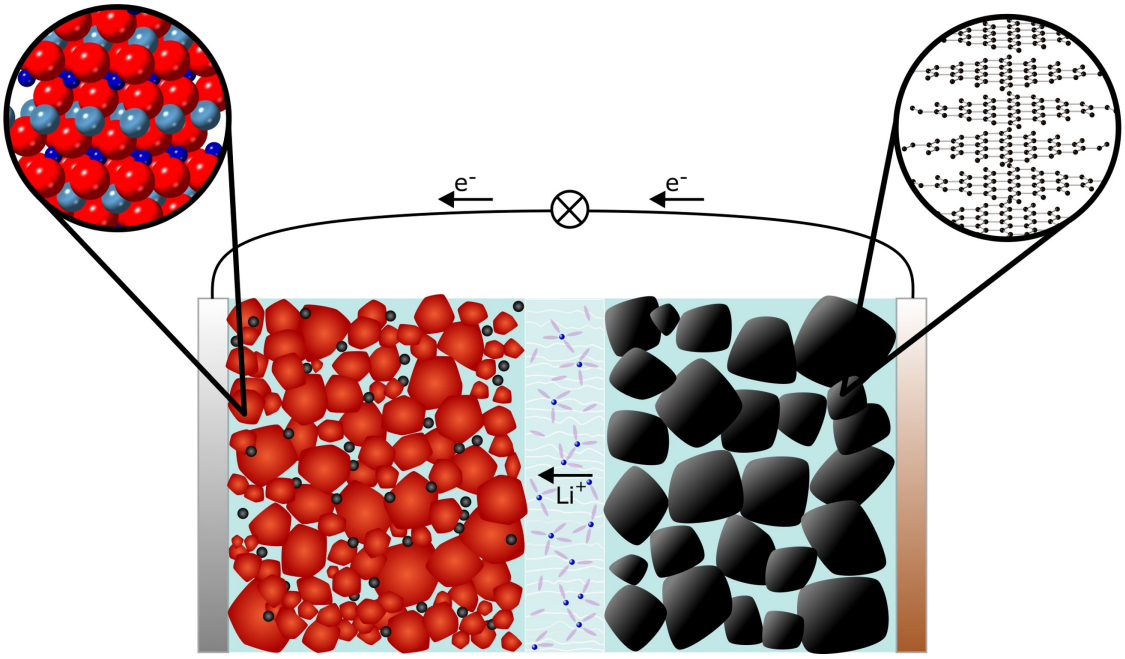


Figure 1.1: Schematic of Li-ion battery cell undergoing discharge. The negative electrode is shown on the right and the positive on the left. The structures of graphite and $LiCoO_2$ (LCO) are shown in detail in bubbles as example of materials for each electrode, respectively. The blue background represents a liquid electrolyte, with the purple ovals representing solvent molecules which bind to the Li^+ ions. The electrolyte facilitates ion transport, while an external electronic circuit transports electrons. The pale area in the centre represents the separator (often polypropylene or polyethylene) which prevents direct electrical contact between the electrodes. The direction of the Li^+ and e^- shows the cell in discharge.

transferred in the reaction, and F, the Faraday constant (96,500 C mol$^-$1), you get the potential of the equation, as shown in Equation 1.3.

$$\Delta G^0 = G^0_{reactants} - G^0_{products} = -zFE^0_{cell} \tag{1.3}$$

The theoretical cell potential is what would be expected under standard, equilibrium conditions (298 K, 1 atm, 1 M). To calculate the cell potential under non-standard conditions the Nernst equation can be used, which is shown in Equation 1.4. This incorporates the temperature, T, the universal gas constant, R (8.314 J mol C^{-1}), and the reaction quotient, Q. The reaction quotient is the activity, or effective concentration, of the reactants divided by the activity of the products. Note that potentials must always be measured relative to a standard, generally the potential of a half reaction is measured relative to the Standard hydrogen electrode

(SHE). Within a battery cell, the electrodes will either be measured relative to each other or to stable reference electrodes.

$$E_{cell} = E^0_{cell} - \frac{RT}{zF} lnQ \tag{1.4}$$

While the Nernst equation calculates the driving force for the reaction to occur, its relation to the rate of reaction via kinetics is determine by using the Butler-Volmer equation shown in Equation 1.5. This equation relates the current density, i, which is effectively the same as the rate of reaction, to the charge transfer coefficients (α) and the activation overpotential ($E - E_0$, sometimes written as η). The two parts of the equation are the effects from the anode and cathode, denoted by subscripts a and c, respectively. The i_0 term is the exchange current coefficient, which is equivalent to a rate constant, a high i_0 value will mean that the reaction can occur quickly.

$$i = i_0[exp(\frac{\alpha_a zF}{RT}(E - E^0)) - exp(-\frac{\alpha_c zF}{RT}(E - E^0))] \tag{1.5}$$

The activation overpotential described above is the potential required to overcome the activation energy of the reaction, also sometimes called the surface overpotential. An overpotential is something which causes the actual potential of the cell to deviate from the theoretical value. Alongside the activation overpotential, the concentration and ohmic overpotentials are often significant sources of deviation from the theoretical value. The ohmic overpotential is related to Ohm's law and the resistance to the movement of ions through the different battery components including the electrodes and electrolyte; it only arises when current is flowing in the battery. The concentration overpotential is the result of concentration gradients which develop in liquid electrolytes in the battery. These losses add up to reduce the overall potential of a battery cell.

While these key equations govern how a battery functions, there are additional, higher-level, metrics which are used to define battery performance.

1.2.2 Battery Metrics

One of the most important battery metrics is lifetime. It may appear self-explanatory but it can be sub-divided further into cycle and calendar life. Cycle life is the number of charge-discharge cycles which a battery can undergo before its capacity decreases below an acceptable level. This level is usually defined as 80 % of the initial capacity. Calendar life, or shelf life, is the length of time that a battery can last in storage when not in use. Due to the highly reactive components in a battery, side-reactions can occur during storage, lowering the overall capacity.[6] Self-discharge is also a common problem during storage, the scale of which is highly dependent on battery chemistry and state of charge when stored.

Gravimetric and volumetric energy density measure the amount of energy a battery can store, one normalised by weight and the other by volume. While both are important, which one is a greater priority varies by application. For example, in electric vehicles space is at a premium, so volumetric energy density is very important. Meanwhile, for aerospace applications large batteries can be accommodated but heavy ones cannot.The specific term used to refer to them can vary, as either can be referred to as energy density and gravimetric can also be called specific energy density, therefore noting the units is key. Capacity is similar to these metrics, but has different units. Where gravimetric energy density is reported in Wh/kg, specific capacity is reported in Ah/kg, they differ by whether they incorporate the voltage of the cell.

Battery efficiency is also defined in two ways; overall and Coulombic. The overall efficiency includes losses due to factors such as internal heating. The Coulombic Efficiency (CE) is more narrowly defined as the ratio of charge input to the battery during charging to the charge output during discharge. CE is widely reported because of its effect on cycle life and capacity but can be misleading in Li-metal batteries as there is often excess Li at the negative electrode which can lead to a higher capacities than would normally be expected at a given CE.[7]

The importance of the temperature range over which a battery can function safely is dependent on the application. It is perhaps under-realised that electric vehicles will

need to withstand large temperature variations due to utilisation across the world in different climates and seasons. Additionally, batteries that will be used for aerospace applications will need to be able to withstand extreme cold without the electrolyte freezing, unless an additional warming device is used which would lower the overall efficiency. High temperatures can increase the likelihood of catastrophic failure. [8]

The most common reason rate is considered by the general public is due to speed of charging for electric vehicles. However, the discharge rate can be important for speed of response to grid demand or for other high-power applications. It is defined by C rate, shown in Equation 1.6, where 1 C means (dis)charging the cell fully in 1 h. Using a battery at high C-rates can reduce its cycle life by increasing the extent of degradation or triggering different mechanisms.[9] The maximum dis(charge) rate a battery can withstand can be converted to power density by multiplying the maximum current by the voltage of the battery and normalising by weight.

$$Crate(C) = \frac{(dis)chargecurrent}{batterycapacity} \tag{1.6}$$

General product metrics also apply to batteries. Cost is key, in particular cost of the battery as a proportion of the cost of the product it is powering (e.g. proportion of the cost of an electric vehicle). Safety is always important and has moved increasingly into the public consciousness as batteries have become more prevalent in society. Finally, batteries are being implemented to help combat climate change, therefore it would be counterproductive to cause new environmental problems with their development. The environmental friendliness of battery materials from cradle to grave should be taken into account through life cycle analyses.

It is worth noting that these metrics may not be reported or are selectively reported in the literature, or, as has been stated earlier, may be referenced with a different name, which makes it difficult to compare (see Figure 1.2). There have been numerous calls for standardisation from within academia [10], but as of yet there is still not a standard for reporting.

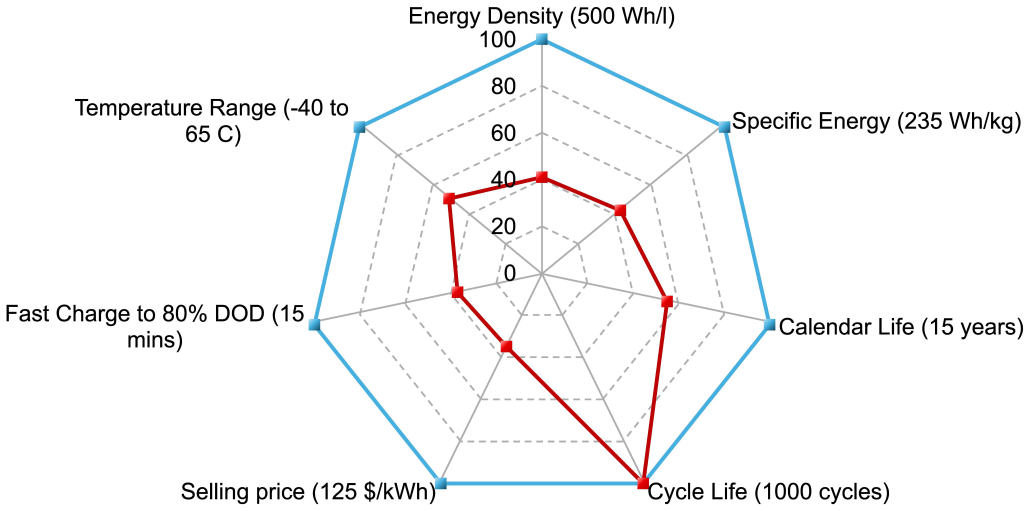


Figure 1.2: Example radar plot showing the difference between the state-of-the-art for Li-ion batteries in 2016 (red) and the United States Advanced Battery Consortium (USABC) goals for batteries (blue). This demonstrates the importance of these metrics and gives an idea of the strengths and weaknesses of this type of battery. Reproduced from [11].

1.2.3 Battery Materials

The first rechargeable lithium batteries were commercialised in the 1980s by Moli Energy used a Li_xMoO_2 positive electrode and Li-metal negative electrode, but had to be taken off the market shortly after because of flammability issues relating to the instability of Li metal. [12] The combined discoveries of Nobel laureates Whittingham, Goodenough, and Yoshino enabled the commercialisation and wide adoption of Li-ion batteries with a graphite negative electrode and $LiCoO_2$ (LCO) positive electrode, which is still widely used today. [13–15]

Electrolytes are usually an organic solvent with a lithium salt. Commercial compositions may contain a variety of components but common solvents include carbonates and ethers, and salts include $LiPF_6$ and $LiClO_4$. [16] Liquid electrolyte compositions have a huge effect on performance as they alter the transport of the Li^+ ions across the battery, and form reaction layers on the negative and positive electrodes (SEI and Cathode electrolyte interphase (CEI), respectively). Electrolytes should have high ionic conductivity, high transference numbers, and

good stability against the electrodes to enable fast charge and discharge without significant concentration gradients forming (which lead to overpotentials), and prevent continuous side reactions which reduce capacity. Ideally, they should also be non-flammable to improve safety, as the electrolyte decomposing or catching fire during thermal runaway is one of the major safety risks of batteries, but this is difficult to achieve while maintaining performance and is an ongoing area of research.[17]

Among Li-ion batteries, the majority of electrode differentiation occurs at the positive electrode, while graphite is usually the negative electrode. Some examples are discussed below and illustrated in Figure 1.3. The layered oxide LCO remains a common material used in many electronic devices, however the high cost of Co and the ethical issues surrounding its production have pushed researchers to develop alternatives with lower Co contents.[18] These same issues have increased interest in the olivine $LiFePO_4$ (LFP) as it contains more plentiful (cheaper and easier to access) materials. It also has good cycle life, safety, and power capabilities, but its lower gravimetric energy density has limited its wider application.[19] $LiMn_2O_4$ (LMO) is an alternative Co-free material with a spinel structure. This allows for 3D Li^+ transport, rather than the 1D transport as in LFP. However, Jahn-Teller distortions reduce its cycle life.[20] $LiNi_{0.5}M_{1.5}O_4$ (LNMO) has similar safety benefits to LMO but with higher rate capabilities and energy density because of the stabilising influence of Ni. However, this Ni content also increases the cost slightly compared to LMO.

$LiNiO_2$ is too unstable to be used as a cathode material, but in combination with other materials, in particular Co, has produced some of the highest energy-density cathodes. $LiNi_xMn_yCo_zO_2$ (NMC) is known to be one of the highest-performing positive electrode materials, due to its high voltage which leads to a high energy density. Variations of this material change the ratios of the transition metals, often with the goal of reducing the amount of Co. NMC811, where the 811 refers to 80% Ni, 10% Mn, and 10%Co on the transition metal site is particularly promising. However, reducing the Co also tends to reduce the stability, leading to work on

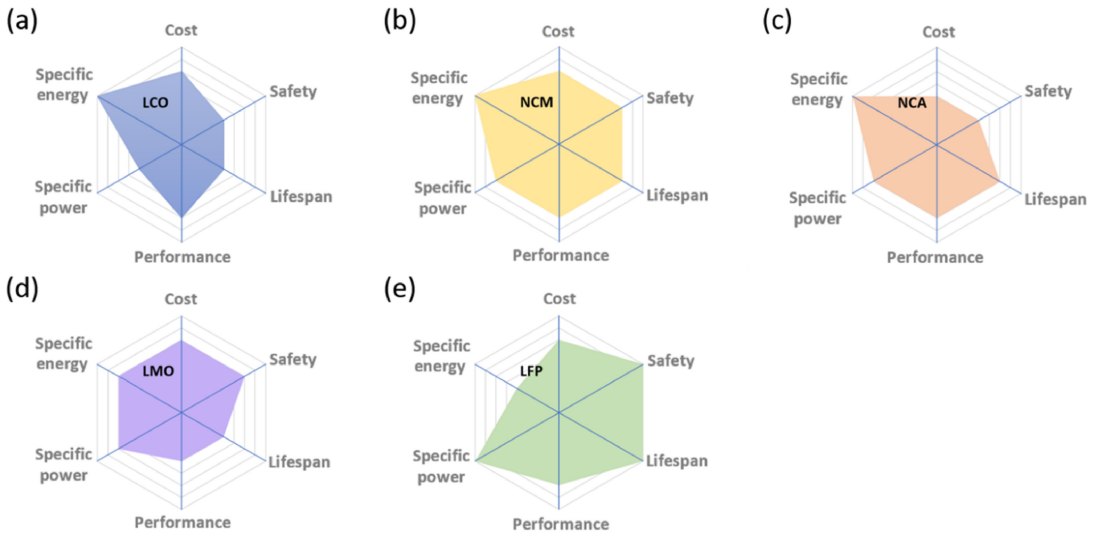


Figure 1.3: Radar plots comparing some common positive electrode materials including (a) LCO, (b) $LiNi_xMn_yCo_zO_2$ (NMC), (c) $LiNi_xCo_yAl_zO_2$ (NCA), (d) LMO, and (e) LFP. Reproduced with permission from [21].

surface coatings and microstructure design to help maintain the structure during cycling and reduce side reactions. [22, 23] $LiNi_xCo_yAl_zO_2$ (NCA) is also being developed heavily as it also has a high voltage and often has a higher capacity than NMC. However, it (generally) contains a higher amount of Co, which makes it more expensive, and it has lower thermal stability. [24] While NCA and NMC can increase the energy density of Li-ion batteries above 200 Wh kg^{-1} at a cell level, cells with a liquid electrolyte and graphite negative electrode are reaching the practical limits of what can be achieved.[25–29]

1.3 Lithium Metal Anodes

Li metal has a specific capacity of 3862 mAh g^{-1}, which is an order of magnitude higher than that of graphite (372 mAh g^{-1}), making it the "holy grail" of negative electrodes and enabling substantially higher energy densities and new battery chemistries.[29] Unfortunately, its reactivity, heterogeneous plating, and the resulting safety issues have meant that it has not been successfully commercialised in rechargable batteries. The intrinsic properties of Li metal are key to understanding its performance in batteries.

Lithium has a Body-centred cubic (BCC) structure and is extremely ductile at room temperature with a yield point of 0.75 MPa and a low melting temperature of 180.5 °C. Masias et al. investigated the mechanical properties and creep of Li metal, determining that it has a Young's modulus, shear modulus, and Poisson's ratio of 7.82 GPa, 2.83 GPa, and 0.381 GPa, respectively. They also showed that it follows a power creep law via a dislocation climb mechanism.[30] Investigations into the nucleation and growth of Li during plating have shown that the weak Li-Li bond strength, which was calculated to be on average 0.18 eV weaker than Mg-Mg, leads to a lower free energy barrier to low dimensional morphology formation, such as that found in dendrites.[31] Lithium has a self-diffusion coefficient of approximately 7.65 cm^2 s^{-1} at room temperature, high reactivity, and infinite volume change when used in a zero-excess electrode.[32] These factors complicate the use of Li as a negative electrode.

1.3.1 Dendrite Nucleation and Growth

Dendrite nucleation and growth has drawn a lot of attention in Li metal batteries as dendritic growth is the main mechanism by which short-circuits occur, leading to thermal runaway, fire, or even explosions. This is why Moli Energy Li-metal batteries failed. In addition to the safety issues, thin dendrites are susceptible to breaking leading to "dead" disconnected Li and the high surface area means there is a larger area for reactions with the electrolyte to occur. Both of these processes can lead to significant capacity loss and increasing resistance due to continuous side reactions, and can lead to cell failure. There have been substantial efforts to better understand the nucleation and growth of Li metal dendrites, with models incorporating Butler-Volmer kinetics (Equation 1.5), diffusion limits, elastic stress, and plastic flow of Li. [33–36] The plastic flow, or creep, of Li is directly related to its low melting point, which makes it more susceptible to this phenomenon at room temperatures than most metals. The different phases of nucleation and growth include the time it takes for the initial deposition overpotential to be overcome, then for the diffusion limitations to become significant (Sand's time), and finally

for plastic flow to develop under pressure.[37–39] The specific times taken for these factors to become significant depend on the properties of the electrolyte, SEI, and external factors such as applied pressure.

Often, dendritic growth is spoken of in relation to a Critical Current Density (CCD), beyond which dendrites form and the battery fails. As can be seen in Figure 1.4 taken from Jana et al., it can be a bit more complicated than defining a single value, although there is certainly a strong dependence on current density.[40] At low current densities, the minimum size of the dendrite (shown by the black line in the figure) is higher, leading to larger deposition sizes whose growth is then dominated by base plasticity. Smaller depositions will not form dendrites, so this is line represents the CCD. Beyond this point, the balance of growth processes determines the morphology of the Li deposition. At higher current densities, both base and tip growth is observed as base plasticity balances higher rates of electrodeposition at the dendrite tip due to a concentration of electric field lines. As current density continues to increase, or with smaller electrodeposits, the build up of stresses in the deposits makes plastic deformation at the tip can significantly affect the dendrite microstructure. Qualitative matches to experimental literature are shown for this region in the second part of the figure, starting from incubation growth (◯), to base-growth dominated columnar growth (▷), to onset of dendritic growth due to tip electrodeposition (♢), and a more complex bushy microstructure developing as tip stresses rise and tip plasticity plays a roll (□).[38, 41–43] To the right of the orange line is the Sand's regime where mass transport becomes limited and highly dendritic structures are observed. [40, 41]

As shown, the low melting temperature of Li means creep/plastic flow can be significant at room temperature, so pressure and can have a meaningful impact on dendrite microstructure. Altering the pressure on deposited Li can be done by changing the SEI or by applying pressure externally. Stronger SEIs will put more pressure on the Li dendrite tips, encouraging more homogeneous growth, which is why mechanically strong SEIs are desired.[44] External pressure has been shown to aid performance in both solid and liquid electrolyte batteries as it improves interfacial

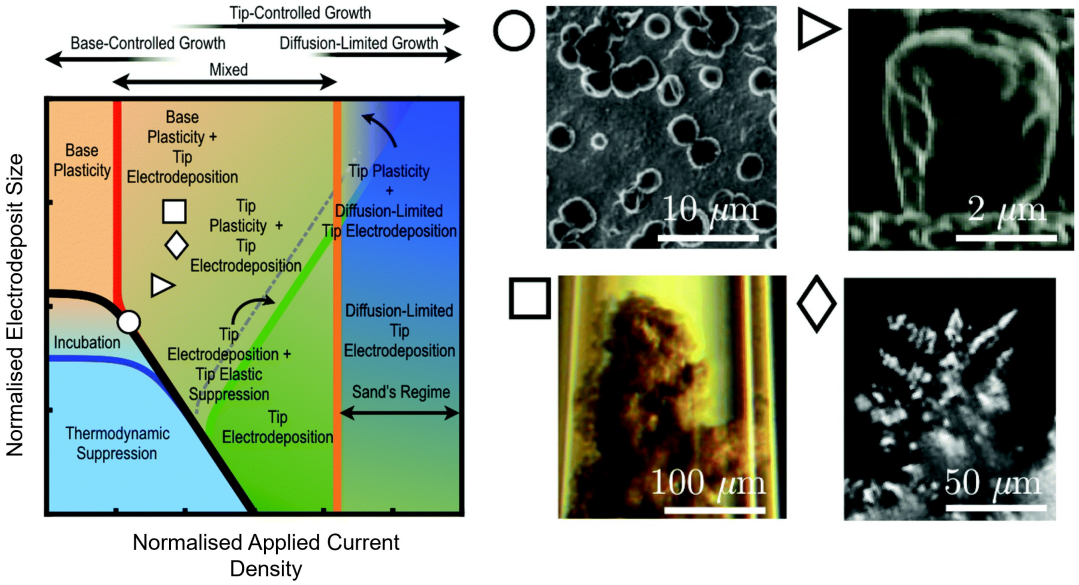


Figure 1.4: Diagram corresponding to the different growth regimes of lithium dendrites as a function of electrodeposit size and applied current density. The black line shows the kinetic limit below which stable deposition occurs, the orange line shows the barrier to Sand's regime, beyond which mass transport limitations dominate. In between these lines there is a mixed growth region where elastic stresses and the plasticity of Li can lead to differences in growth morphologies as shown in the right of the figure. The shapes on the diagram qualitatively match to where the images would fall. ◯ shows nuclei deposited on Cu at 0.1 mA cm^{-2} for 1 h. ▷ shows columnar growth of Li on Cu under a hollow C layer after 50 charge/discharge cycles. □ shows a mossy Li deposition on Cu at 2.61 mA cm^{-2} for 0.5 h. ♢ shows Li deposition in a gel-based electrolyte (only non-liquid) at 3 mA cm^{-2} for 1 h. Reproduced with permission from [40] and showing images from [38, 41–43]

contact, reduces the presence of voids, and suppresses dendrite growth.[45–48] But too much pressure has been linked with Li ingress in ASSBs, increasing the chance of short-circuits. [49] A happy medium must be struck between the two, which seems to be around 150 kPa for liquid electrolytes and 5 MPa for solid electrolytes.[48, 49]

The above description of dendrite growth is theoretical, therefore the calculations must refer back to experimental evidence to validate their results. Microscopy is used for this, as shown above, but at this scale (μms) optical microscopy can be beneficial as it is easier to obtain *operando* results. By pairing optical microscopy with electrochemical characterisation, invaluable links can be made between electrochemical traces and physical meaning.[50] It is more difficult to obtain *operando* or in-situ results when using electron microscopy as by definition

this must occur in a vacuum. To understand the morphology of the nucleation and growth of dendritic structures, optical microscopy is often sufficient as they are on the order of μm. To understand smaller structures which influence dendrite growth, notably the SEI, higher resolutions are needed.

1.3.2 Solid Electrolyte Interphase

As mentioned above, the solid electrolyte interphase (SEI) affects Li deposition morphology and directly affects the performance of the battery. A good SEI should be thin, passivating (electronically insulating), mechanically stable enough to prevent dendrite penetration, ionically conductive, and homogeneous.[44] A thin, passivating SEI will prevent continuous reactions which decrease capacity and increase resistance of the cell.[51] If the SEI is electronically insulating, this should suppress chemical reactions, unless it is cracked or damaged. To prevent this from happening the SEI needs to be able to withstand high volume changes during cycling and suppress dendritic growth.[52, 53] Finally, as a layer on the surface of an electrode, the Li^+ ions need to pass through it to reach the electrode, if it has a high resistance it can reduce the performance of the battery, and a heterogeneous composition with differing ionic conductivities leads to "hot spots" of Li deposition, current concentration, and dendritic growth.[29, 54]

The exact structure and chemistry of the SEI varies depending on the battery chemistry and electrolyte and it is very difficult to image them so most of the theories are based on extrapolation from theory and electrochemical analysis. A few proposed structures are shown in Figure 1.5. The first theories were developed by Peled who suggested a theory that it has a "mosaic" structure with domains of different compounds formed from reactions between the Li and electrolyte.[55] Within this structure, it has been suggested that there is a compact inorganic layer closer to the electrode and a more open, organic layer further away from the interface (Figure 1.5 (A)).[55] Cryo-Transmission Electron Microscopy (TEM) has confirmed and expanded on the structures proposed by Peled, with Li et al. showing that carbonate electrolytes form the classic "mosaic" morphology while

fluorinated electrolytes exhibited a more ordered structure, with only small changes in chemistry identified by Energy Dispersive X-ray Spectroscopy (EDX) (Figure 1.5 (B)).[48, 56] Liu et al. investigated the role of nitrates in carbonate and ether electrolytes, demonstrating that their benefits are due to promoting spherical deposition morphology via a modified bilayer SEI morphology, where cryo-TEM enabled a greater understanding of the amorphous SEI structure containing localised crystalline domains (Figure 1.5 (C,D)).[57–60] Most of the cryo-microscopy studies use a "washing" step in their sample preparation, which is a requirement so as not to freeze so much electrolyte that the sample is no longer electron transparent, but can also remove key parts of the sample. Zachman et al. avoided this problem by developing a full cryo-workflow to thin the electrolyte with a FIB.[61] They were able to reveal an extended SEI, thicker than shown by others, and very porous (Figure 1.5 (E)). An extended SEI could trap a large amount of SEI without increasing the resistance of the battery greatly as the liquid electrolyte can still reach the electrode, decreasing the capacity while allowing the battery to continue functioning if there is sufficient excess Li. As excess Li is often used in Li-metal battery testing, this may be flying under-the-radar in lab-scale tests. In addition to cryo-microscopy, techniques such as X-Ray photoelectron spectroscopy (XPS), EDX, and Atomic Force Microscopy (AFM), are used to gain more insight into the specific compounds present in a given SEI layer.[62, 63] Some of the most common components with liquid electrolytes include a variety of insoluble reaction products such as LiO_2, Li_2CO_3, and LiF.[64]

The mechanical requirements of the SEI are non-trivial. It needs to be flexible enough to deal with volume changes, but stiff enough to suppress dendrite growth. It is generally considered that the inorganic, crystalline components of the SEI provide stiffness and strength, while the organic components provide flexibility. It is therefore beneficial to have a combination of both, and too high of a modulus can be counter-productive if it leads to lower flexibility.[52] There have been various attempts to characterise the mechanics of the SEI, with AFM providing a majority of the studies.[65–67] But as with all physical characterisations of the SEI there

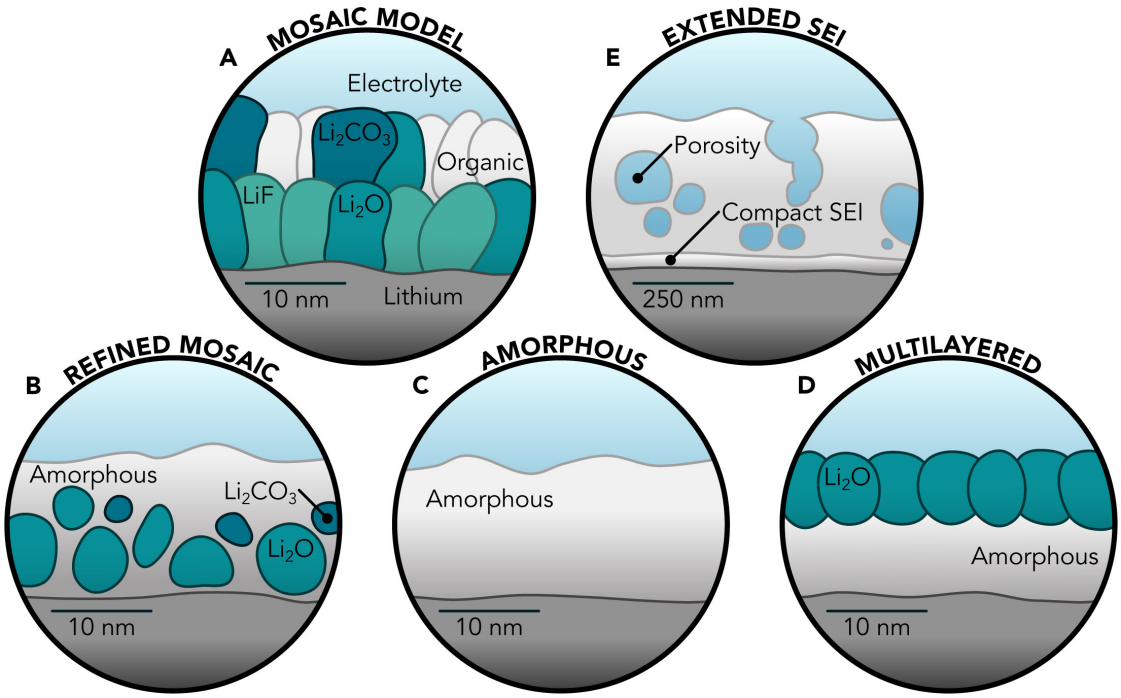


Figure 1.5: This figure shows schematics of various proposed SEI structures from the literature. (A) This displays the traditional mosaic SEI model proposed by Peled with a predominantly inorganic layer closer to Li and a predominantly organic layer further away.[55] (B) Later research refined this model to give the more heterogeneous mosaic shown here. [48, 56] Beyond the mosaic structures, others have been observed, including (C) purely amorphous, [58, 59] (D) layered structures with amorphous SEI observed close to the Li and a majority Li_2O SEI further away, [56, 60] and (E) extended SEIs which are orders of magnitude larger and highly porous.[61] Often the extended SEI is removed during sample preparation steps and is not observed in ex-situ measurements. These extended SEIs are highly non-passivating and can cause large capacity losses. Reproduced with permission from [44].

are significant sample preparation difficulties which lead to differences in reported results, for example the effect of substrate on characterising thin films and the inclusion (or not) of the liquid electrolyte during AFM.[68, 69] There is even a large range in the theoretical calculations of what the mechanical strength of the SEI could be.[70] This is because of the lack of experimental results on which to base these results, highlighting the importance of further development of experimental techniques to shed light on the structure and chemistry of the SEI.

Assuming the SEI remains physically stable, transport through it can still cause current concentration if it has a heterogeneous structure. This may even lead to dendritic growth below what the CCD would be otherwise. With liquid electrolytes,

transport is a combination of through the solid SEI, along cracks and grain boundaries, and through the liquid electrolyte within pores.[71, 72] Without a strong consensus in the literature for the SEI structure in ASSBs, it can only be assumed that the transport streams are similar, but with "pores" in the SEI filled with SSE as much as is possible in a rigid system. The specific mechanism behind ion transport through the SEI is component-specific, but knock-off and vacancy mechanisms have been suggested for some common components.[73] Most studies on transport through the SEI are computational, based on models investigated with Molecular Dynamics (MD) or Density Functional Theory (DFT), and evaluated by results of electrochemical analysis from techniques such as Electrochemical Impedance Spectroscopy (EIS).[74–77] Investigating transport mechanisms experimentally has been attempted with techniques such as Nuclear Magnetic Resonance (NMR), but significant difficulties with sample preparation have limited the literature in this area.[78] Of course, the models used are based on characterisation of the SEI structure done using the few techniques which are capable of imaging such a thin, sensitive layer. Cryo-Electron microscopy (EM) has been particularly useful in elucidating these structures since its first application to batteries by the Cui group, but further work is still required in particular for solid-state systems.[56]

1.3.3 Performance Improvements

A common way to evaluate the performance of a Li metal anode is to look at the CE. To produce a Li metal battery which can run for 200 cycles with a capacity retention above 80 %, the CE would need to be above 99.9 %.[79] This value has yet to be reached, is still far below the goal for many use cases, and is significantly lower than the 1000s of cycles Li-ion batteries can achieve. [80] To achieve 1000 cycles CE of 99.98 % would be required. While there have been significant improvements over the last few decades, in particular with the liquid electrolyte batteries shown in Figure 1.6, there is a plateau around 99 %, demonstrating the difficulty in exceeding this limit with the current technology.

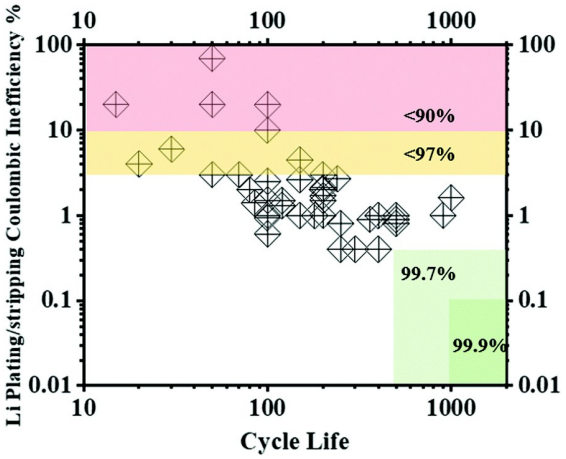


Figure 1.6: Summary of Li metal battery Coulombic efficiencies reported in literature as of 2020. All reported cells use liquid electrolytes. It is clear that there are none close to the required efficiencies for practical use and there have not been significant improvements on this in liquid electrolytes since. Reproduced with permission from [79].

Host structures are used with Li-metal to control the deposition morphology and volume change. This can be done by modifying the Current collector (CC) to form a 3D host structure, reducing the local current density, and encouraging a high number of deposition sites with desired morphologies.[81] Changing the CC material can also improve the deposition behaviour as it has been shown that having a higher nucleation energy barrier leads to larger, less homogeneous initial electrodeposits, which increases the chance of dendritic growth.[82] On the other hand, some Li alloys have been shown to lower this energy and have high surface diffusivities to encourage smooth deposition morphologies.[83, 84] The application of alloys as host materials has seen particular interest in ASSBs as loss of contact due to volume changes is of particular concern, as will be discussed in more detail in the next section.[85] When any component is added to the battery, the reduction in energy density and increase in cost must be balanced against its benefit to CE.[86]

As has been discussed above, changing the electrolyte affects the Li^+ transport and the formation of the SEI. As LiF content in the SEI has been correlated with better performance, highly fluorinated electrolytes are common, although the exact reason for this benefit remains unclear.[87] Another promising recent advance in the field of liquid electrolytes has been Highly concentrated electrolytes (HCEs),

where the high salt content is thought to encourage a stable, passivating, highly inorganic SEI to form.[88] The high cost and viscosity due to the salt concentration in HCEs drove the development of Locally highly concentrated electrolytes (LHCEs) which have the benefits of HCEs as a diluent aids in maintaining similar solvation structures with lower salt concentrations.[89, 90] Even with these developments, the required performance has not been achieved, leading to the most drastic change in the electrolyte, becoming solid, which will be discussed in the next section.

Finally, artificial SEI layers have been applied to protect the Li surface. The same mechanical and Li^+ transport factors considered for "natural" SEI are desirable for "artificial" SEI. For this reason, combinations of inorganic compounds which have high ionic transport and organic compounds which have higher flexibility have been utilised.[91] Some common methods involve using compounds such as LiF, which is associated with high performance in the SEI, sputtering thin oxide films known to have high moduli (e.g. Al_2O_3) onto the surface, or long-chain alcohols and carboxylic acids to provide flexibility.[92–94] As with a modified current collector, the reduction in energy density should be taken into account, but as they are usually on the order of a few nm, the effect is often negligible.[86]

Effectively what an "artificial" SEI is trying to do is act as an ultra-thin solid-state separator between the deposited Li and the liquid electrolyte. The logical next step is to work from a thicker SEI which could then act as the electrolyte itself, leading to the concept of an all-solid-state battery.

Interest in All-solid-state-batteries (ASSBs) was sparked by their potential to improve safety and prevent dendrite growth, even at high current densities.[95, 96] As stated above, they seem like a logical extension of some of the tactics used with liquid electrolytes. Development of Li-metal and ASSBs are intertwined as to achieve energy and power densities comparable or greater than Li-ion batteries in solid state, Li metal must be used, which means high volume change, dendritic growth, and interfacial reactions must be navigated.[97] In theory, as SSEs generally have a transference number close to 1 (although polymers can have lower values) Li concentration gradients should not form, preventing dendritic growth. In addition,

the high moduli of SSEs should mechanically prevent Li dendrites from growing through them.[33] Finally, the higher thermal stability of SSEs should make them safer, in addition to the reduced probability of short-circuits.[98] The advantages of ASSBs should enable much higher current densities, meaning lower charging times. But only if their ionic conductivity is sufficient.

Unfortunately, few of these promises have been fulfilled. Volume change during cycling has proven to be a major issue as it leads to SSE and electrode cracking and loss of contact. Contact issues, including void formation at the Li interface, have severely hindered rate capabilities.[99] Dendrite growth has also been observed in a wide variety of SSEs even with moduli significantly higher than that of Li, which according to Monroe and Newman should be able to suppress dendritic growth.[100–102] These issues demonstrate the complicated mechanical property requirements for SSEs. These are summarised by their shear modulus, Young's modulus, fracture toughness, and interfacial adhesion.[103] A balance must be struck between these properties so that they are sufficiently strong to withstand dendritic growth but not so brittle as to crack easily under the stresses of volume change.[104] Good surface adhesion lowers interfacial resistance, reduces the chance of current concentration and dendritic growth, and can be predicted by the wetability of a material by Li metal.[105]

The interfacial reactions between Li and several SSE have proven to form significant SEI layers, increasing resistance at the interface.[106] However, the effects this has on performance are not fully understood because the challenges of characterisation mean that information on the SEI in ASSBs is still extremely limited. It is expected that, as with liquid electrolytes, this can affect Li^+ transport at the interface. Depending on the structure and composition of the SEI it could increase current concentrations, encouraging dendrite growth, decrease adhesion at the interface, and weaken the structure so that it is easier for dendrites to propagate.[103] Alternatively, a homogenous and strong SEI could be helpful in promoting uniform plating and preventing dendritic growth, as with liquids.[44]

Further research is required to better understand the mechanics of SEI growth and its effect on the rest of the battery.

Processing is also a challenge, as a SSE must be homogeneous and dense to reduce current concentration and dendrite formation, and thin to reduce resistance, cost, and mass. However, they can be brittle and air-sensitive, which makes them difficult to handle.[107] Additionally, many of the most effective processing techniques are non-scalable or expensive.[108] Finally, as thermal stability has been investigated further, many SSEs display worse performance than was expected.[109] As most of these problems are associated with interfaces, so these have been the focus of research. Some of these problems associated with ASSBs' interfaces are summarised in Figure 1.7.

1.4 Solid-state Batteries

The ideal SSE needs to have an ionic conductivity on the order of liquid electrolytes in order to compete in terms of rate performance (10^{-3} Scm^{-1}). It should also have sufficient mechanical properties to withstand the stress induced by volume changes at both electrodes during charge-discharge cycles without fracturing or losing contact, be able to easily form a dense and homogeneous structure, have a wide electrochemical stability window (or at least form a passivating and homogeneous SEI), and be low cost and environmentally benign.

1.4.1 Solid-State Electrolyte Materials

Broadly, Solid-state electrolytes (SSEs) can be divided into organic and inorganic. Note that semi-solid or solid-liquid hybrid electrolytes have also been used, but that is beyond the scope of this work. The first and most common organic SSEs are polymers based on a Polyethylene oxide (PEO) backbone. Their main advantage over inorganics is their ability to maintain contact due to their flexibility and compared to other organics it has good interfacial stability against Li and electrochemical stability, as well as acceptable Li transport properties with conductivities on the order of 10^{-3} S cm^{-2} above 63° C.[110] At room temperature, their ionic conductivity

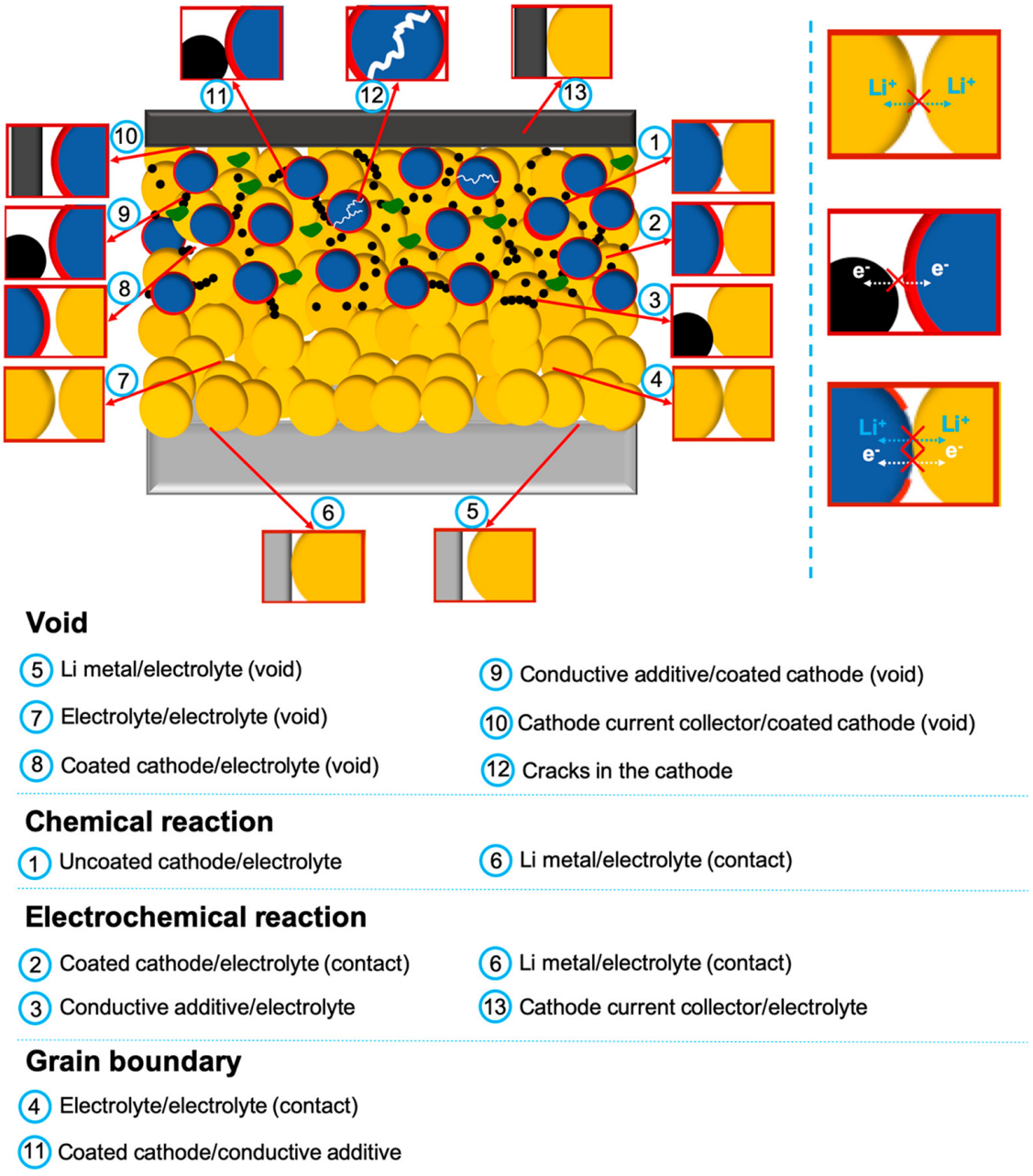


Figure 1.7: Schematic illustration of interfacial degradation processes observed in ASSBs. Reproduced with permission from [99].

is too low for use (10^{-7} to 10^{-8} S cm^{-2}). Introducing higher salt contents, similar to what has been done with liquid electrolytes, increases the ionic conductivity by forming polymer-in-salt electrolytes. However, this decreases the mechanical stability and flexibility of the electrolyte, which is their main advantage. Changing the polymer structure (e.g. by block co-polymerisation, grafting, and cross-linking) has shown some promise but the ionic conductivities have yet to reach a level

where they are competitive with inorganics.[111]

Overall, inorganic SSEs consist of three major groups; oxides, halides, and sulphides. They exhibit high shear moduli, suggesting that they should be able to suppress dendrite ingress, but they are also more difficult to manufacture into thin, dense films. Oxide electrolytes, including the garnet $Li_7La_3Zr_2O_{12}$ (LLZO), have attracted attention for use because of their stability in air and against Li while possessing ionic conductivities on the order of 10^{-3} - 10^{-4} S cm^{-2} at room temperature.[112] The addition of interstitial dopants such as Nb can further improve their interfacial stability and ionic conductivity.[113] However, their high mechanical strength also makes them very stiff, leading to contact loss and their high melting points require high (expensive and energy intensive) sintering temperatures to produce dense samples. As can be seen in Figure 1.8, halides have comparable ionic conductivities to oxides. Their main advantages are their stability, including to humid air, but they have still been shown to react with Li.[99, 114] An honourable mention should go to the amorphous oxynitride Lithium phosphorous oxynitride (LiPON), which has been applied successfully in thin-film micro-batteries, but its low ionic conductivity (10^{-6} S cm^{-2}) limits its application to this niche.[115]

To perform comparably to Li-ion batteries, ASSBs require ionic conductivities similar to those of liquid electrolytes (10^{-2} - 10^{-3} S cm^{-2}). Arguably, they require even higher conductivities due to the effect of tortuosity in composite cathodes and if non-conductive binders are necessary to reach the required flexibility for manufacture of Thin Solid Electrolyte (TSE)s of commercially relevant thicknesses, which is the case for brittle ceramics.[116, 117] The only class of SSEs which has achieved this metric is the sulphides, as can be seen in Figure 1.8. They generally exhibit lower moduli and melting temperatures than oxides, which should make it easier to manufacture SSEs with suitable microstructures under practical processing conditions.[118, 119] As with all ceramics, they also possess high shear and Young's moduli, and while these are lower than for oxides they are still well above those for Li metal.[103] They exhibit some significant drawbacks, notably sulphides react with moisture in the air to produce H_2S and have a narrow Electrochemical Stability

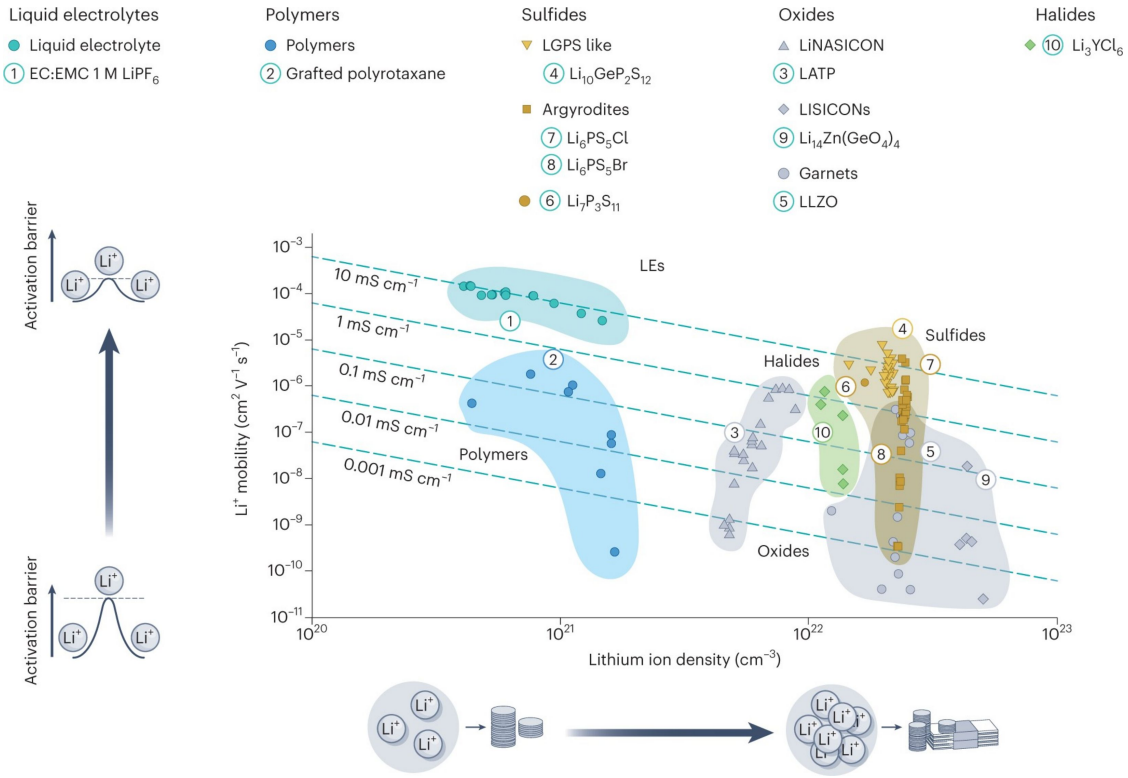


Figure 1.8: Graph comparing the ionic mobility and charge density of different SSE groups. The ionic conductivity is shown as dashed isoconductivity lines. Li density is considered as a proxy for price. Reproduced with permission from [97].

Window (ESW) so are degraded by both Li-metal and most positive electrodes.[120] However, their advantages make them a highly promising class of SSEs.

The first sulphides to be investigated were glasses, which showed promise due to their high ionic conductivities, isometric properties, and greater ease of manufacturing compared with oxides.[121] While some metastable crystalline phases within the glasses demonstrated very high ionic conductivities in the required range ($Li_7P_3S_{11}$ (LPS)), the real promise came with the application of the $Li_{10}GeP_2S_{12}$ (LGPS) and argyrodite structures.[122, 123] While both of these structures have demonstrated SSEs with ionic conductivities on the order of liquid electrolytes, their interfacial stabilities are very different. The electronically conductive SEI containing Ge and Li_3P which continuously forms between LGPS and Li makes it impractical for use. Argyrodites will also form a SEI but as it does not contain metallic components, it has been suggested the SEI propagates at least an order of magnitude slower than

in LGPS.[106, 124, 125] Therefore, among the promising sulphides, argyrodites are particularly interesting and will be utilised as the SSE throughout this thesis.

Sulphide Argyrodites

Sulphide argyrodites have the formula Li_6PS_5X (X=halide) and the space group $F\bar{4}3m$. Their greatest strength is their ionic conductivity, and X = Cl,Br chemistries exhibit significantly higher conductivities than X = I.[126] This has been developed further by halide and aliovalent doping to reduce the diffusion barrier and increase the concentration of Li vacancies.[127, 128] Increasing the entropy of the SSE has been shown to stabilise the structure against higher defect concentrations which in turn enables higher ionic conductivities.[129] However, doping to increase the ionic conductivity can further reduce stability.[130] While, thermodynamically, argyrodites will break down into Li_3P, Li_2S and LiX, the impact of kinetics and structure on how the SEI develops is not known.[131] The SEI increases the resistance of the interface, reducing the benefits of high ionic conductivity.[106] Therefore, a better understanding of it is fundamental to the broader utilisation of these materials.

1.4.2 Areas for Future Work

Scalable methods of processing SSEs to form dense, homogenous films with sufficient mechanical properties to prevent cracking during battery assembly and cycling are urgently required. Lab-scale experiments often use thick (> 500 μm) SSEs, while practical thicknesses are considered to be < 150 μm to reach a level comparable to Li-ion batteries.[107] These are prepared via high-cost vacuum-based techniques or high-temperature sintering which can alter the lead to decomposition or side reactions if co-sintering occurs with the positive electrode.[132] As ceramics are brittle, for scalable processing it is useful to make composites with a more ductile polymer to enable more scalable manufacturing methods to be used.[117, 133] This is still a developing area of research and may require even higher ionic conductivity

ceramics to compensate for the tortuosity introduced in the composite, or two-step manufacturing processes where the ductile polymer is later burned out to form a dense, homogeneous film.

Interfacial issues are some of the most difficult problems facing ASSBs. Specifically, these include Li dendritic growth, SSE fracture, void formation and SEI formation. These have all proven to be highly significant problems in sulphide electrolytes, despite the initial hypotheses that aspects such as SEI and dendritic growth may be limited by the solid nature of the SSEs.[100, 106, 134, 135] While all of these areas have received some degree of study, there is still much uncertainty about the underlying mechanisms. Much of this uncertainty is due to the difficulty of characterising buried, reactive interfaces. Without further development and application of characterisation techniques, understanding of these interfaces will not reach a level where they are able to be commercialised.

1.5 Characterisation of the Li-SSE Interface

As has been shown, the interfaces in all-solid state batteries are key to performance and degradation. Understanding what occurs there is of paramount importance, but accessing, imaging, and analysing these interfaces is difficult.

1.5.1 Limitations of Electrochemical Characterisation

The most common methods for battery characterisation are electrochemical techniques such as EIS, Cyclic Voltammetry (CV), and potentiometry. These can give a wealth of information on changes in the potential and impedance at electrodes and interfaces. However, to translate these data into physical meaning, they need to be matched with models derived from physical characterisation. That being said, there have been some interesting developments in the electrochemical characterisation of ASSBs. The SSE makes development and placement of a reference electrode difficult, but the Janek group has produced work to quantify this effect and encourage more reliable placement.[136] They additionally developed a novel technique to investigate the growth of the SEI called Coulometric Titration Time Analysis (CTTA) which

involves depositing a small amount of Li and analysing how long it takes for the potential to rise, suggesting full conversion to SEI.[135] This is an interesting approach, but again without physical characterisation, the conclusions drawn in terms of structure and thickness of the SEI include significant assumptions.

1.5.2 Sample Preparation Challenges

Physical characterisation of any battery material is inherently challenging because they are reactive and air sensitive, almost without exception. Li metal, with its extremely low potential, is one of the most extreme examples of this. It has been shown to react with trace oxygen even within an Ultra high vacuum (UHV).[137] Sulphide SSEs also degrade in air, changing their chemical make-up and producing toxic H_2S.[138] Therefore, to accurately characterise these materials, extreme care must be taken to avoid air exposure. This has delayed characterisation efforts as these workflows often require laboratories to obtain expensive equipment or even to develop their own.[61]

While Li morphology in liquid electrolytes can be investigated via optical microscopy without any severe artifact introduction, SSEs are not usually optically transparent which complicates in-situ or *operando* analysis by these methods. X-Ray techniques are easier to use because they are more penetrating, but can still require complicated cell designs to maintain pressure and inert conditions. For ex-situ analysis, the removal of a SSE from a cell can radically change the Li morphology due to its low modulus and high adhesion, limiting the utility of this data.[102, 139] Fracture of the cell before imaging of the cross-section has also been utilised. This works well for brittle ceramic SSEs and metal oxide positive electrode materials, but again the morphology of ductile Li can be severely affected.[140] This has prompted the use of ion milling as a sectioning method. This was initially limited because of the artifacts introduced by milling of Li at room temperature due to melting and Ga implantation/alloying, but cryo-Focused-Ion Beam (FIB) has been shown to alleviate these issues.[141]

Finally, in particular for characterisation techniques where small samples are required, brittle ceramic SSEs and ductile Li are difficult to handle without introducing cracks or morphological artifacts. The release of pressure when removing ASSBs from the assemblies they are tested in, which on a lab scale are usually cycled under pressures from 1 - 50 MPa, can lead to shifting of components. Removing current collectors to access the electrode and SSE underneath can distort the Li morphology, and removing SSE from densification and testing assemblies can cause crack formation. These artifacts can disguise interfacial degradation mechanisms or lead to false conclusions.

1.5.3 Morphological Characterisation

Early studies into Li nucleation and growth in ASSBs utilised optical microscopy. By imaging through transparent and air-stable LLZO, a Li propagation model was developed suggesting that Li plates into existing cracks which grow due to "crack-tip stresses" [142] A similar methodology was used to link dendrite growth in SSEs with electrochemical signatures.[143] Optical microscopy, especially through SSEs, has severe limitations on the resolution and depth which can be achieved. X-Ray techniques have provided more detailed characterisation of Li plating, void formation, and dendrite growth deeper into the electrolyte. However, it remains challenging to design cells which are air-tight and can apply sufficient pressure whilst being X-Ray transparent and representative.[144–146] *Operando* synchrotron X-Ray Tomography (XRT) is particularly useful because it can provide high temporal resolution of morphological changes. Wu et al. used it to describe the evolution in tortuosity of conduction paths through SSEs due to volume changes during cycling.[147] The Bruce group also used it to demonstrate a two-step mechanism separating the initiation and propagation of cracks in Li_6PS_5Cl via pore-filling then wedge-opening mechanisms, respectively.[100] A figure demonstrating this mechanism can be seen in Figure 1.9.

While X-Ray techniques are very powerful tools for analysing the microstructure of ASSBs over relatively large fields of view, their resolution is more limited

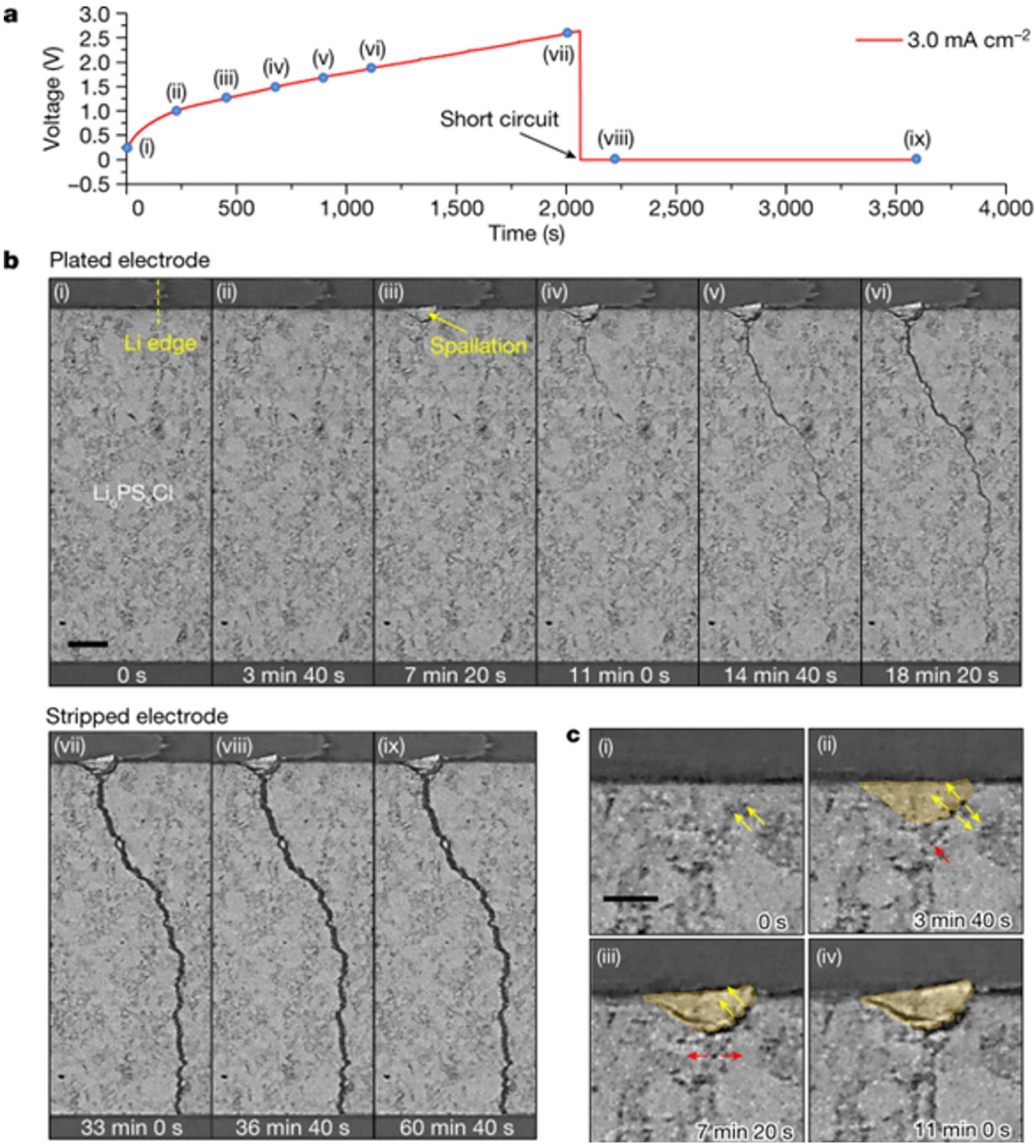


Figure 1.9: (a) Voltage vs time graph for the cell with end points of the XCT slices shown in (b) marked (i) - (ix).The cell was symmetric Li-Li cell with a Li_6PS_5Cl electrolyte, operated at 3.0 mA cm^{-2} for one hour with a 7 MPa stack pressure. The images in (b) show (i-iii) initial plating of Li in pores away from the surface, (iv-end) leading to crack growth and short-circuiting. The scale bar is 100 μm. (c) Magnified areas for (i-iv) shows the initial plating of Li into "subsurface" pores and spallation leading to contact with the Li electrode and subsequent crack growth. Yellow arrows are used to highlight pores associated with spallation and red arrows are used to highlight pores associated with crack growth. The scale bar is 50 μm. Reproduced with permission from [100].

than electron imaging and their sensitivity to low-Atomic number (Z) elements, in particular Li, can make it challenging to interpret.[148] Scanning electron

microscopy (SEM) is better for high-resolution imaging, but it is difficult to prepare representative in-situ or *operando* samples in the high-vacuum environment of a microscope. Still, *operando* techniques within a microscope have been developed, including utilising a W probe as an electrode to cause Li to plate at the SSE surface.[149] Additionally, a prepared SSE cantilever demonstrated the effect of stress on plating, highlighting the importance of nano-scale cracks as nucleation points for dendritic growth.[150] This technique has its merits, but the small probe area leads to current densities more than an order of magnitude higher than utilised in normal ASSBs. An in-situ cell, connected to a potentiostat outside of the chamber, provided a more representative approach but still included modifications to allow the Li plating to be visible, such as a current collector which did not reach the edge of the electrolyte. Still, observation of preferential Li plating at grain boundaries via this method agrees with work done with XRT.[151]

FIB can be used to access 3D morphologies or sample cross-sections with SEM. While standard Ga FIB can only mill volumes on the order of 10s μm^3, Inductively Coupled Plasma (ICP) sources have enabled more massive ions, such as Xe, and higher currents to be used which has increased this to 100s μm^3 with only a marginal increase in voxel size.[152] In addition, cryo-FIB has been shown to reduce the artifacts induced in Li during milling.[141] An additional advantage is that FIB can be paired with other techniques within the microscope to obtain additional analysis. The most common techniques are EDX and Electron Backscatter Diffraction Spectroscopy (EBSD), to analyse composition and grain orientation, respectively. For example, Siniscalchi et al. used Plasma Focused-Ion Beam (PFIB)-SEM with EDX and the diffusivity of Mg in Li to investigate whether Li deposits in LLZO formed within the SSE or were connected to the Li-Mg electrode.[153]

Morphology of the SEI has not been widely investigated because of the challenges in preparing samples without damaging the thin, air- and beam-sensitive interphase. In one method, Li dendrites were mechanically detached from an electrode to investigate changes in the SEI with temperature. A mainly amorphous SEI with some crystalline Li_2S was observed which was thicker when formed at higher

temperatures. However, the full section from Li to the SSE was not preserved, making it difficult to draw further conclusions.[154] In-situ investigations remove the requirement to remove a sample from a cell. Li was brought into contact with an $Li_{1.4}Al_{0.4}Ge_{1.6}(PO_4)_3$ (LAGP) particle within the TEM, demonstrating the rapid volume change and cracking initiated by SEI formation.[155] This reduces sample damage, but is unrepresentative of a full battery cell. To improve on this, ultra-thin batteries are a step closer to a representative set-up. The effect of a Li_2S interlayer on PEO was investigated by electroplating a thin layer of Li onto a PEO-coated TEM grid, observing an amorphous layer with nm-sized crystallites.[156] The closest to a representative interphase was imaged via a full cryo-FIB liftout procedure with a thin and dense LiPON SSE. A multi-layered SEI was observed with an oxide next to the Li, then a N-rich layer, and finally a P-rich layer, as shown in Figure 1.10.[157]

1.5.4 Compositional Characterisation

Compositional changes at the Li-SSE interface are primarily due to SEI formation. As stated, the sensitivity and thinness of the SEI requires delicate sample preparation protocols and high-resolution imaging techniques. To investigate the properties of the SEI on a more manageable scale, a "bulk-SEI" was formed by heating Li_6PS_5Cl (LPSCl) and Li together in a crucible at 250 °C. This is clearly different from the conditions under which batteries are normally operated which could lead to significant deviations in morphology and properties. However, it did benchmark the ionic conductivity of the SEI formed with LPSCl, which was several orders of magnitude less than the ionic conductivity of the SSE.[158]

XPS has proven useful in analysing more realistic SEIs. In this case, the solid nature of SSEs is useful as, unlike liquid electrolytes, they do not evaporate in the vacuum chamber. The first study on the SEI with sulphide electrolytes investigated the interfacial chemistry between sulphides and Li metal using in-situ XPS. This showed that Li_2S, Li_3P, and Li_xP formed at the interface, but the SEI resistance stabilised after about 10 h.[106] It was assumed that LiX (Li halide) was also formed, but it was not possible to distinguish it from the SSE in XPS. For in-situ

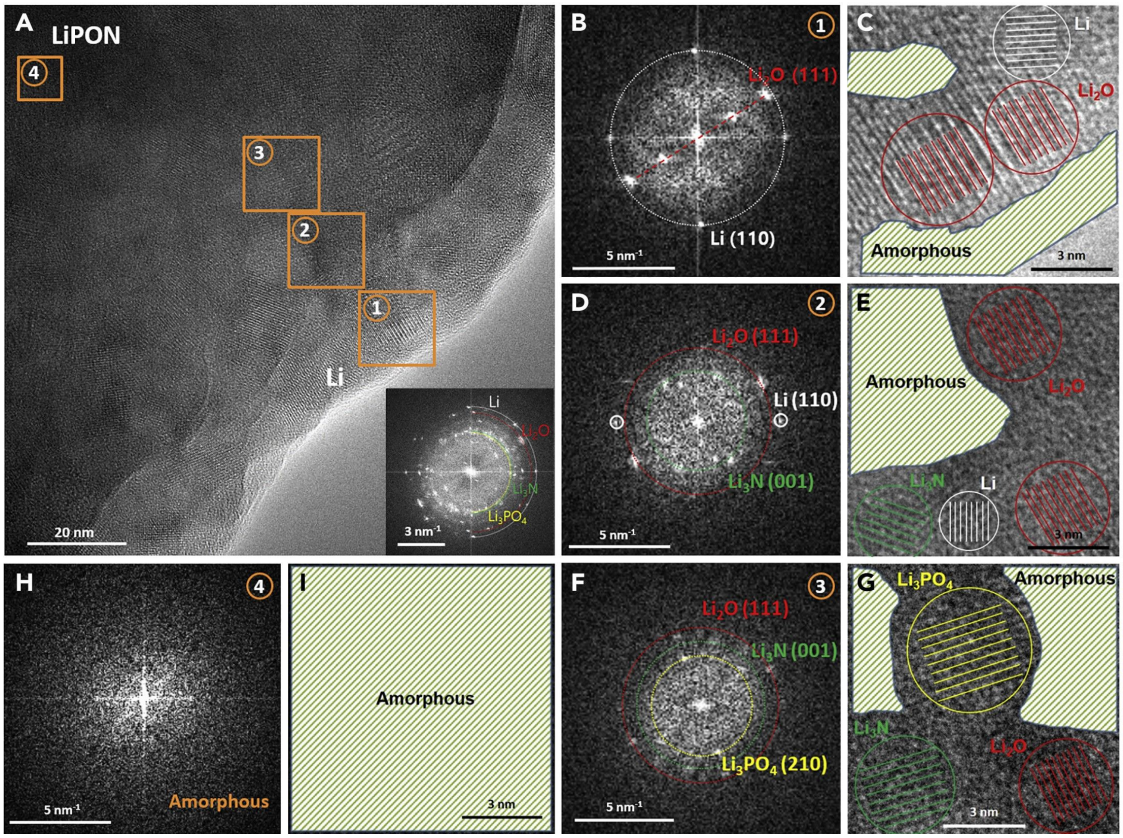


Figure 1.10: A High-resolution TEM (HRTEM) image taken via cryo-TEM. B,D,F,H FFTs of the corresponding areas 1-4 in subfigure A moving across the interface between Li and LiPON and then within the LiPON bulk. The radial distance for each compound is shown. C, E, G, I HRTEM images for regions 1-4 with the amorphous areas blocked out and the crystalline areas highlighted with colours and labels corresponding to their respectie components. Reproduced with permission from [157].

investigations, the electron gun in the XPS has been used as a "virtual electrode" to force Li to plate on top of the SSE within the chamber.[159] This technique was used to investigate the effect of applying different current densities on the SEI with LPSCl (to which I contributed SEM characterisation).[139] This demonstrated a kinetic limitation on the formation of Li_3P, as is shown schematically in Figure 1.11. XPS is useful for providing compositional information, but the wide field of view (FOV) limits spatial resolution, and the low penetration depth and difficult-to-quantify milling makes thickness challenging to determine.

Time of Flight - Secondary Ion Mass Spectrometry (ToF-SIMS) has been able to provide spatial and compositional characterisation to the cathode-electrolyte interface.[160, 161] It has also been applied to the Li-SSE interface in ASSBs where

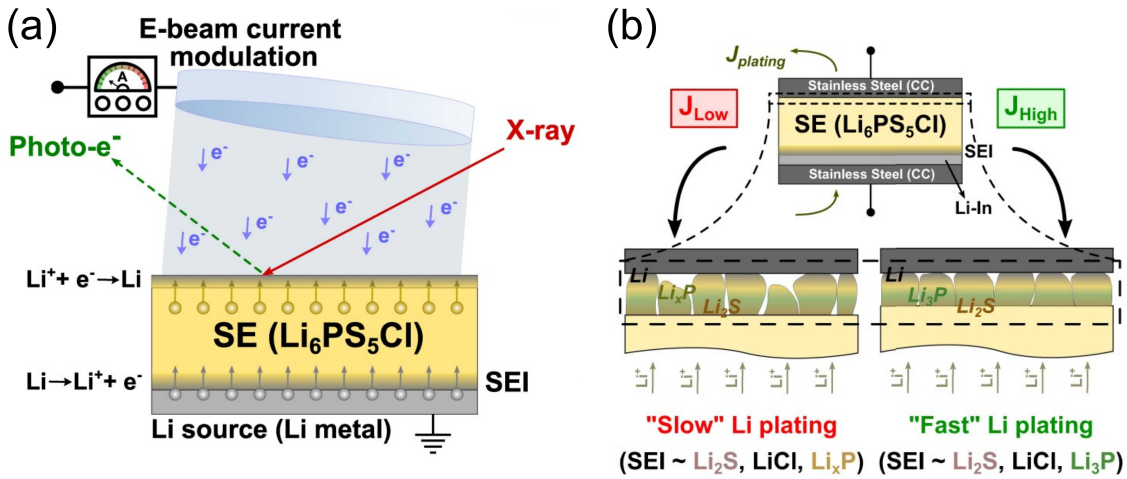


Figure 1.11: (a) Schematic of the *operando* XPS set-up showing the use of the electron beam as a "virtual" electrode so the SEI will form at the top surface where it can be analysed with XPS. (b) Schematic of the determined microstructure at low and high current density (J). Where P-species form closer to Li, and Li_xP species dominate at low rates and Li_3P dominates at higher rates. Reproduced with permission from [139].

it was able to identify the thickness and general composition of the SEI, leading to a classification of three types of SEI: stable (self-passivating), SEI (diffusion-limited), and Mixed-Conducting Interphase (MCI) (continuously growing, ionically conductive).The complexity of ToF-SIMS analysis makes exact understanding of the SEI difficult, but a bilayer structure was observed with a S-rich layer closer to the Li and a P-rich layer closer to the SSE.[125] Raman spectroscopy mapping has similarly combined spatial and compositional characterisation, but limitations to the Raman activity of SEI species and difficulty in cell design has limited its utility.[162, 163]

As mentioned above, cryo-TEM has demonstrated the most promise as a technique to analyse the SEI. Both spatial and compositional information can be obtained in a single experiment. With high-resolution imaging, visible lattice spacings can be converted to Fast Fourier Transform (FFT)s for d-spacing matching with components. Alternate detectors, such as EDX, can also provide compositional mapping of the sample. Spatio-compositional mapping can link components to highlight structure-property relationships. For example, a Li_2S interlayer was shown to encourage the formation of LiF, which is known to improve the performance of SEI layers.[156, 164] Cryo-Scanning Transmission Electron Microscopy (STEM)-Electron Energy Loss Spectroscopy (EELS) is another powerful tool to analyse

the chemical make-up of the SEI. When investigating the Li - LiPON interface a combination of FFT and cryo-STEM-EELS showed a layered structure with crystals of Li_3N, Li_3PO_4, and Li_2O, as shown in Figure 1.10.[157].

Electron Microscopy

Electron microscopy has proven invaluable in characterising the interfaces in ASSBs. FIB-SEM combined with EDX can give information on μm length scales about changes in the morphology of the interface, while EDX can help to separate different components. Cryo-TEM has lead to significant developments in the understanding of the SEI with liquid electrolytes, while it has only been investigated in a few instances with SSEs. Further work can broaden this knowledge, but there are significant challenges.

Li is difficult to characterise with electron microscopy because its low melting temperature (180.5°) makes it susceptible to heating damage. Its low Z makes it weakly diffracting for TEM and invisible in EDX without a windowless detector, as well as increasing its susceptibility to knock-on damage. Its poor mechanical properties make it difficult to handle in sample preparation without altering the morphology, and its extreme reactivity can lead to side reactions which are attributed to the SEI but are actually due to sample preparation, storage, or transport. Access to facilities which can accommodate the airless transfer needed to characterise battery materials in electron microscopy are increasing but remains an additional challenge. While these challenges are significant, the wealth of characterisation information available via electron microscopy makes it more than worth it to pursue it as a means of characterising interfaces in ASSBs.

1.6 Thesis Objectives

The aim of this thesis is to increase knowledge of the degradation mechanisms at the Li-SSE interface. The promising LPSCl argyrodite SSE will be investigated as an example, with the interface characterised via electron microscopy. This first chapter has outlined the relevant literature on this topic. The next chapter will introduce the

science underlying the key techniques applied throughout this thesis. The following three chapters will outline my contributions to this field. Chapter 3 will focus on the use of PFIB to characterise SSE with Li and Li alloys, with the work from this chapter having contributed to 3 papers [117, 165, 166]. Chapter 4 discusses a novel sample preparation technique to obtain thin sections of the Li-SEI-SSE interface for 4D-STEM analysis with minimal sample damage. Chapter 5 covers the analysis of these samples to produce, for the first time, spatio-compositional mapping of the SEI and statistical analysis of the relationships between the components. Chapters 4 and 5 contribute to a first author publication (in preparation) covering the characterisation of the SEI between Li and LPSCl-based SSEs.

I didn't want to just know the names of things. I remember really wanting to know how it all worked.

— Elizabeth Blackburn, Winner of the 2009 Nobel Prize for Physiology or Medicine

2 Methods Fundamentals

Contents

2.1 Electron Microscopy 38
2.1.1 Optics 38
2.1.2 Scanning Electron Microscopy 40
2.1.3 Transmission Electron Microscopy 43
2.1.4 Energy Dispersive X-ray Analysis 46
2.1.5 Focused Ion Beam Microscopy 47
2.1.6 Cryogenic Microsocopy 51
2.1.7 Beam Damage 52
2.2 X-Ray Techniques 55
2.2.1 X-Ray Diffraction 55
2.2.2 X-Ray Photoelectron Spectroscopy 56
2.3 Electrochemical Techniques 56
2.3.1 Electrochemical Impedance Spectroscopy 56
2.3.2 Chronopotiometry 57

2.1 Electron Microscopy

Electron microscopy allows a large degree of flexibility in imaging of materials science samples. Scientists were initially attracted to the increase in resolution due to the much shorter wavelength of electrons compared to photons (approximately 2-4 x10^{-3} nm compared to 400 - 700 nm, respectively). However, the other signals which can be collected due to the interactions between electrons and solids have led to a wide range of characterisation opportunities beyond simple imaging.

2.1.1 Optics

A light microscope uses highly-engineered glass lenses to focus photons to a specific point on the sample. Electron microscopes use electromagnetic 'lenses'. These are essentially coils of wire which generate a variable electromagnetic field. The difficulty in generating a perfect field means that there are aberrations inherent in the lenses such as chromatic aberrations, spherical aberrations, astigmatism, and coma. Before use of the microscope, alignments should be done to minimise the impact of any of these aberrations on the image.

In a scanning electron microscope (SEM), the electron beam is focused to a point on the sample surface. In a transmission electron microscope (TEM), the electron beam goes through the sample in a roughly parallel beam and is then focused down onto a screen using a second set of lenses. An example of the difference in optics can be seen in Figure 2.1. Besides the clear difference in the location of the sample in relation to the lenses, the contents of the microscopes are not significantly different, with both consisting of an electron gun, sets of condenser and objective lenses, with their corresponding apertures and finally projector lenses at the bottom of the microscope in the case of TEMs. TEMs are significantly taller than SEM because higher accelerating voltages are used meaning that the longer distances are needed to properly focus the electron beams. There are now both scanning electron and transmission electron microscopes where STEM can be conducted. This involves a transmitted electron beam which has been focused to a point being scanned across the sample using scanning coils. The location of these are shown in Figure 2.1.

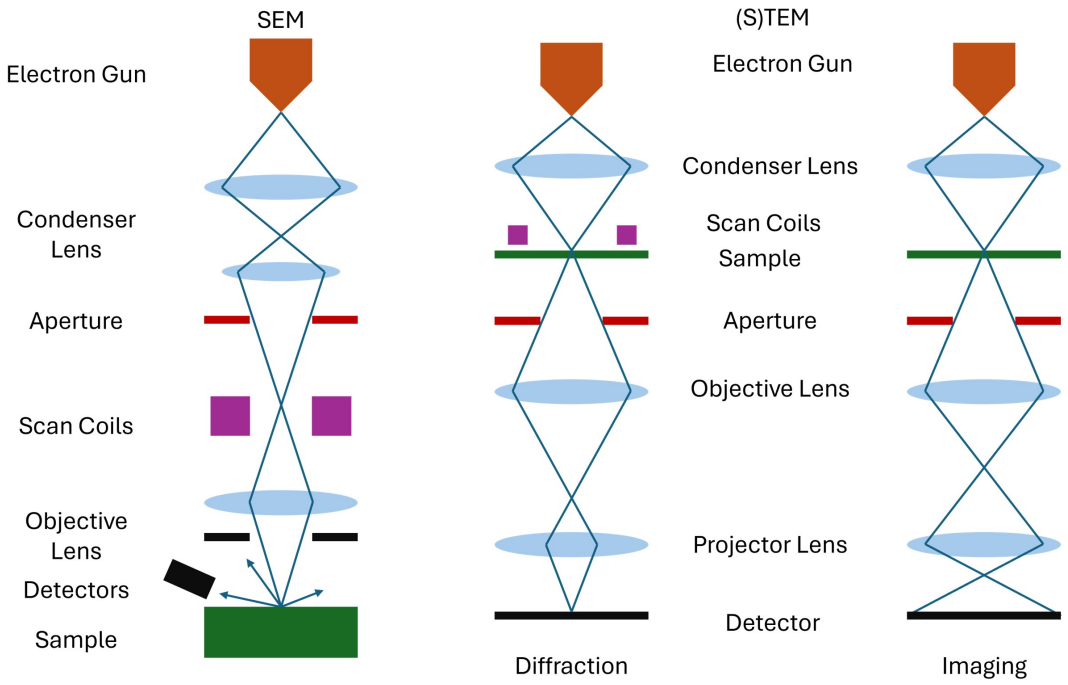


Figure 2.1: Simple comparison between SEM and TEM microscope optics (STEM would include scan coils).

Resolution limits in a microscope are described by Rayleigh's criterion (Equation 2.1). Where d is the limit of resolution, λ is the wavelength of the imaging radiation, n_r is the index of refraction of the medium between the point source and the lens, and α is the semiangle onto the sample. $n_r sin(\alpha)$ is referred to as the numerical aperture. This was developed from Abbe's equations based on the idea of Airy disks, which are rings of intensity produced by an aperture as radiation goes through them. The Rayleigh criterion states that if the centre (maximum) of one diffraction pattern (Airy disk) is over the minimum of another, they are just resolvable. From Equation 2.1 we can see that to improve the resolution we can decrease the wavelength, increase α, for example by using a large aperture, and increase the index of refraction. Changing the index of refraction is not relevant for electron microscopes because they must be operated in a vacuum, but sometimes optical microscopes can be operated with oil immersion lenses to improve their resolution.[167] These theoretical resolution limits are not often reached because of various aberrations in the microscope such as chromatic aberration (a range of wavelengths which are all refracted slightly

differently), and spherical aberration (differences in strength across a lens leading to different beam trajectories focusing at different points).

$$d = \frac{0.612\lambda}{n_r sin(\alpha)} \tag{2.1}$$

2.1.2 Scanning Electron Microscopy

There are two main electron signals used for imaging in the SEM, Secondary electrons (SE) and Back-scattered electrons (BSE). The differentiation between these two signal types is the amount of energy that the electron escaping the sample surface has; BSE have > 50 eV, SE have < 50 eV. The difference in energy level is due to their interactions within the sample. BSE have interacted elastically with the atomic nuclei in the sample, causing $> 90°$ direction changes and an incident electron to escape back out of the sample surface. SE are generated due to inelastic interactions between the incident beam and electrons in the sample, leading to outer electrons in the sample being ejected from the sample. As shown in Figure 2.2, because of the difference in the mechanism of their generation, BSE can originate from deeper within the sample (have a larger interaction volume), while SE give more surface-sensitive information. BSE emission is much more dependent on the Z of the sample, while SE emission (δ) varies less.[168]

The relationship between Z and BSE emission can be summarised in Equation 2.2 below:

$$\eta = \frac{\eta_{BSE}}{\eta_B} = -0.0254 + 0.016Z - 1.86 \times 10^{-4}Z^2 + 8.3 \times 10^{-7}Z^3 \tag{2.2}$$

Where η is the backscatter coefficient, or the ratio between the incident beam electrons (η_B) and the backscattered electrons (η_{BSE}). The relationship between SE and Z is more complicated. They are generated along the entire length of the incident electron path, but as they have much lower energy they can only escape if they are not scattered too many times, which relates to the λ_p (mean free path), which is the average distance an electron moves before being scattered in the sample. SE must be within $5\lambda_p$ of the surface to be able to escape, as defined in Equation 2.3.[169]

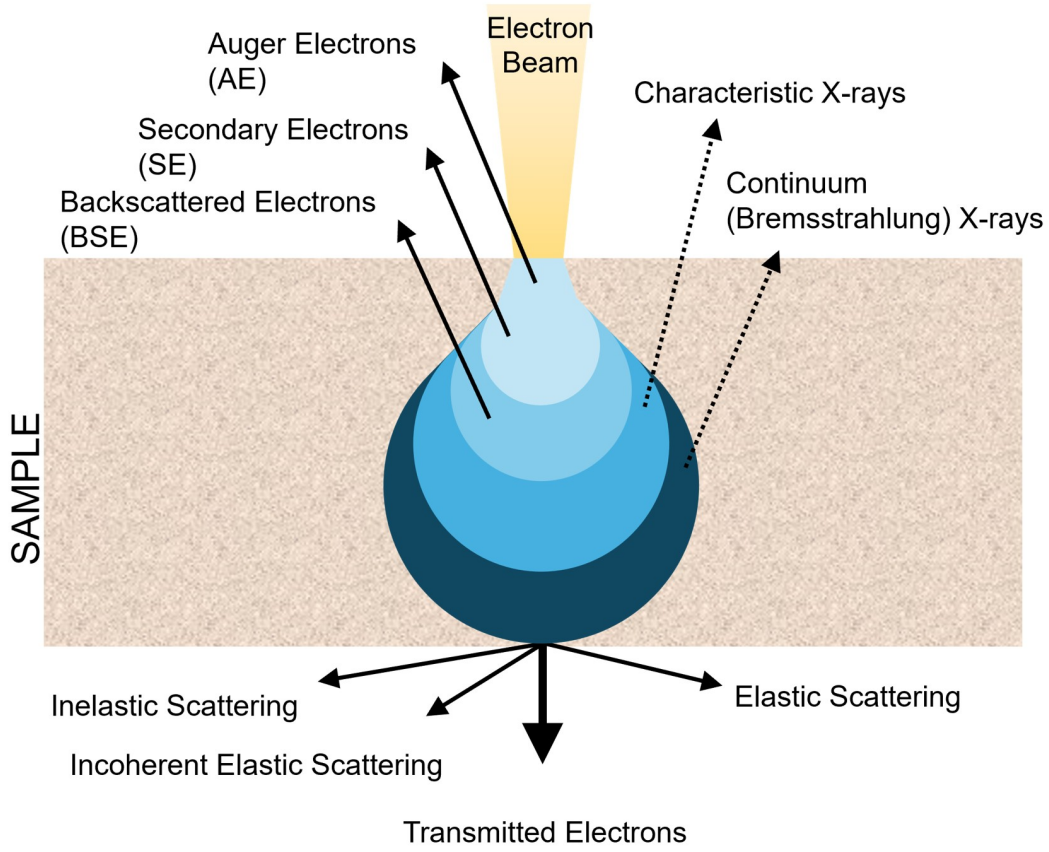


Figure 2.2: Diagram of some of the ways an electron can interact with a sample, with an approximate comparison of the variation in interaction volumes associated with different signals.

$$\lambda_p = \frac{A}{N_0 \rho \sigma_{atom}} \tag{2.3}$$

Where A is the atomic weight of the scattering scattering atoms, N_0 is Avogadro's number, ρ is the density of the sample, and σ_{atom} is the atomic scattering cross-section. Calculation of the exact scattering cross-section can become quite complicated, but it broadly depends on the atomic radius of the sample atoms and what is considered a significant deflection angle. Because SEs can be produced when an incident electron is sufficiently close to the surface both on entry (SE_1) and exit (SE_2), it is difficult to quantify their exact relationship with Z, but it is a much weaker relationship than for BSE. Additionally, SE are much more strongly affected by surface morphology effects. For example, any edges or ridges will appear

brighter as it is easier for the SEs to escape the surface, and surface contamination will have a greater effect on the image formed.[168]

The incident beam energy and angle of incidence on the sample also have a huge effect on the signal electrons which exit the sample. A larger incident beam energy will increase the interaction volume as the electrons start with more energy and lose it at a lower rate. For low beam energies there is a point at which the BSE and SE interaction depth are approximately equal, called the upper crossover point. This is because the escape depth for SE does not change with beam energy, but the interaction depth for BSE decreases. Additionally, any angle between the incident beam and the surface of the sample will decrease the distance electrons will have to travel to escape from the surface This will increase electron signal but reduce the resolution as electrons which have travelled further from the point of incidence may remain close enough to the surface to escape.

When operating the SEM, there are four main parameters to consider: d_p (electron probe size), i_p (electron probe current), α_p (electron probe convergence angle), and V_0 (electron probe accelerating voltage). For high-resolution imaging, d_p should be kept as small as possible, but this will limit i_p which can reduce the amount of signal obtained. i_p must be sufficiently high to obtain signal higher than the background noise level. Charging effects and beam sensitivity of the sample must also be considered, which may limit the current which can be used. α_p mostly affects the depth-of-field, which is one of the biggest advantages of SEM over visible-light microscopes. By having a low α_p, the beam diameter does not change significantly over a range of heights, leading to reasonable resolution across rough sample surfaces. Finally, V_0 has a large impact on resolution as it affects both the electron yield from the sample and the interaction volume from which they originate. A low V_0 (≤ 5 kV) will give a surface-sensitive image but also a lower electron yield, while a higher V_0 (20 - 30 kV) will give higher electron yields, but also significantly higher interaction volumes which can lower resolution. These factors must be balanced based on the goal of the imaging session to obtain images with both high signal and resolution.

2.1.3 Transmission Electron Microscopy

TEM forms images with electrons that have been transmitted through a sample, rather than deflected back out through the top surface. These can also be seen schematically in Figure 2.2. Because the electrons are transmitted through the sample, it must be sufficiently thin to be electron transparent. This complicates sample preparation further, but also enables higher resolutions to be achieved. Samples are generally required to be on the order of 100 nm thick, although with some low-Z materials and higher accelerating voltages thicker samples can be imaged. Thicker samples may still reduce resolution due to multiple scattering effects, electron energy loss, and beam attenuation.

The electron beam interaction with the sample are as fundamental to TEM as they are to SEM. As with SEM, they main distinction is between electrons which interact elastically or inelastically with the sample, which can vastly change the scattering angle. Generally, as the samples are so thin a single interaction (kinematical) approximation can be used, but if thicker samples are used there may be plural electron scattering events.[169]

TEM analysis occurs in the imaging and diffraction planes. This can give concurrent information on the crystallinity, composition, and structure of the sample. In the imaging plane, mass-thickness, diffraction and phase contrast are the most common mechanisms. Mass-thickness contrast is simply due to a higher degree of scattering in higher thickness or higher mass regions (inelastic scattering $\propto Z^2$) which causes them to appear darker in Bright Field (BF) images and brighter in Dark Field (DF) images. Another contrast mechanism is due to crystallinity. With crystalline samples there can be significant diffraction contrast if Bragg conditions are met, leading to dark areas in BF image and corresponding bright areas in DF. [167]

Electrons are charged particles so they interact with both the nucleus and electron cloud of materials, leading to stronger diffraction than X-Rays, which are also commonly used for diffraction studies. This is particularly true for low-Z materials. In standard TEM the diffraction of the entire area under the parallel electron beam is considered. If smaller areas want to be investigated selective

apertures can be introduced, this is called Selected Area Electron Diffraction (SAED). The most important equation in diffraction is Bragg's law (Equation 2.4):

$$n\lambda = 2dsin(\theta) \tag{2.4}$$

Where n is the order of the reflection, λ is the wavelength, d is the spacing of the planes in the sample and θ is the Bragg angle through which diffraction occurs. When constructive interference occurs between the rays of electrons bright spots occur at specific distances from the non-diffracted beam, and different planes will produce spots at specific angles to one another which can be used to identify the orientation of crystals in specimens. It is also important to consider the effect of the composition on the intensity of the diffraction. This can be summarised by the atomic scattering factor (f(θ)) in Equation 2.5:

$$f(\theta) = \frac{(1 + \frac{E_0}{m_0c^2})}{8\pi^2 a_0}(\frac{\lambda}{sin(\frac{\theta}{2})})^2(Z - f_x) \tag{2.5}$$

Where E_0 is beam energy, m_0 is the rest mass of an electron, c is the speed of light, a_0 is the Bohr radius of the scattering atom, and f_x is the X-Ray is scattering factor (which are tabulated). It can be seen that the atomic scattering factor will decrease with increasing θ, decrease with decreasing λ (i.e. as accelerating voltage increases), and increase with increasing Z. To extend this from a single atom to a crystal structure the atomic scattering is summed over the unit cell of a crystal to become the structure factor as shown in Equation (2.6):

$$F(\theta) = \sum_{i}^{\infty} f_i e^{2\pi i(hx_i + ky_i + lz_i)} \tag{2.6}$$

Where i refers to the number of atoms in the unit cell, (x,y,z) denote the position of the atom within the unit cell and (h,k,l) give the atomic plane. The degree of crystallinity will also affect the intensity of the diffraction. More crystalline samples will produce brighter, more defined spots, while polycrystalline or amorphous samples will contain more background noise leading to less definition of the spots, and instead of producing spots in diffraction may produce rings.[169]

STEM imaging is a variation on TEM where a focused beam is scanned across a sample surface and detectors are in the diffraction plane. A BF STEM image is mathematically equivalent to a TEM image. By placing hollow, circular detectors at specific radii in the microscope, High-angle annular dark field (HAADF) images can be obtained which give complementary information. They collect incoherently scattered electrons, which excludes some of the interference effects from conventional TEM and allow for easy interpretation of images where intensity is approximately proportional to Z^2.[170]

4D-STEM

4D-STEM is a technique in which a 2D diffraction pattern is recorded at every position in a 2D array of electron probe positions. These add up to the four dimensions included in 4D-STEM. It is essentially a series of diffraction experiments across each pixel of an image in real space, generating a diffraction pattern per pixel. With the introduction of detectors which can cope with the required high speeds of the STEM scanning rate (ms - μs), such as direct electron detectors, 4D-STEM has become a much more accessible technique.

4D-STEM can roughly be categorised into two types, which are somewhat allegorical to TEM and STEM. Nano-Beam Electron Diffraction (NBED) involves scanning of a parallel beam while Convergent-Beam Electron Diffraction (CBED) scans convergent beam as shown in Figure 2.3. The difference in convergence angle means that the diffraction disks in CBED overlap, whereas in NBED they are separated.[171] Depending on the experiment, one may be preferable over the other as a higher convergence angle means that the real space resolution is higher, while a lower convergence angle means that there is lower real space resolution but higher reciprocal space resolution, which can help with certain types of analysis, such as strain mapping.[172] A combination of improved detector efficiency and image processing has enabled lower dose high resolution TEM (< 10 e^- $Å^{-2}$), but contrast in these images can be more difficult to interpret. 4D-STEM can fill this gap to provide low-dose, high-resolution imaging of beam-sensitive materials.[173]

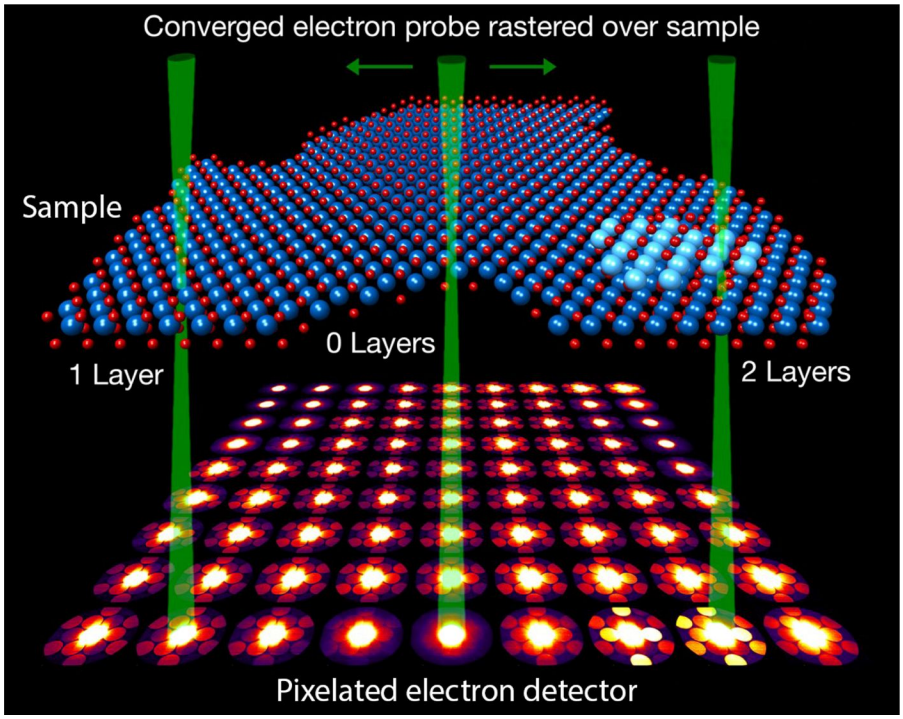


Figure 2.3: Diagram of 4D-STEM with beam rastering over a 2D material with different areas of the sample and showing differences in the diffraction patterns. The green columns represent STEM beams transmitting through different thicknesses of the sample as labeled. Reproduced with permission from [172].

The large data sets generated during 4D-STEM experiments open up many analysis possibilities. One of the simplest ways is to create virtual images by placing virtual detectors onto the diffraction patterns. This can show the location of areas of crystallinity or different phases. Effectively, this enables many opportunities and time for choosing the location of detectors. Phase mapping is another useful tool which uses a classification algorithm to group similar diffraction patterns. Strain mapping can also be accomplished by calculating changes in the Bragg peak position across the sample. There are many other opportunities for analysis using 4D-STEM data, and it is important for users to keep in mind the goal of their experiments when choosing parameters, particularly the convergence angle.[174]

2.1.4 Energy Dispersive X-ray Analysis

Alongside the signals generated directly from electrons, there are a number of signals generated by the electrons interacting with the solid which can give information

on the the chemistry of the sample, as can be seen in Figure 2.2. EDX can give information on the elemental composition of a sample, although exact quantification requires careful sample preparation. When incident electrons interact with electron clouds in the sample, they excite electrons, then when they relax back to their original energy level they release the excess energy in the form of a photon of a characteristic wavelength. These photons are collected by a specific detector to generate a spectrum at each point. The data can then be automatically attributed to specific elements and analysed as individual spectra, line scans, or maps. There will always be a significant background due to continuum or Bremsstrahlung radiation, which is generated during inelastic scattering of electrons. Therefore, the signal from the characteristic X-Rays must be sufficiently above this level to be registered.

It should be noted that, for SEM work, the interaction volume of these X-Rays are much deeper than for both BSE and SE. Especially for low Z materials, such as battery materials, the accelerating voltage must be chosen carefully as the resolution can be significantly impacted by using a high accelerating voltage or the signal an be convoluted by penetrating too deep into the sample and generating X-Rays from behind what is visible in the SEM. However, if the accelerating voltage is not sufficiently high the incident electrons may not have enough energy to generate characteristic X-Rays.[168] Additionally, low-Z elements tend to return to their ground state by Auger electron emission rather than X-ray emission and as their X-Rays are lower energy they are more easily reabsorbed by the sample or screens protecting the detector.[167] As battery materials are both low-Z and often beam-sensitive, it is imperative that images are taken before and after an EDX map is recorded so that any damage can be taken into account when analysing the results.

2.1.5 Focused Ion Beam Microscopy

FIB microscopy can be used to do three things: image, deposit material, or remove material, an example of all three can be seen in Figure 2.4 (B). Imaging can either be done in SE mode or Secondary Ion (SI) mode. In terms of instrumentation, it employs a SEM column with an ion beam column at an angle to to the SEM

as shown in Figure 2.4 (A). It also includes a Gas Injection System (GIS) which enables organometallic gases to be injected close to the sample. These are then decomposed precisely by an ion beam to deposit material. One of the most common uses for this is to deposit a Pt or W protective layer prior to sample thinning for TEM sample preparation. Modern FIBs will also contain a manipulator needle which is used during TEM sample lift-outs to transfer the region of interest from the sample to a TEM grid. Finally, they will often contain other detectors, such as EDX detectors, which can be used in conjunction with SEM and FIB to give additional information during 3D-sectioning.

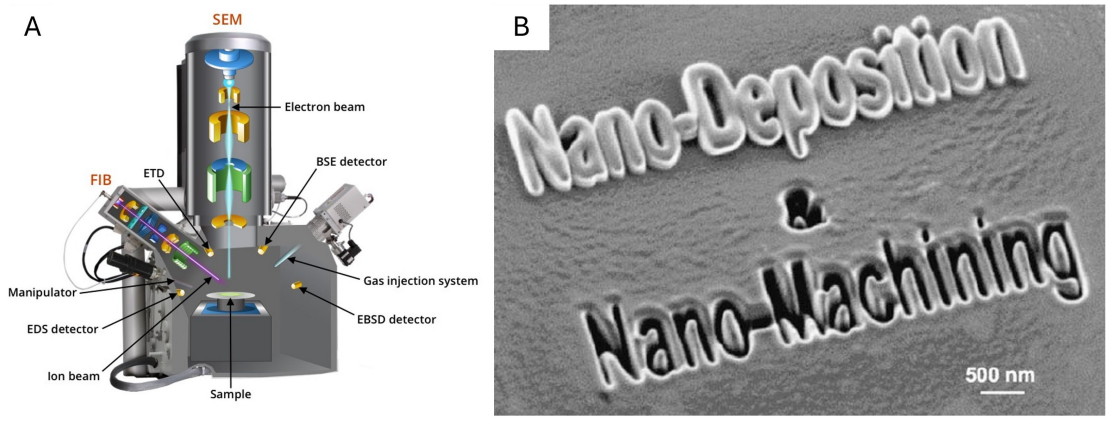


Figure 2.4: (A) Diagram of focused ion beam microscope. Reproduced with permission from MyScope. (B) Example of a focused ion beam used to deposit material and remove material on a tiny scale with high precision, then imaged using the ion beam. Reproduced with permission from Fibics International.

The ion beam is generated at a gun in an allegorious position to the electron gun in a SEM. The first FIBs used a Liquid Metal Ion Source (LMIS), which was able to provide a beam focused down to a radius of about 5 nm by heating a metal ion (usually Ga^+ due to its low melting point of 29.8 °C, low volatility, and low vapour pressure), which then flows to the end of a W filament. An electric field is applied to pull off the ions from the tip of the Taylor cone which forms.[175] More recently, a plasma source has been developed which not only can work with a wider range of materials (for example Xe, Ar, and O) but can also tolerate much higher currents which increases the rate at which cuts can be made.[176] The variation in

materials is particularly useful for batteries as Ga is known to alloy with Li which can induce milling artifacts. It also enables milling through thicker solid electrolyte layers which would have take prohibitively long time periods otherwise.

The mechanisms governing the milling and image generation from FIB are based on complex ion-solid interactions, summarised in Fig. 2.5. When an incident ion reaches the solid specimen it undergoes a series of elastic collisions known as a collision cascade.There are three regimes in the collision cascade, the first is the single knock-on regime where incident ions do not have sufficient energy to generate much sputtering. The second is the linear cascade regime where a cascade forms but with minimal enough energy that multiple collisions can be disregarded. The third is the spike regime where the incident ion has such a large momentum that the majority of atoms in the volume move during the collision cascade.[177] A surface particle is ejected if it receives kinetic energy greater than the surface binding energy, if it is ionized it is known as a SI. SE are generated as a result of inelastic collisions. Both SE and SI can be used to form images, but the number of SE generated is usually several orders of magnitude higher so it is the major imaging mechanism. It is important to note that even simply imaging with the ion beam is a destructive process based on the same mechanisms and therefore should be used carefully so as not to induce artifacts.[175]

There are a few fundamental concepts which are useful when considering solid-ion interactions in the FIB. The first is the Projected Range (R_p) as shown in Fig. 2.5, which is the longitudinal projected range for a single ion. The overall Range (R) is the total distance the incident ion travels. The Implantation Depth (X_s) is equal to R_p when the incident ion impinges on the sample at a right angle. Both of these values are usually considered statistically rather than for a single ion as the stopping range of an ion is a random process, with an approximately Gaussian distribution. If the sample is crystalline, crystallographic channelling effects can lead to X_s being much larger than R_p, as ions will travel further down the crystal channels.[178]

The distance an ion travels in a sample during FIB sputtering depends on the mass and atomic numbers of the incident ion and sample, as well as the incident

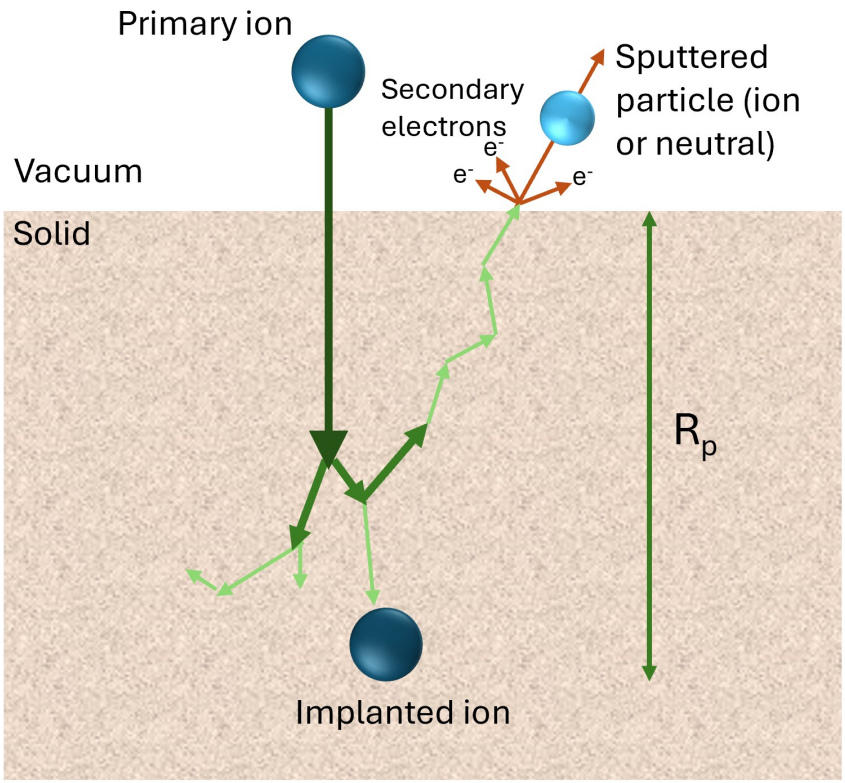


Figure 2.5: Diagram of sputtering process and ion-solid interactions. Adapted from [178].

energy. This is because the interactions are a combination of transfer of momentum and interatomic potential. The Stopping Power (S(E)) is the term used for the energy transferred incorporating the different mechanisms and angles of scatter. It can be modelled, and has been shown to correlate with density, and even more strongly with melting temperature.[175] This means that low density, low melting point materials tend to have low S(E).

When undertaking FIB sputtering, there are a few practical matters which should be considered. The first is the redeposition of material. If there is not sufficient space for material to escape after it has been sputtered (for example, if you have milled a narrow trench) material can redeposit on the walls and in pores in the sample, changing the morphology or the location of elemental components in EDX. Different milling patterns are now built into FIBs which help to minimise this problem, and by polishing the surface at a lower energy, you reduce the sputter

yield and therefore reduce the chance for redeposition while removing any material which may have been deposited during earlier, higher energy, rough mills. However, especially in porous samples, care should be taken to ensure that the sputtering yield is not so high as to lead to redeposition into the sample. The second is curtaining, which is the appearance of lines in the sample parallel to the incident ions due to the collision cascades. These are more prominent at higher incident energies because the individual collision cascades are stronger. They are also more prominent in porous samples because the pores can disrupt cascades leading to less milling below them. To avoid this issue, polishing at lower accelerating voltages can be done as well as using a rocking polish stage, if one is available, which tilts the sample back and forth during milling to reduce the effects of milling in a single direction.

2.1.6 Cryogenic Microsocopy

Cryogenic TEM applied to imaging biomolecules won the Nobel prize for Chemistry in 2017.[179] It has more recently been applied to battery materials [56, 180] because these materials are also beam sensitive. The other sample preparation difficulty of battery materials is that they are often air-sensitive, which adds an extra degree of difficulty when preparing, storing, and loading samples as they must be kept in an inert atmosphere or cold enough that any reactions are prevented by kinetic limitations. Submersion in liquid N has been shown to effectively prevent reactions, even with Li metal which would normally react with N_2.[56, 137] This hardware is only beginning to be implemented for physical science characterisation, for example at the Imperial Centre for Cryo Microscopy of Materials. Cryogenic microscopy minimises damage via heating, radiolysis and diffusion, more detail on this is given in the next section.[181, 182] This has been shown to be very helpful for battery materials, especially materials like Li which have a low melting temperature. There are many other types of beam damage which must also be taken into account and can still limit the electron and ion dose which can be used.

2.1.7 Beam Damage

Electron Beams

The beam damage effects for both SEM and TEM are similar, but are often far more noticeable in TEM because the higher electron energy and higher resolution means even small changes in the structure are detected. EDX also requires a higher electron dose for TEM than SEM because the samples are so thin, limiting the signal output. Some of the common mechanisms are shown in Figure 2.6. Of these, all apply to TEM, but only heating and charging are usually significant in SEM.

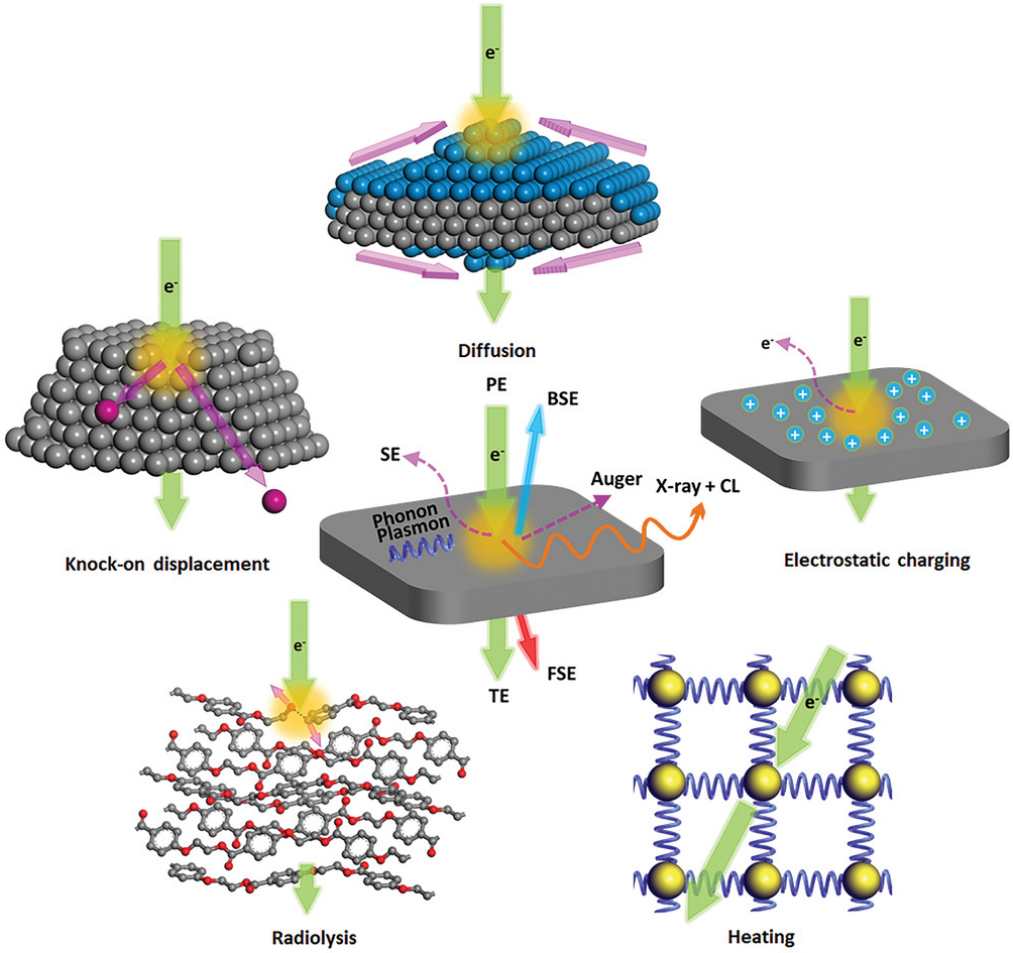


Figure 2.6: Diagrams representing some of the different damage mechanisms between a high-energy electron beam and a sample. PE, SE, TE, FSE, BSE, and CL refer to primary, secondary, transmitted, forwardscattering, and backscattering electrons and cathodoluminescence, respectively. Reproduced with permission from [183]

Heating of the sample is due to inelastic collisions between the incident electrons and the sample, increasing the kinetic energy of the sample. The severity of this

effect on the sample depends on the sample's heat transfer coefficient, its sensitivity to heat, the electron dose, and incident energy.[184] It can lead to melting, phase changes, and thermal expansion of the sample structure in sensitive samples. Cooling holders, such as cryogenic holders, are very useful in this case and can minimise or eliminate the melting problem, but may also cause structural changes due to thermal contraction or phase changes, and difficulty imaging due to ice build-up during loading and sample movement under the beam.[183]

Knock-on damage (also known as radiation damage) is caused by elastic collisions between high-energy electrons and sample nuclei, causing them to be displaced from their atomic sites. This induces artifacts in the crystal structure. It depends on both the sample atomic mass and the threshold displacement energy, which is the energy required to knock an atom off its site leading to atomic displacement or mass loss. The minimum beam energy for knock-on damage to be problematic can be calculated by using the maximum kinetic energy which could be transferred by the incident electron. Defects or surfaces in the sample will lead to lower binding energies, potentially leading to knock-on damage below this threshold. Low Z samples tend to have lower binding energies, making this a significant mechanism for them. As the electron beam energy increases the damage cross-section decreases, and it has been shown that the magnitude of the cross-section has a larger role than the atomic mass.[184] It can be observed as a gradual amorphisation of the sample under the beam, making it more difficult to interpret the crystal structure. For some samples, lower accelerating voltages can help to avoid this mechanism if they remain under the energy threshold. If that is not possible, lower electron doses or higher accelerating voltages to reduce the damage cross-section can be used.[185]

Radiolysis (ionization) is similar to radiation damage, but rather than knocking off an atom, an electron is knocked off due to inelastic interactions. The resulting radical can then react with other atoms in the sample, driven by thermal vibrations, Coulomb interactions, or conservation of energy-momentum.[183] The damage cross-section for radiolysis decreases with increasing incident energy, and it is often the dominant damage mechanism in non-metals. The secondary effects due

to the propagation of dissociated electrons or radical species can lead to larger impacts from radiolysis. For low-Z insulating materials, such as polymers or solid electrolytes, it can be more beneficial to use a higher accelerating voltage to reduce the radiolysis damage cross-section.[186]

Radiation can speed the rate of diffusion along the surface of the sample. In some cases this can lead to 'sample healing' if diffusion occurs filling holes generated in the sample. It can also cause surface diffusion of hydrocarbons over the area of interest, reducing contrast.[182] Finally, electrostatic charging is most common in insulating materials and will get worse if low temperatures are used to manage other damage mechanisms. This can be managed by coating the sample.[183, 186]

Different damage mechanisms may depend more on the dose or the dose rate. Common ways to determine the damage mechanism include monitoring the diffraction pattern for changes in spot brightness (changes in crystallinity), EELS spectra for changes in coordination environments, or changes in EDX and EELS for evidence of mass loss. It is useful to know the dominant mechanism for the material being imaged so appropriate measures can be taken to avoid damage to the specimen.[183]

Ion Beams

Some mechanisms for beam damage from ion beams is similar to electron beams. Notably, heat damage has the same mechanism, although as ions are more massive they have more momentum and can lead to greater heat transfer. Some of this is mitigated by sputtering removing the highest-energy atoms but ion implantation (discussed below) has the opposite effect. With the low melting temperature of Li this is a major concern. Cryogenic cooling stages for FIB have made it possible mill through Li-metal batteries.[141]

As discussed above, ions can become implanted in the material leading to changes in the structure of the sample. The implantation depth increases with incident energy and is also highly dependent on the incident angle, a grazing angle will have a much lower X_s than an incident beam normal to the sample surface. Larger incident

ions have lower X_s because it requires more energy for them to fit into the sample structure, therefore this is less of an issue when using a plasma FIB with Xe, for example.[176] Additionally, using a grazing angle for all polishing can mitigate this problem. The material being milled will also have a large impact, as some materials, such as Cu and Li, will alloy with Ga and form additional phases during milling.[187]

Amorphisation of the sample can occur during ion milling as well as electron imaging, but the mechanism is different. With ion milling the cause of bond breaking is the high-energy impact of the incident ion with the sample, which can cause a sample atom to be fully sputtered away, as is often intended, or knock it off its site but remain in the sample, leading to amorphisation. This is a very common in the FIB, and can be minimised by low-energy polishing as a final step to remove the amorphised layer.[188] It is common to use an Ar^+ ion for this step as the lighter ion is less likely to lead to further amorphisation, but its low mass also means that it would take a long time to sputter for the full sample preparation.[189]

Heavy ion bombardment can lead to significant changes in sample morphology, such as cracking. This is due to a variety of the mechanisms mentioned above notably ion implantation and heating. To balance time taken for milling and minimisation of artifact production, checks should be done as to what current density the sample can receive without leading to significant morphological changes.[175]

2.2 X-Ray Techniques

2.2.1 X-Ray Diffraction

Powder X-Ray diffraction (XRD) is used widely in materials science as it can give a wealth of information on the structure of a material, including its atomic arrangement, lattice spacing, crystallite size, and more. It is conducted by placing a powder sample between a X-Ray source and detector, then rotating it through a series of angles. The variation in signal which arrives at the detector is determined by Bragg's law, which is shown above in Equation 2.4. More information on diffraction can be found in the TEM section shown above. As X-Rays do not carry charge, they

only interact with the electron cloud in materials. This means they are diffracted more weakly than electrons, in particular by low-Z elements.

All XRD in this thesis was completed by colleagues.

2.2.2 X-Ray Photoelectron Spectroscopy

XPS is a surface-sensitive technique which involves X-Rays interacting with a sample, resulting in the ejection of electrons via the photoelectric effect. The specific energies of the photoelectrons are equivalent to the binding energy of the chemical environment they originated from. The equation from which the binding energy can be determined is:

$$E_{\text{binding}} = E_{\text{photon}} - (E_{\text{kinetic}+\phi})$$

The binding energy can be used to determine the elemental composition and chemical state of the sample. It is a very surface-sensitive technique as the photoelectrons only originate from the top few nm of the sample, but depth profiling can be done in between acquisitions to obtain depth information.

All XPS in this thesis was completed by colleagues.

2.3 Electrochemical Techniques

2.3.1 Electrochemical Impedance Spectroscopy

EIS is a very complex technique, which will only be described briefly here as it is purely used as supporting information. Readers interested further are referred to Lazanas and Prodromidis.[190] EIS applies an oscillating potential or current across an electrochemical cell across a range of frequencies. The changes in the resulting sine wave can be interpreted to determine the impedance at different frequencies, which can then be associated with processes at different time scales. Longer time-scales are often associated with diffusion processes (low frequency) and shorter time-scales are associated bulk resistance (high frequency). To separate out the different components of the EIS spectra, equivalent circuits are often used, where each part of the circuit is linked to a specific physical meaning, for example SEI

resistance. The attribution of this physical meaning is challenging (or impossible) without physical characterisation of the system.

2.3.2 Chronopotiometry

In this technique a constant current is applied by a potentiostat between the working and counter electrodes. The potential is recorded as the difference between the working electrode and the counter electrodes in a 2-electrode set-up or the working and reference electrodes in a 3-electrode set-up. The potential recorded will deviate from theoretical by an amount described as the η (overpotential), which is due to resistive processes in the electrochemical system. The different processes can be split out into different components of the η, such as ohmic and activation resistance. These are due to the resistance of the electrolyte and the charge-transfer reaction, respectively.[5]

I am among those that thinks science has great beauty.

—Marie Skłodowska-Curie, first woman to win a Nobel Prize and the first person to win a Nobel Prize twice

3

Insights into the Solid Electrolyte - Li-based Electrode Interface from Plasma Focused-Ion Beam Microscopy

Contents

3.1 Abstract 60
3.2 Introduction 60
3.3 Results and Discussion 63
3.3.1 Li-Mg Alloy: Alternative to Li metal? 63
3.3.2 Li-Mg - Solid Electrolyte Interface 67
3.3.3 Microstructural Changes in Li-In Alloys 72
3.3.4 Developing Thin Solid Electrolytes 78
3.3.5 Effect of Interlayers and Temperature on Li morphology 84
3.4 Conclusion 87
3.5 Experimental Detail 88
3.5.1 Plasma Focused Ion Beam - Scanning Electron Microscopy 88
3.5.2 Energy Dispersive X-Ray Spectroscopy 89
3.5.3 Transmission Electron Microscopy 89
3.5.4 Sample Preparation 89

3.1 Abstract

The Li-solid state electrolyte (SSE) interface is the site of key degradation mechanisms, but physical characterisation is challenging because of the air sensitivity, low X-Ray emission, and poor mechanical properties of Li metal and many SSEs. Here, a combination of plasma focused-ion beam (PFIB) and scanning electron microscopy (SEM) with an inert transfer system is used to overcome these challenges and better understand the microstructural evolution of this interface. First, room-temperature PFIB was used to investigate the interface between a Li_6PS_5Cl SSE and Li-Mg alloys, demonstrating that these alloys can be used as a proxy for Li for characterisation without a cryo-FIB. The stability of Li alloys to ion milling enables the investigation of Li-Mg and Li-In. Li-Mg is shown not to prevent voiding or dendritic growth in all-solid-state batteries, limiting its practical utility. The effect of Li-In microstructure on stripping of this highly-utilised reference electrode is also determined. A cryogenic stage operated at -150 °C is needed to characterise the interface between Li metal. With this, more complex SSEs, such as composite Thin Solid Electrolytes or interlayers are investigated. Its use demonstrates the impact of these developments on the morphology of Li and highlights the promises and pitfalls of cryo-PFIB for analysis of the Li-SSE interface. These results have contributed to three published papers [117, 165, 166].

3.2 Introduction

The Li-SSE interface is a key site for degradation mechanisms in ASSBs. These include dendrite growth, contact loss, and SEI growth.[99] The Li-SSE interface is buried making it difficult to characterise without generating artifacts. Additionally, the materials used in ASSBs are often air- and beam-sensitive, and composed of low-Z elements, restricting the applicable characterisation tools. For example they require specific hardware to avoid air contact and X-Rays from Li are only detectable in windowless EDX.[96]

FIB-SEM is a powerful technique which can be applied to this problem. It has been widely used to characterise the cathode-SSE interface in ASSBs.[191–195] It allows access to the internal structure of the battery with minimal artifact generation. Other methods of accessing these internal structures, for example snapping or crushing samples to image them internally, are liable to introduce high stresses, deformation, and fracture. While there are also artifacts which can be introduced by FIB, with proper utilisation they can usually be identified and avoided. Figure 3.1 demonstrates the ease of separating the components in the cross-section by using EDX with FIB-SEM imaging. This allows for easy component identification, analysis of phase distribution, and imaging of damage mechanisms throughout cycling or across different electrode morphologies. It has a higher resolution than techniques such as XRT ($\leq$ 1 nm compared to 10s - 100s nm) which can image these interfaces non-destructively. This makes them well-suited for combined use together to obtain information on the sample over different length-scales.[100, 166]

The application of FIB-SEM to the Li-SSE interface has been more limited as Li is highly beam-sensitive. The Meng group has more recently shown that cryo-FIB can be used to investigate Li while preserving the structure and minimising Ga implantation. [180] Keeping the sample cold reduces the impact of heating artifacts, such as melting, and reduces the effects of redeposition. It can also reduce the kinetics of any side-reactions induced by ion bombardment, including alloying and reactions with residual O in the chamber which could exacerbate heating effects by lowering the thermal conductivity.[189] The introduction of plasma FIB with Xe^+ can also reduce this effect, as Xe does not alloy with Li. Xe has also been shown to produce thinner damage layers than Ga (20 - 40 % less), even when utilising the higher currents available with an ICP source.[137, 152, 196]

Since this discovery, cryo-FIB has been used to investigate the morphology of Li at the Li-SSE interface. For example, Fuchs et al. used cryo-FIB with EBSD to characterise the orientation of deposited Li and Na with different current collector and SSE materials.[197] They also investigated the *operando* growth of Li dendrites using a W probe above a FIB-trench, which demonstrated whisker, film, and

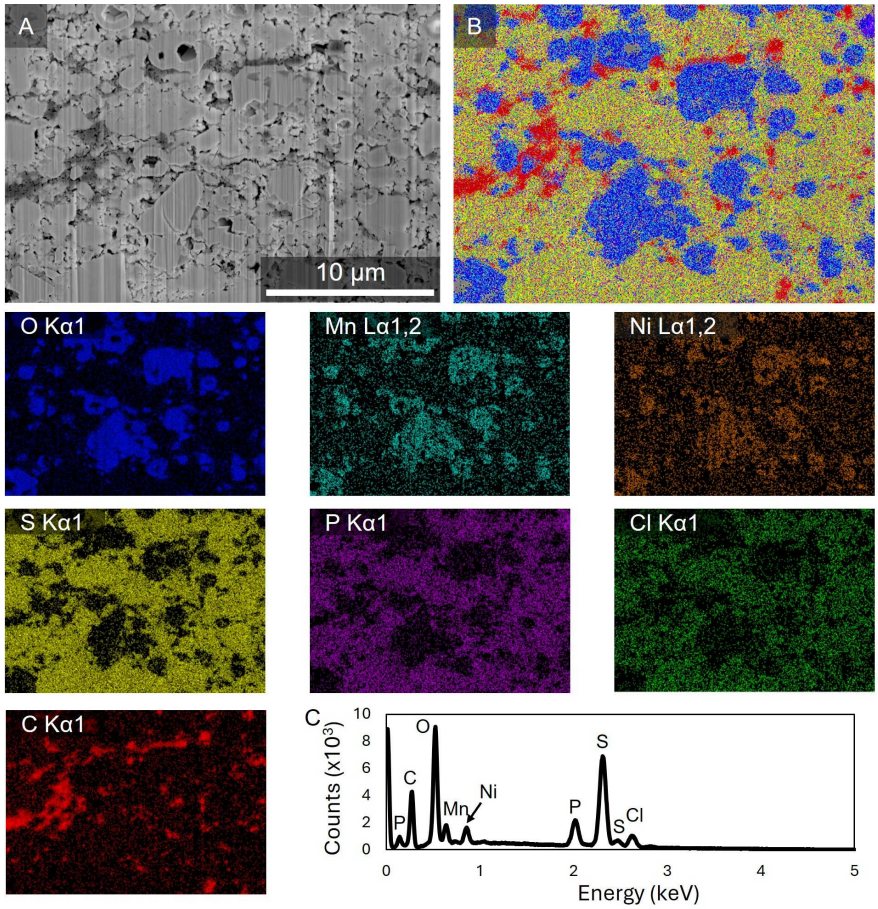


Figure 3.1: An example of plasma FIB-SEM cross-sectioning of a composite cathode containing hollow LNMO particles and LPSCl. (A) Shows the SEM image of the cross-section, where the Z contrast enables the C to be distinguished but it is harder to distinguish the cathode and electrolyte. (B) Shows an EDX map of all identified components in the sample, with the signals of C, S, and O being the strongest. (C) This is confirmed by the spectrum shown at the bottom of the figure. C shows the location of the C additive, S shows the location of the LPSCl, and O shows the location of the LNMO cathode. The individual maps for each component are shown below, and while the other elements show weaker signals the elements which should correspond to the same components are found in the same areas (shown in rows to aid viewing). Part of candidates contribution to [191] (reproduced with permission).

dendritic growth morphologies. However, this methodology is not representative of battery operation as no pressure is applied and the current is highly localised through the probe.[198] Other studies have also used FIB-SEM with EDX to demonstrate superior plating morphologies with current collector coatings such as LiPON and Li_2Te.[199, 200] Perhaps most promising is the use of FIB-SEM to better understand Li plating and stripping mechanisms. Wang et al. used

FIB-SEM with EDX to develop a model for the nucleation and growth of Li starting at grain boundaries and then spreading due to plastic deformation.[201] Void formation has also been investigated by imaging after stripping different capacities, demonstrating the evolution of the interface and that fewer but larger voids appear at lower current densities.[77]

For some SSEs, the SEI is visible in the SEM as a darker area at the SSE edge close to the Li. This has been demonstrated in LGPS, and also suggested with LPSCl.[202, 203] If this can be done, it would enable faster and easier imaging of the SEI thickness without the more difficult sample preparation required for TEM. This was the initial motivation for utilising the FIB-SEM in this thesis, but as will be shown it is not possible to view the SEI of LPSCl with this technique. Further technique development to enable imaging of this layer will be discussed in the next chapter. Nevertheless, FIB-SEM has enabled multiple investigations into the SSE-Li-based interfaces in ASSBs, which will be explored in this chapter, including imaging of alloys at room temperature to reduce reliance upon cryogenic stages for Li interface characterisation, better understanding of the pros and cons of the Li-Mg alloy system, how microstructure affects the popular Li-In reference electrode, the importance of microstructure to the development of TSEs, and the effect of temperature on Li plating morphology with an interlayer.

3.3 Results and Discussion

3.3.1 Li-Mg Alloy: Alternative to Li metal?

First, Li was confirmed to be heavily damaged with a Xe^+ ion beam at room temperature, as has been shown with Ga^+ FIB.[141] PFIB produces thinner damage layers, so it might have milled Li with fewer artifacts.[141, 196] As can be seen from the discolouration (due to reactions), gapping at the interface with Pt, and peaking morphology in Figure 3.2 (A), severe melting artifacts remain after milling Li (T_m = 180.5 °C) at room temperature in the PFIB. Gapping at interface has been observed with other low melting point materials.[204] These artifacts were mitigated by utilisation of a cryo-stage to cool the sample, as shown in Figure

3.2 (C), although cryogenic temperatures also meant that it was not possible to apply a Pt protective layer as the organic precursor would condense across the whole surface rather than be directed just to the location of the ion beam, as is the case during room temperature operation.

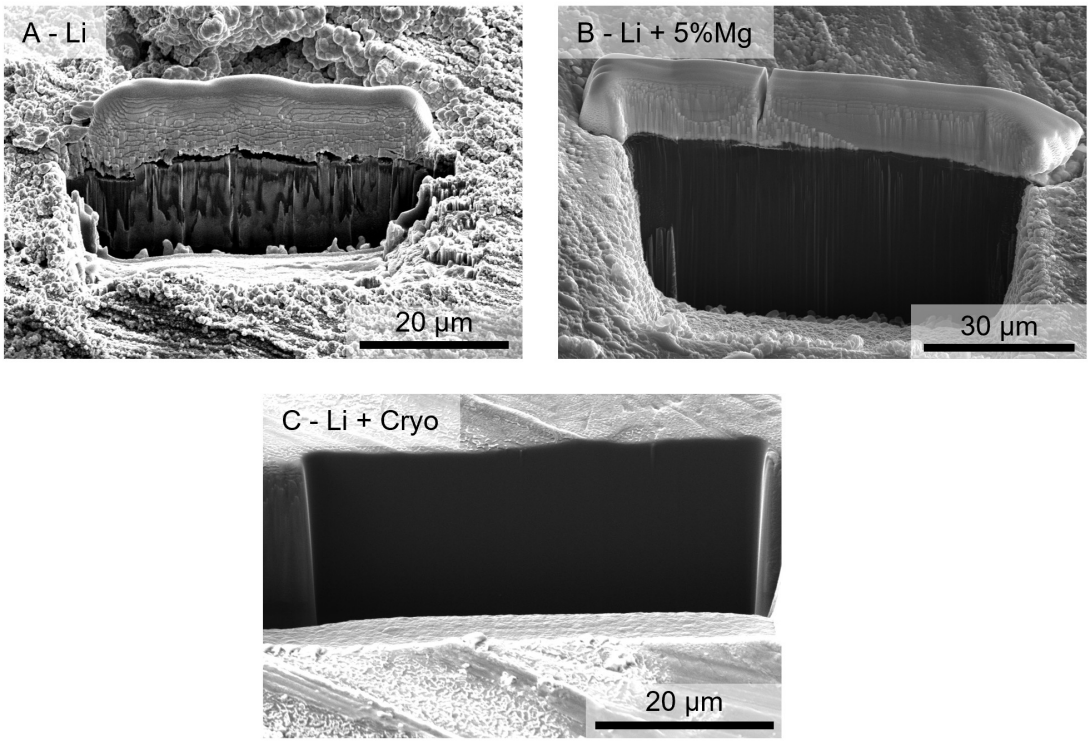


Figure 3.2: (A) Li milled with a plasma Xe^+ FIB at room temperature. (B) Li+5 at% Mg alloy milled at room temperature. (C) Li milled at -150 °C at a later date when a cryogenic stage was installed. All samples above had final polishing parameters of 30 kV 15 nA.

Cryogenic FIB stages are not widely available, and at the beginning of this work one was not available to me. Simultaneously, we were investigating whether Li-Mg alloys would make a good alternative to Li as negative electrode in ASSBs. Their higher melting temperatures (200 - 300 °C for 5 - 20 at% Mg) should reduce creep into the SSE pores and it was suggested they could leave behind a Mg scaffold on stripping to prevent voiding and encourage homogeneous plating.[85] The higher melting temperature and density suggested that they might also be more stable to FIB milling. This proved to be true after testing with various current densities as shown in Figure 3.2 (B). While very high current densities (> 60 nA) showed some

minor artifacts, such as gapping and discolouration due to reactions with trace O in the chamber, this was easily removed with cleaning mills at lower currents.

The other major source of deformation for Li at room temperature, as reported by Lee et al., was alloying due to Ga implantation.[141] Therefore, a cross-section of Li-10 at% Mg - SSE interface was prepared and EDX was run to identify if Xe had become implanted in either the SSE or the Li alloy. The EDX was run at 1.6 nA and 5 kV to minimise the interaction volume while ensuring signal from all expected elements. As can be seen in Figure 3.3, the S and Mg EDX signals are clearly separated along the Li-Mg - SSE (LPSCl) interface. A significant O signal can be seen at defects in the Li-Mg alloy and at the interface. This is expected due to small defects from the in-house manufacturing process and the reactivity of Li-Mg alloys, which leads to an oxide layer forming on their surface even when stored in an Ar glovebox (H_2O and $O_2 < 0.1$ ppm). Xe has two EDX peaks below 5 keV (Mα at 0.53 keV, Lα at 4.1 keV), which are indicated by green dashed lines Figure 3.3 (B). There is a peak at approximately 0.53 keV, but this can be attributed to O (Kα at 0.523 keV) as there is no noticeable peak at 4.1 keV. This shows that there is no noticeable implantation of Xe. Neither melting nor implantation cause significant artifact creation with Li-Mg alloys, enabling room-temperature FIB to be utilised for interface characterisation, which contributed to this study.[165]

Part of the attraction of Li-Mg for ASSBs is their similar potential to Li (E = 0.29x mV vs Li/Li^+, where x is the at% of Mg), which means they maintain a high energy density.[85, 165] This also means they should react with SSEs similarly to Li metal. From a characterisation perspective, this suggests they could be used to investigate the SEI. As can be seen in Figure 3.3 (A), the SEI is not visible in SEM, so it would need to be imaged with a higher resolution technique such as TEM.

FIB lamella were prepared from the Li-Mg alloys, with an example shown in Figure 3.4 (A-C). This further demonstrates their stability to FIB milling. These lamella were then transferred to the TEM via inert transfer. Unfortunately, even limiting the electron dose by using the small apertures (20 μm) and imaging at moderate resolutions (approximately 2.2x10^4 e^- $Å^{-2}$ s^{-1}), still lead to significant

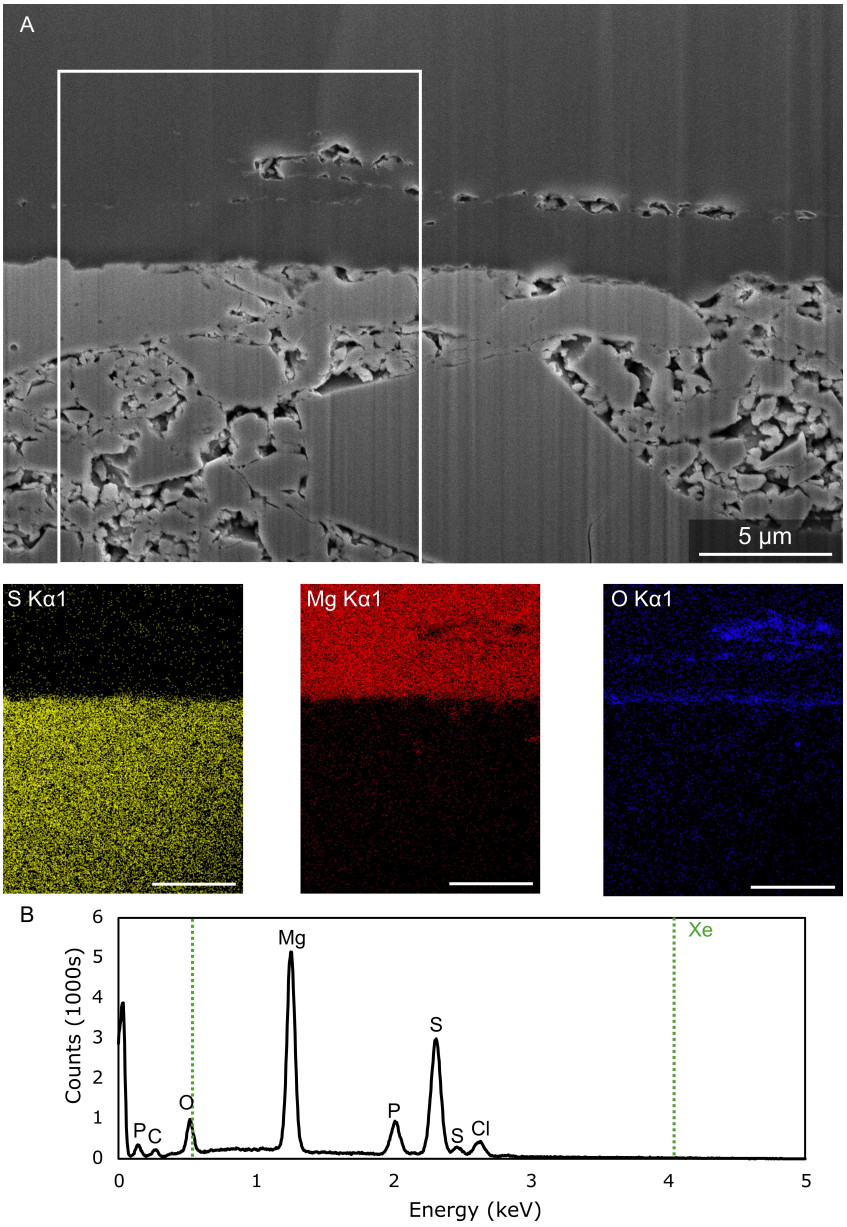


Figure 3.3: (A) Shows the SEM image of the cross-section of Li-10 at% Mg and LPSCl after polishing down to 30 kV 15 nA. The single-element EDX maps shown below correspond to the area surrounded by a white box in (A). They show a clear delineation between the Mg in the electrode and S in the SSE. The full EDX spectrum is shown in (B), with the location of Xe peaks shown as green dashed lines. All scale bars are 5 μm.

beam damage at room temperature (Figure 3.4 (D-E)). Smaller apertures and lower currents were also trialled, but there was insufficient signal to form a useful image. To obtain compositional information, sufficient resolution to view the lattice is required (so a FFT can be performed or the lattice spacing can be measured directly). Alternatively, EDX or EELS could be used but that would require much

higher electron doses. Therefore, higher resolution is needed than what can be achieved without damaging the alloys.

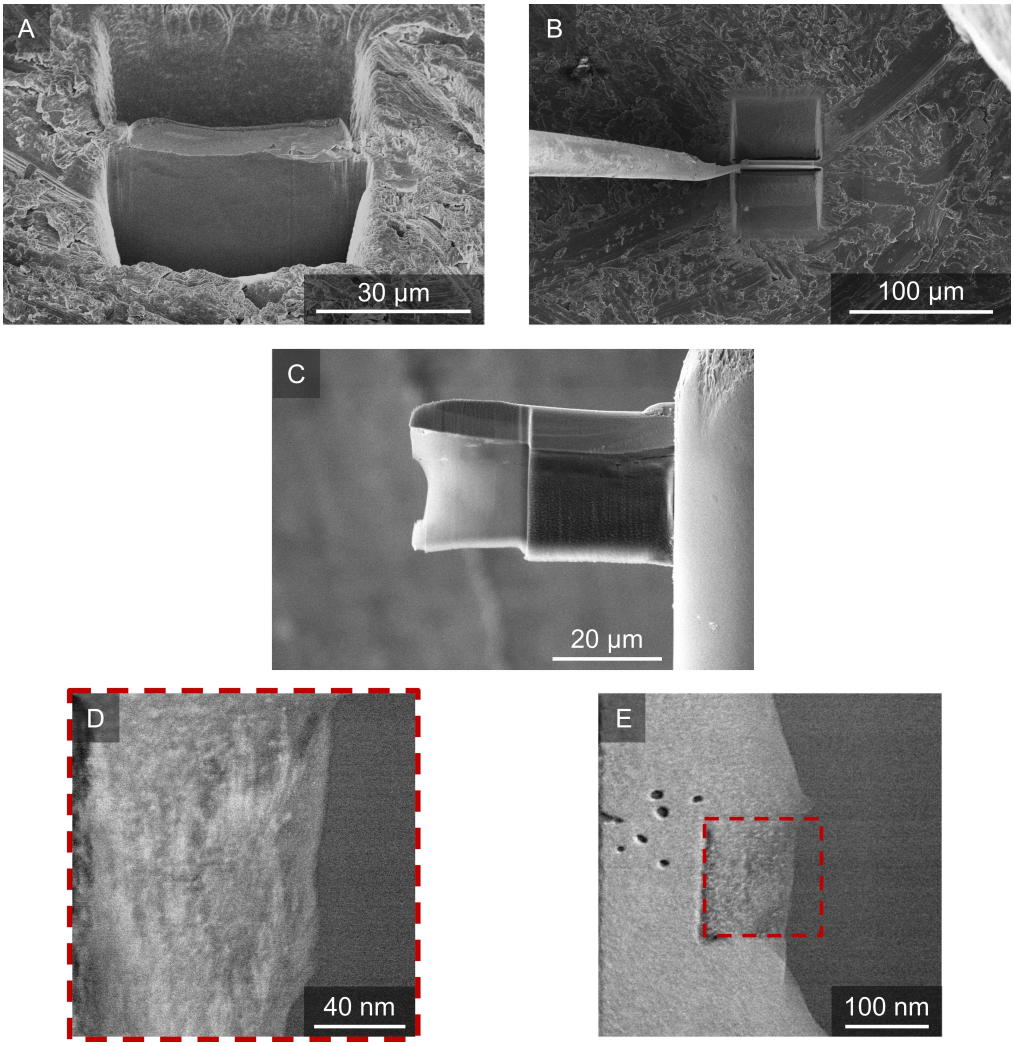


Figure 3.4: (A-C) Preparation of a TEM lamella with Li - 20 at% Mg. (D) Annular Dark Field (ADF) TEM image of a Li - 5 at% Mg lamella and (E) lower magnification image directly after showing the area of damage caused by the previous image. The respective area is shown with a red dashed box. TEM images taken with help from Ian Griffiths.

3.3.2 Li-Mg - Solid Electrolyte Interface

As Li-Mg can be milled at room temperature, we decided to investigate the evolution of the Li-Mg - SSE interface to evaluate the effect of its superior mechanical properties and determine if it could be used to avoid voiding and dendritic growth at the negative electrode. The mechanical properties of the Li-Mg alloys are shown

in Figure 3.5 (A-C).[165] The ratio of peak load (P_{load}) to load to overcome adhesion (P_{off}) clearly decreases with increasing Mg content. As higher adhesion decreases the likelihood of void formation, this is a strike against Li-Mg alloys, although it may make them easier to handle for manufacturing.[205] A linear increase in the indentation stiffness was observed with Mg content as has been observed in high-Mg alloys.[206, 207] This indicates increasing hardness across the compositions, which, along with the higher melting temperatures, reduces the creep rate. Creep can cause Li ingress into SSE pores, leading to short-circuits.[208] Finally, it has been suggested that alloys could be used as a scaffold for Li to encourage homogeneous plating and reduce the chance of dendritic growth.[85]

Initial electrochemical testing demonstrates that there are some pros and cons of using Li-Mg alloys, with significantly less capacity able to be accessed via chronopotiometry (Figure 3.5 D) and a sharper increase in potential than in the case of Li, as highlighted by the box. This suggests a sudden blockage of the path of Li^+ ions out of the alloy electrode, but does not provide information on the mechanism. Changes in the impedance of the cells over time were also investigated using EIS as as shown in Figure 3.5 E and F. While the high-frequency component, attributed to porosity and grain boundaries in the SSE, did not change much with composition, the much larger low-frequency charge transfer component became much more prominent with higher Mg content.[165] This is indicative of higher interfacial resistance due to passivation and/or reactive layers at the interface. The increase over time indicates that the reactive layers which form continue to grow over time. The key to understanding this electrochemical performance lies at the interfaces in the battery.

To evaluate the performance of Li-Mg alloys, interfacial characterisation is necessary. Initial experiments showed good interfacial contact between the Li - 5% Mg (Figure 3.5 (C)) while Li - 20% Mg had a significant gap at the interface, which would lead to cell failure (Figure 3.5 (D)). However, as with most ASSBs, these cells were cycled under externally applied pressure (5 MPa) which necessitated significant casing which needed to be removed prior to imaging. Removal of this

casing led to some unavoidable damage of the sample. Even while care was taken to mill trenches in central regions, far from areas with clear signs of damage, trenches often revealed disconnected current collectors, as shown in Figure 3.5 (E). While this has not induced cracking, because of the less adhesive nature of Li - 20% Mg, it could have peeled off during disassembly, rather than having occurred during cycling. In other samples and areas of the samples, better adhesion was found with the 20% alloy, and gaps were found between the 5% alloy and the SSE. In Figure 3.5 (F) you can see an enlarged section of the gap between the Li-Mg and SSE, which shows a close match between the morphology of the Li-Mg and the morphology of the SSE, suggesting close contact at a previous point. Therefore, while the FIB can be used to confirm that there is close contact between the Li-5% Mg alloy and the SSE, it cannot conclusively prove the presence of voids in disassembled cells.

To investigate the ability of Li-Mg to reduce the presence of voids and Li ingress, a cell was prepared where Li was first stripped then plated back into a Li-Mg alloy at 0.3 mA cm^{-2}. An example is shown in Figure 3.6 with a Li-10% Mg alloy. First, on the left side of the image in Figure 3.6 (A) there is an area of brighter contrast. It is shown at a higher magnification in (B), where it appears to be a void which has been partially re-filled with Li during plating. This is probably due to Li depositing most quickly at the corners of the void and growing into the space where there is less stress and therefore a lower energy barrier to deposition.[209] This shows that voids have formed at the interface and that it is preferential for the Li to deposit into the voids rather than into the Li-Mg alloy. That being said, if the voids refill on plating, that may help to maintain contact overall. The more concerning degradation mechanism is visible in the SSE.

Within the LPSCl SSE there is a region closer to the interface where the edges of the pores do not show any brightening due to edge effects. Further away from the interface, the edges appear brighter.[168] Further inspection of this area with EDX was done at 5 keV to minimise the interaction volume while still enabling visualisation of all expected elements. The S peak shows the location of the LPSCl,

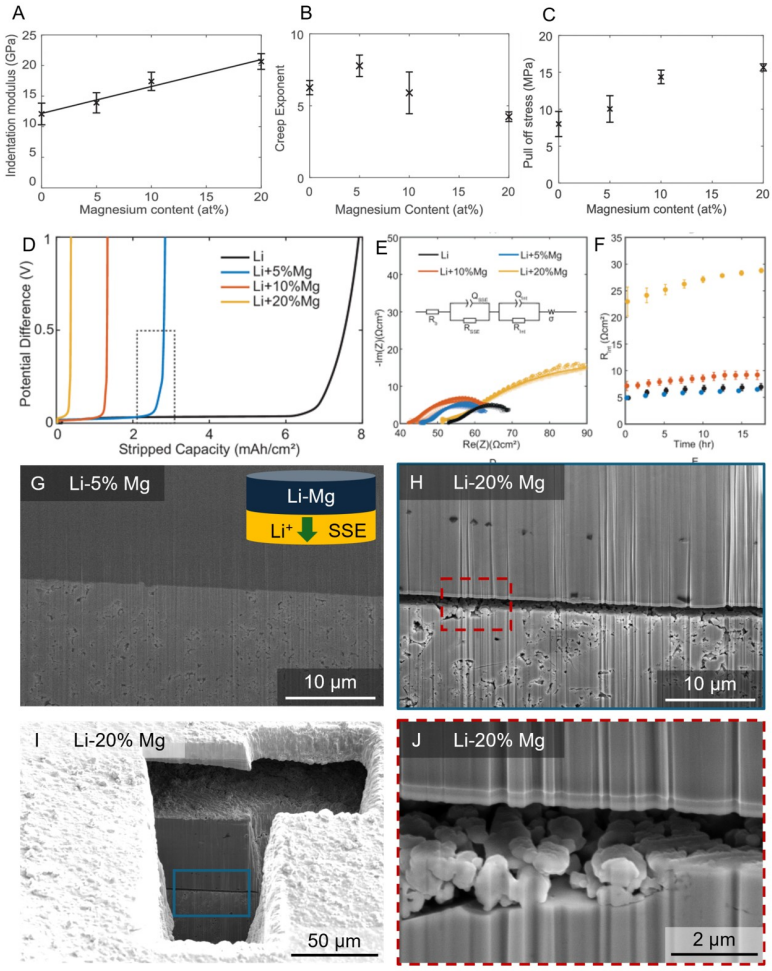


Figure 3.5: (A) Pull-off stress for different Li-Mg compositions where the error bars are the standard deviation. (B) Calculated creep exponent. (C) Indentation modulus for different Li-Mg compositions. (D) Chronopotiometric stripping (0.31 mA cm^{-2}) with potential as a function of capacity for the different Li-Mg compositions. (E) EIS measurements and fit for symmetric Li-Mg cells with the equivalent circuit used for fitting inset. (F) Change in interfacial resistance with time, derived as shown in (E). (G) Interface between Li-5 at% Mg and LPSCl after chronopotiometric stripping at 0.3 mA cm^{-2}. (H) Interface between Li-20 at% Mg and LPSCl after chronopotiometric stripping at 0.3 mA cm^{-2}. The dashed red box is shown blown up in (J) and a wider view of the interface is shown in (I) with the area shown in (H) indicated by a blue box. Analysis in A-C by Jack Aspinall, D-F by Krishnakanth Sada. Curtaining artifacts have been removed for clarity using FFT. A-H are reproduced with permission from [165].

but the characteristic X-Rays of Li iare too low-energy to be detected by a non-windowless EDX detector. As can be seen in Figure 3.6, the S signal is fairly homogenous below the line where there are bright edges start, while there are gaps corresponding to the pores above this line. This suggests that something is blocking

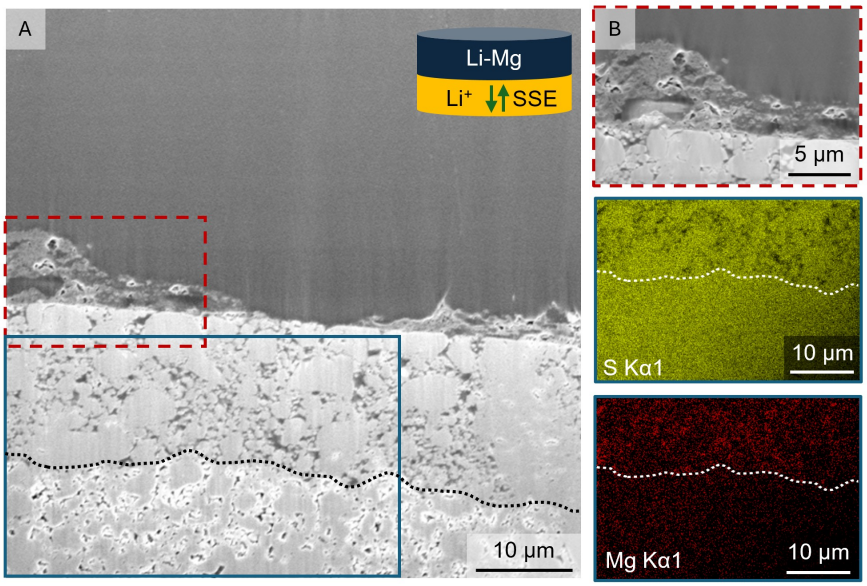


Figure 3.6: (A) SEM image of the interface between LPSCl and Li - 10% Mg after plating and stripping at 0.3 mA cm^{-2}. Inset shows a schematic demonstrating the plating and stripping. (B) Is a higher-magnification of the area in (A) surrounded by a red dashed box, showing a void refilled with Li. Below that are EDX maps taken at 5 keV for S and Mg corresponding to the area in (A) surrounded by a blue solid box. Images in the this figure have had curtaining artifacts removed with FFT for clarity.

the signal from these pores, or preventing the electrons from reaching the LPSCl in these areas. The dark contrast and the lack of obvious EDX signal shows this is Li. This negates another advantage of the Li-Mg alloy, as Li preferentially deposits in pores and not the alloy, showing that it does not function as a scaffold.

As outlined in the introduction there are still many questions about the mechanism behind dendritic growth in ASSBs.[100, 142] One of the main questions is whether Li begins to plate into the SSE through electron leakage, or whether it grows from the electrode and forms cracks. In this case, we can use the location of the Mg to determine if Li is connected to the electrode, as pure Li will be plated (Mg cannot be transported through the SSE) but Mg can diffuse through the Li to form a solid solution if it is in contact with the Li-Mg electrode.[153] Therefore, the fact that there is a Mg signal (as seen in the Mg EDX) coming from the region of the pores shows that they are connected to the Li-Mg electrode. However, this is a snapshot after plating. It is possible that earlier in the deposition process Li could

plate separately from the electrode, then become connected due to further growth, which has been described as spallation.[100, 153] Additionally, this SSE is highly porous, which gives many more opportunities for Li to deposit in low-stress areas.

3.3.3 Microstructural Changes in Li-In Alloys

Li-In alloys have been of interest as reference electrodes in ASSBs because of their wide two-phase region between In and Li-In, as can be seen in Figure 3.7 (A) and potential of 0.622 V vs Li/Li^+ which reduces the probability of dendritic growth.[210, 211] Usually they are simply prepared by placing a Li foil next to In metal, which undergoes a solid-state reaction to form the Li-In intermetallic. The slow kinetics, unstable voltage profile, and volume contraction (leading to loss of contact) make this an unsuitable method for producing a reference electrode.[166] A cast In - 25 at%Li electrode containing InLi islands within an In matrix produced a much more stable voltage profile as seen in Figure 3.7 (B), but only a very low discharge capacity. A second morphology utilised an In layer with a pressed InLi layer closer to the SSE, as can be seen in the schematic in (C). A much higher capacity was extracted, even at current densities over an order of magnitude higher. The reasons for this improvement in performance are revealed by PFIB-SEM.[166]

The success of milling Li-Mg alloys suggested that In-25% Li would also be able to milled at room temperature as it has a higher melting temperature (visible in the phase diagram in Figure 3.7 (A)) and higher Young's modulus and hardness.[166] However, the pure In phase is more difficult as its melting temperature is similar to Li (In: 156.6 °C, Li: 180.5 °C), and it has been shown to form defects on milling with both Ga and Xe.[154, 204] Those defects do not appear to be melting, despite its lower melting temperature and similar thermal conductivity to Li, where melting is observed as shown above (Li: 85 W $m^{-1}K^{-1}$, In: 86 W $m^{-1}K^{-1}$). Rather, gap formation between the In and higher melting point materials, and precipitation of pure In from alloys.[154, 204] Still, these observed morphological effects on milling are not as severe as what has been observed for Li. The reason behind this is may be due to the higher density of In compare to Li (In: 7.31 g cm^{-3}, Li: 0.534

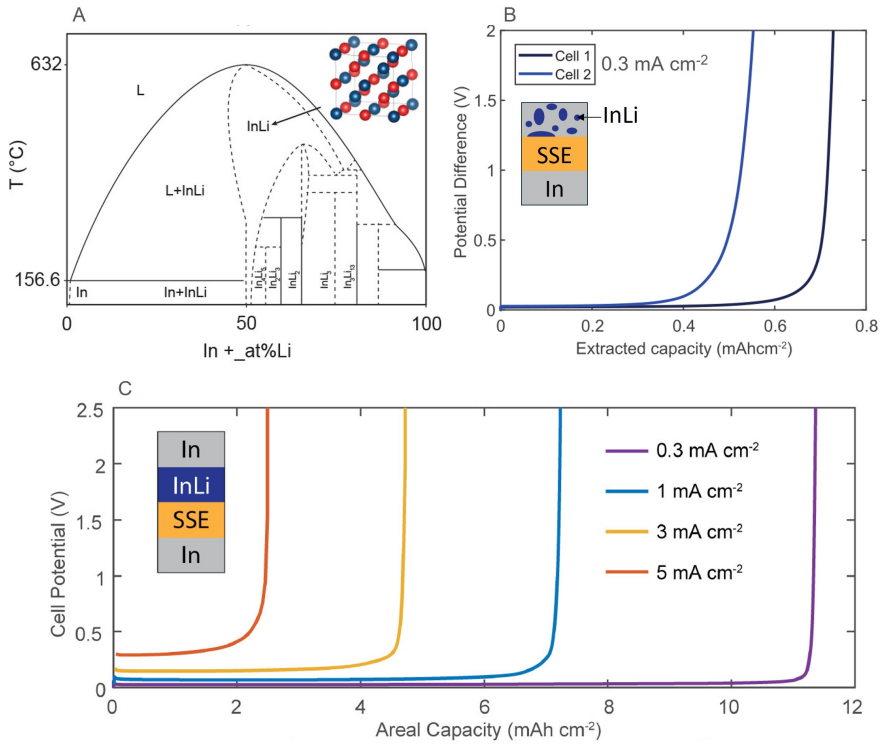


Figure 3.7: (A) Phase diagram of Li-In, redrawn from [210]. (B) Chronopotiometric discharge of two cast In-25%Li cells at 0.3 mA cm^{-2} with a schematic on the left side. (C) All reprinted with permission from [166], by Jack Aspinall.

g cm^{-3}) which reduces the projected range of incident ions, as can be seen in Figure 3.8. At the energy used for milling and polishing in these experiments, 30 keV, there is $>$ 7x larger projected range into Li than In. While there are significant assumptions when using SRIM for modelling ion ranges, notably that the samples are amorphous, this remains a significant margin of difference.[212] Additionally, milling through Li at room temperature was observed to cause arcing of the FIB gun, presumably because the light, sputtered Li was travelling up the column. As In is much heavier this was not a problem, allowing for milling at much higher currents than were allowable for Li.

Figure 3.9 (B) shows that it is in fact possible to mill an Li-In - In cast electrode without noticeable melting artifacts. The difference in Z between the two phases makes it clear where the two phases are, even in the SE images shown in (B) - (D). This is particularly beneficial as the lack of Li signal in EDX and the high proportion of In in the Li-In phase means that there is no visible differential in the EDX signal.

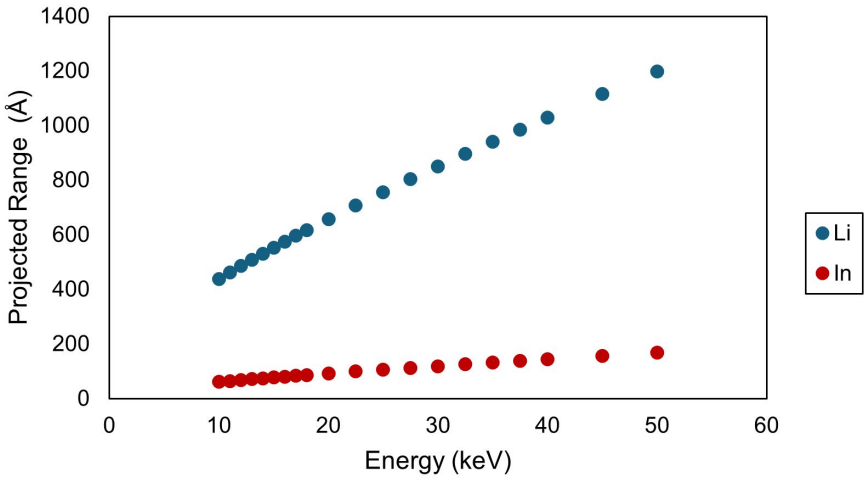


Figure 3.8: Graph of Projected Range for Xe^+ ions in Li and In calculated in SRIM.[212]

There is also a lack of variation in the O signal, which can sometimes be used to find the location of Li due to its high reactivity, even within the microscope vacuum it forms an oxide layer.[137] From the SE image, the darker phase is the Li-In phase (lower Z) and the brighter phase is pure In. The contrast would be greater in a BSE image, but the resolution would be slightly worse due to the larger interaction volume. Contrast can also be due to channelling of electrons into grains oriented so as to obey Bragg's Law. Electrons which are incident on grains where Bragg's law is obey can channel deeper into the material, leading to a much lower electron yield and dark areas in the resulting image. This could lead to similar contrast as observed here, even it was all the same material, and is known as channelling contrast. Tilting the sample so it is out of the Bragg condition would remove this effect, allowing users to differentiate between the Z and channelling contrast. As the Z contrast is more than sufficient in this case, SE images were used. There are cracks at the In - Li-In interface in a few locations. This could be due to material disappearance as has been observed with other In samples, Li-In shrinkage during stripping, or pulling apart during cell disassembly.[204]

Despite these difficulties, the mechanism behind the lack of capacity extraction is clear from the SEM images. The Li-In phase is only apparent further from the SSE. There is a strong difference between the conductivity of Li-In and In to Li^+ ions;

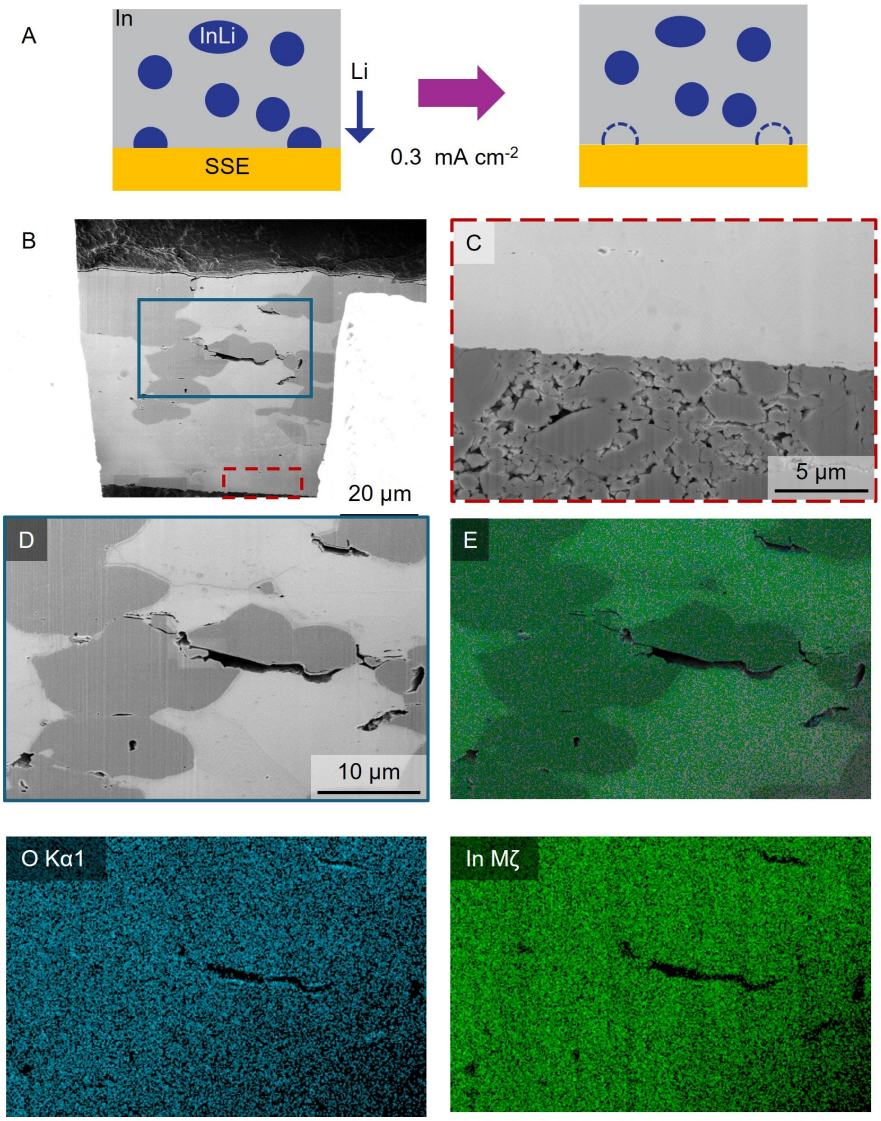


Figure 3.9: (A) Schematic of the delithiation of a cast In-25 at% Li alloy. (B) Full cross-section of the cast alloy after delithiation taken via SE imaging mode. (C) Higher magnification image of the interface between the Li-In alloy and the LPSCl SSE, corresponding to the red dashed box area in (B). (D) Higher magnification image of the Li-In case alloy further from the interface corresponding to the blue box shown in (B). (E) EDX map of the Li-In cast alloy area shown in (E) with both the O and In signal shown. O and In individual element EDX maps shown below. B,C are reprinted with permission from [166].

at 303 K the ionic conductivity of Li-In is 82.3 mS cm^{-1}, while it is negligible in In.[166] Therefore, the observation of an In layer between the Li-In alloy and the SSE interface suggests the mechanism shown in the schematic in Figure 3.9 (A). In this case, the fast Li conduction in the Li-In phase allows for high capacity extraction,

but Li-In phases which are not connected to the SSE are effectively isolated, so this capacity cannot be reached. This leads to the observed low capacities in Figure 3.7.

To reach higher extracted capacities and enable higher current densities on discharge, electrodes with a layer of In close to the current collector and Li-In pressed below were assembled. This enables good contact and voltage stability, due to the adhesive nature of the In, while the Li-In provides more extractable capacity.[213] The thickness of the electrode in the initial trial cell was approximately 250 μm, which made it difficult to obtain a cross-section without significant redeposition and shadowing from the trench, as can be seen in Figure 3.10 (B) and (C). Because of the high currents available with an ICP source, the full thickness was still milled through. The most time-consuming part was polishing at lower currents to obtain a cleaner cross-section. Final polishing was done at 30 kV and 0.2 μA, which is a much higher polishing current than normal, and with the area set back from the cross-section and FIB refocused so that the area of interest at the bottom of the cross-section, would receive optimal polishing.

From Figure 3.10 (B) and (C) it appears that the region further from the SSE is more rich in In, with a more Li-In rich phase closer to the interface. Around the Li-In particles there are bright rings of In. It is difficult to be conclusive about these observations because imaging at higher magnifications was restricted due to the deep cross-section leading to long distances between the interface and detectors, and reabsorption of electrons by the walls of the trench, lowering the electron yield. I requested a modified, thinner sample, which had an electrode approximately 100 μm thick, making it much easier to mill and polish in the plasma FIB, although this thickness would still be beyond what was reasonable to mill through for a LMIS Ga FIB. Images from this sample are shown in Figure 3.10 (D) and (E). The Li-In section looks similar to that in the first sample, as dark Li-In areas surrounded by bright In, which has presumably precipitated during delithiation. Cracks formed between the particles due to the 34% volume contraction of the Li-In during delithiation.[166] In either case, the low-conductivity In phase will gradually increase the tortuosity of the electrode, increasing the resistance to Li^+ conduction.

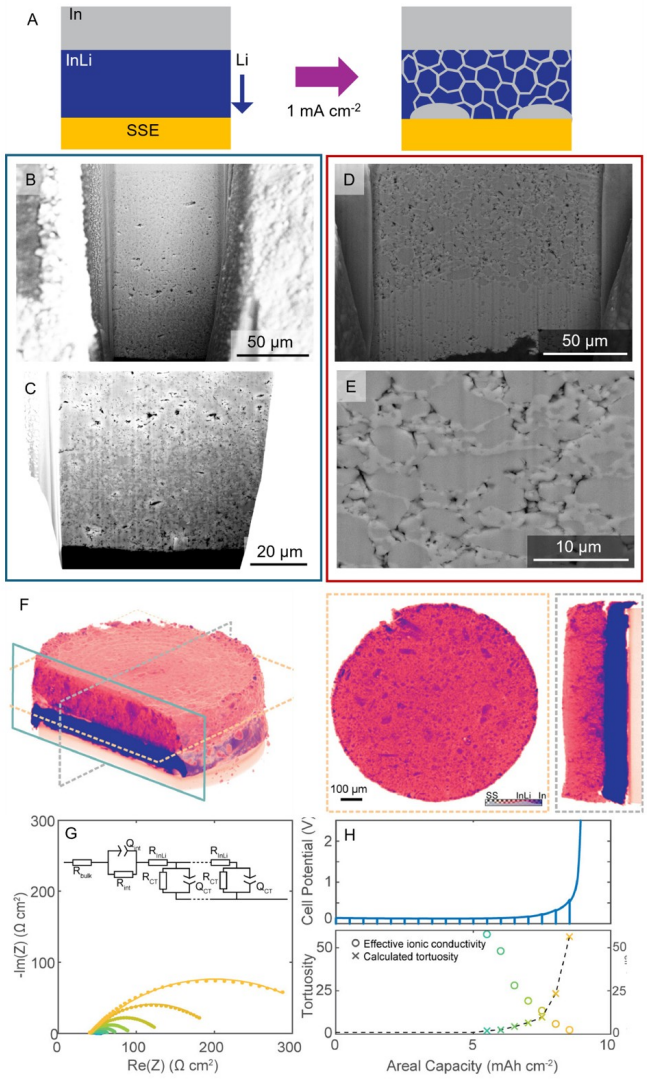


Figure 3.10: (A) Schematic of delithiation of layered In-25 at% Li alloy. (B) Cross-section of interface between a full Li-In electrode and SSE after chronopotiometric delithiation. (C) High magnification image of the interface. (D) Cross-section of thinner electrode, modified for characterisation. (E) Higher magnification image of the Li-In showing the precipitation of In around Li-In particles. (F) XRT of a Li-In electrode after delithiation, with the whole volume and two cross-sections. (G) EIS with delithiation, fitted with a transmission line model. (H) Chronopotentiometric trace with EIS locations marked (top) and calculated effective ionic conductivity and tortuosity (bottom). D-H are reprinted with permission from [166].

The major difference between the two samples is the presence of an In layer close to the interface with the SSE. As only a limited section of the interface is sectioned, there may be variations across the whole electrode that cannot be captured. The differences in the two samples suggests that a 3D reconstruction was needed to confirm the prevalence of large In volumes in the electrode. As

the Z difference is high between the In and Li-In phases, and the In area being investigated is on the order of 100s μm, this should be very possible for XRT, while the thickness of the electrode would make it overly time-consuming even with PFIB. XRT, completed by a collaborator, showed large distributed In precipitates throughout the electrode, as expected, but did not show clearly the In surrounding the Li-In particles. This demonstrates the benefits of using multiple characterisation techniques over different length scales for characterisation of battery materials. The combination of these techniques validates the mechanism shown in Figure 3.10 (A), where In chunks precipitate during delithiation, and thin layers of In precipitate around the Li-In particles.

Finally, the observed microstructure was correlated with electrochemical performance. EIS was run as Li was stripped from the Li-In chronopotiometrically. The impedance is split into electronic and ionic pathways through the whole electrode and the LiIn phase, respectively. This is represented by the transmission line model inset in Figure 3.10 (G). Initally, the impedance is dominated by the SSE-LiIn interface, and does not increase much. However, as more Li is extracted In begins to form, increasing the tortuosity of the cell and reducing the effective ionic conductivity, as shown in Figure 3.10 (H). The tortuosity calculations shown are derived from the EIS results and the known conductivity of the different phases [166] Eventually, the increase in tortuosity leads to such low effective conductivity that the cell fails. Without the cross-sectional analysis, correct interpretation of these electrochemical results, in particular fitting of the EIS data, would have been extremely difficult if not impossible.

3.3.4 Developing Thin Solid Electrolytes

For SSE to be applied commercially they must be thin enough to minimise their energy density and ionic resistance, while being able to be manufactured in a scalable manner.[94, 107, 214] This is a significant challenge for promising sulphide argyrodites because they are brittle and moisture-sensitive.[101] A promising method is to form a composite SSE by incorporating a polymer binder into the ceramic

SSE to improve the flexibility and allow it to be manufactured via scalable routes such as tape casting.[89] Based on this idea, we theorised a method for developing a TSE as shown schematically in Figure 3.11 (A), which incorporates a Carboxylated nitrile butadiene rubber (XNBR) binder into LPSCl to form a rubbery substance is formed into a thin film. This was promising, but required optimisation via a better understanding of the microstructure of the films.

Initially, optimisation of the densification pressure was done by cross-sectioning the TSE after densification at different pressures. The resulting microstructure was imaged in the FIB-SEM and analysed using ImageJ to obtain a porosity measurement.[215] As expected, the porosity decreased with increasing densification pressure, as can be seen in Figure 3.11 (B)-(I). Beyond a 200 MPa densification pressure the film became too brittle too handle, which placed an upper limit on the practical densification pressure which could be applied. As there were still significant improvements in the porosity when going from 100 MPa to 200 MPa, it was worth using this highest pressure. Lower porosity will help increase the ionic conductivity by reducing tortuosity through the electrode and should help prevent dendritic growth.[100] The characterisation of these TSE microstructures was quick and easy because of the high currents enabled by the ICP source. Three of the four samples were sectioned and imaged in one 8 h session.

In addition to the microstructure of the SSE, the location of the binder, XNBR, is important to know as it will have a significant impact on the electrochemical and mechanical properties of the TSE. These properties are summarised by the Young's modulus and ionic conductivity as shown in Figure 3.12 (A). The Young's Modulus was measured in compression and the ionic conductivity by EIS. From this characterisation, it is clear that the ionic conductivity of the TSE drops off quickly between 5 wt% and 10 wt%. Simultaneously the Young's Modulus does not drop significantly as it goes from 5 wt% to 10 wt%. Based on this, 5 wt% was chosen as the optimal binder content and used for the rest of the studies.[117]

All of these measurements were taken after the TSE had been densified at 200 MPa. The question of how the binder was impacting the properties of the TSE

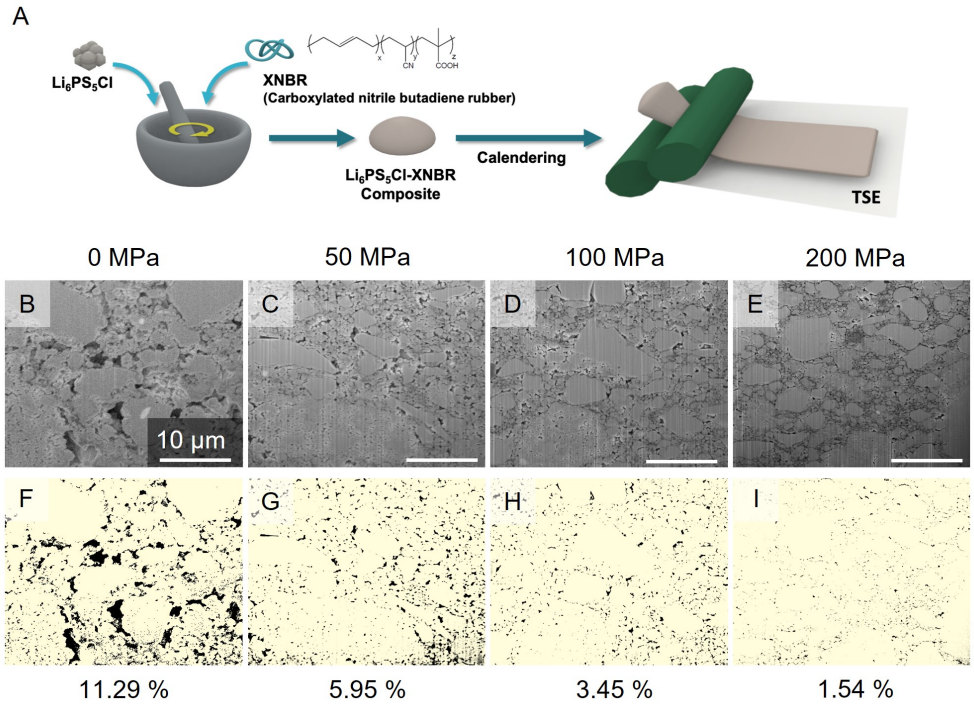


Figure 3.11: (A) Schematic of the preparation of a XNBR-LPSCl composite SSE. SEM images of SSEs with at (B) 0 MPa, (C) 50 MPa, (D) 100 MPa, and (E) 200 MPa, for 3 minutes, all scale bars 10 μm. Approximate porosity analysis using thresholding of the same areas as shown in SEM above, with the % porosity shown below. Samples made by Soochan Kim. (A) Was made by Soochan Kim and is reprinted with permission from [117].

during operation remained. Whether densification caused the much softer polymer binder to be squished out of the pores and end up at the edges and interfaces of the cell, blocking the ionic conductivity but not contributing to the mechanical properties. Ideally, the TSE would maintain its flexibility so that it could adjust to the large volume changes inherent in Li metal batteries.[97] To characterise this, it was helpful that a new cryogenic stage arrived as soft polymers have low melting temperatures (XNBR: 108 °C) and weak mechanical properties which would make them susceptible to ion beam damage.[216] This also enabled imaging of cells with Li.

An example of this can be seen in Figure 3.12. The EDX map in (B) shows the S, C, and O signals from the area after EDX has been collected at 5 keV. The S, C, and O signals are the brightest signals from the EDX as can be seen from the spectrum in (D). The S corresponds to the location of the LPSCl, the C to

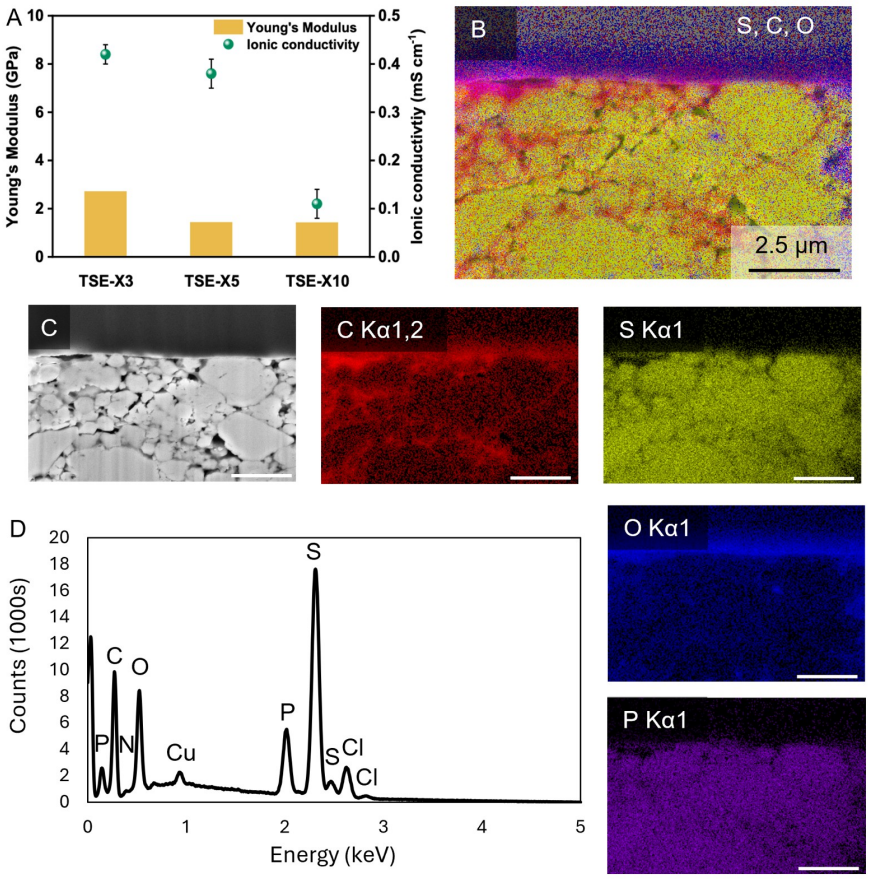


Figure 3.12: (A) Graph of changes in Young's Modulus and ionic conductivity for TSE. (B) EDX map of the S, C, and O EDX signals. (C) SEM image of the area shown in (B). (D) Full spectrum collected by EDX. EDX maps of the most significant elemental components are labelled with the element they represent. (A) is reproduced with permission from [117]

the location of the XNBR and to deposited material, and the O to the location of redeposited material and Li.[137] While there are other elements such as N which could be used to identify the location of the XNBR, seen in Figure 3.11, as can be seen in Figure 3.12 (D). Additionally, the difference in contrast in the SEM image shown in (C) is very minimal, and not sufficient on its own to determine the location of the binder, even when using high contrast. A slight difference in contrast can be observed in the areas with high C signal, but this would not be obvious without the C signal to draw the eye to these areas. As C is the strongest signal attributed to the binder, it must be used and while there is also O in the binder it is only 2 atoms per monomer compared to 10 C atoms, as they have similar Z

it could be expected that the C signal in the area where there is a binder should be higher than the O signal. This suggests that the areas which appear pink and purple in (B), which means there is a high overlap of O (blue) and C (red) are probably due to redeposition rather than the location of the binder.

With this observation, it appears that while the binder is not distributed between all the particles, it has also not been pushed all the way out of the TSE. This suggests that future work could improve the properties of the TSE further by optimising the binder distribution. If it completely surrounds the particles, it will inhibit ionic conductivity, leading to low rate capabilities. However, if it is too localised, the TSE will not benefit from the added flexibility. Stripes of binder perpendicular to the electrodes may form the best balance by providing conducting pathways supported by the binder throughout. Cryo-FIB-SEM would be a vital tool in characterising this development.

Understanding the degradation at the Li interface in Li batteries with a TSE is important to understanding why they fail and how they can be improved.[99] First, the electrochemical stability window (ESW) was investigated using Linear Sweep Voltammetry (LSV), as shown in Figure 3.13 (A). This demonstrates stability except for the expected degradation of LPSCl around 2.5 V to an insulating SEI including Li_2S, Li_3P, and LiCl. EIS was then used to determine the stability of the interface over time, with the impedance response attributed to a high-frequency 'bulk' and low-frequency 'interface' (also called charge-transfer), shown in Figure 3.13 (B). While there was a steady increase in the impedance, as would be expected from continuous SEI formation, it is comparable to what has been observed with pellets, if not better.[106]. The critical current density was then compared by increasing the current at regular intervals until the cells failed, showing comparable results between the pellet and TSE as seen in Figure 3.13 (C). This particularly noteworthy as Li dendrites have so much further to travel through the pellet to cause a short.

To investigate the stability of the interface between the Li and TSE during cycling a pristine cell interface was compared to an interface after the cell had been cycled for 500 h at 30 °C under < 1 MPa of pressure at 0.1 mA cm^{-2} with 0.05 mAh

cm^{-2} of capacity. The cell showed a stable voltage profile throughout cycling, as shown in Figure 3.13 (D). Figure 3.13 (E) shows the pristine interface. There is good contact between the Li and the TSE as it was milled under cryogenic conditions the Li shows no degradation due to milling. There is significant porosity in the TSE which is known to allow Li ingress as shown above with the Li-Mg alloys.[217] While difficult to discern just from contrast there also appears to be slightly darker areas between the different LPSCl particles which could be areas of binder.

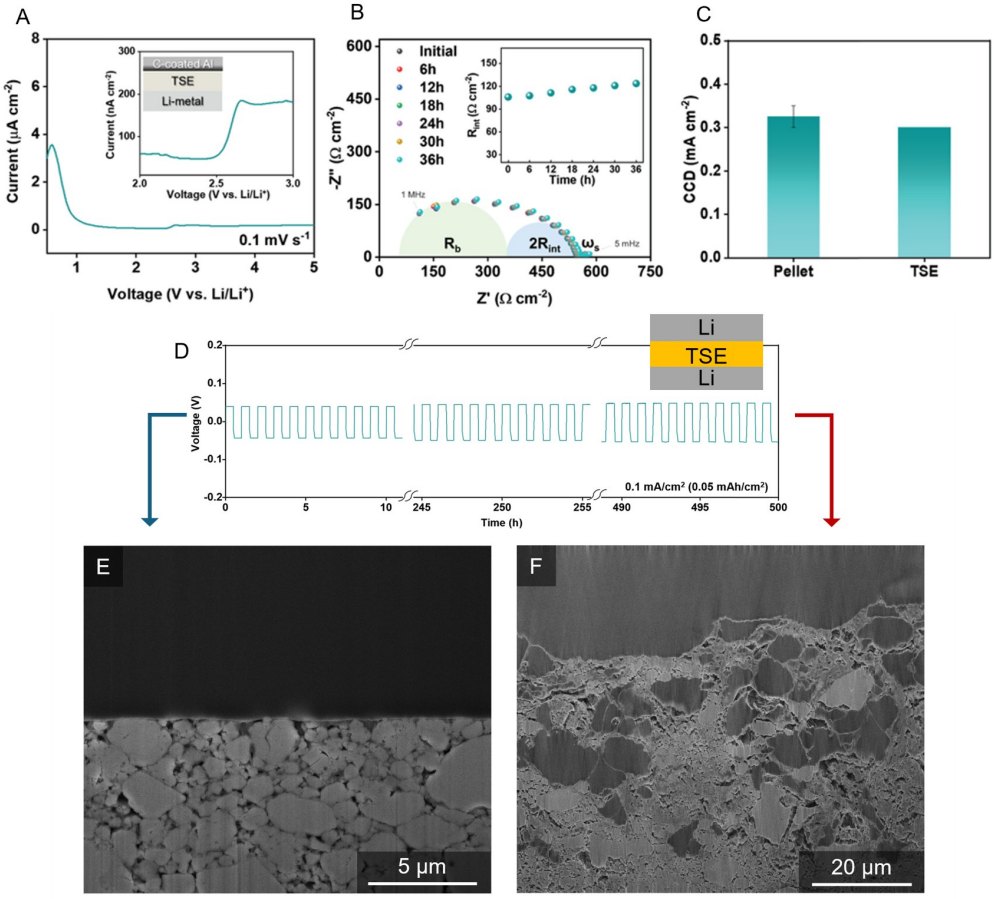


Figure 3.13: (A) Linear sweep voltammetry of half-cell from 0 to 5.0 V. (B) Nyquist plots of a symmetric cell Li-TSE-Li cell with the inset showing the change in interfacial resistance. (C) Comparison between the critical current density (CCD) of a pellet and TSE SSE. (D) Trace of cycling a symmetric Li-Li cell (shown in inset schematic) with a TSE composed of LPSCl and 5 wt% XNBR at 0.1 mA cm^{-2} (0.05 mAh cm^{-2} for 500 h. (E) Image of the Li-TSE interface of a cell before cycling. (F) Image of the Li-TSE interface of the cell that has been cycled for 500 h. Samples and electrochemistry by Soochan Kim. (A-D) are reprinted with permission from [117]. Curtaining artifacts removed for clarity with FFT.

The microstructure after cycling is significantly different to the majority of what has been reported. While it is not surprising to see Li ingress into the TSE, the morphology of the Li is interesting as most reports have demonstrated Li-filled cracks which have a higher aspect ratio.[100, 217] The rounded morphology is probably due to a combination of factors including the presence of the binder, which will help reduce likelihood of brittle fracture as it could deform plastically and rebound on delithiation. The low capacity being cycled could also be a factor as it could lead to growth of small areas of Li over multiple cycles into round morphologies. It could also be due to the high degree of porosity in the TSE, leading to a weaker mechanical structure which is more easily pressed outwards in all directions rather than along a crack perpendicular to the electrode.

By applying cryo-FIB-SEM to the Li-SSE interface, insights can be reached about changes in the morphology of the interface due to degradation and the morphology of the SSE, including the binder location. Using cryo-FIB helps maintain the integrity of these interfaces. Future work could analyse the degradation at more points throughout the degradation process and with 3D-FIB-SEM and EDX to map the changes in the binder location along with Li protrusions.

3.3.5 Effect of Interlayers and Temperature on Li morphology

As has been discussed, FIB studies have lead to significant understandings of the interfaces in ASSBs. The application of this technique to interfaces including Li metal is still in development, and there are some areas where interpretation remains unclear. This section will discuss some considerations that should be taken into account when conducting FIB and cryo-FIB studies, within the context of some recent promising reports on ASSBs. One of the most exciting areas for development in ASSBs is interlayers. They attracted attention based on the very promising paper published by a research group at Samsung.[218] This paper showed remarkably stable cycling of a Li metal full cell with a Ag-C interlayer apparently the main cause of the improvement in performance. The exact mechanism behind

this improvement was not well understood and it prompted many researchers to investigate how the interlayer functioned, and whether other materials would be able to undergo a similar mechanism.[219–222] However, the elevated temperature used during the investigation may have swayed the results significantly as the cells were cycled at 60 °C.

Figure 3.14 shows cells prepared in a similar way to the Samsung paper, but cycled at 60 and 30 °C.[218] In the case at 60 °C a very smooth deposition morphology is observed, while at 30 °C the deposition morphology is smooth in some areas and rough in others. It is also noteworthy that the deposition thickness in the 60 °C case is much greater. The higher temperature means that the Li more easily undergoes plastic deformation, filling in any areas to reduce stress. This process would still occur at 30 °C, but more slowly. From what is visible here, the temperature has a very significant impact on the deposition morphology of the Li in ASSBs, suggesting that the effect of the interlayer may not be as significant as initially thought.

That being said, even at 30 °C, the deposited Li is homogeneous and dense in some areas and the interlayer in both cases shows slight movement of the bright Ag particles in the interlayer closer to the Li layer. EDX was also used to investigate the dispersion of Ag particles, but the large interaction volume made BSE images easier to interpret. This suggests that the interlayer is having some effect, or at least that the Ag particles are interacting with the deposited Li in some way. Based on subsequent studies it has been shown that the Li intercalates into graphite and alloys with Ag in the interlayer during deposition.[219] Therefore, the interlayer helps with deposition, but so does a higher temperature.

All the images in Figure 3.14 are taken in BSE mode. This was useful for this sample because the high Z differential between Ag and C made this a very clear imaging mode for the interlayer. There was another reason, as illustrated in Figure 3.15. Using BSE mode reduces the interference of charging artifacts because it only accepts high-energy electrons, therefore the image looks quite clear in (A). The image in (B) is taken in SE mode and shows a plethora of charging artifacts. This was the case even when the scan rate was increased and the ion beam was used to

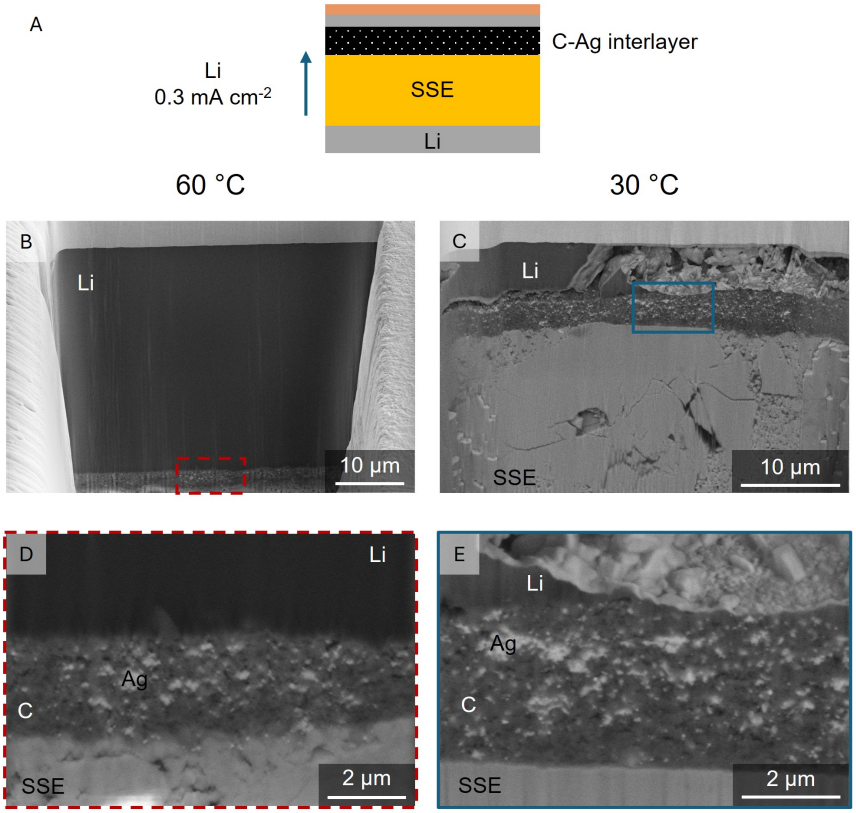


Figure 3.14: (A) Schematic of the testing cell. (B) Li plated at 60 °C through a Ag-C interlayer, with the interface at the bottom of the image. (D) is a higher magnification view of the interlayer shown in (B). (C) Shows Li plated through a Ag-C interlayer at 30 °C. (E) is a higher magnification view of the interlayer shown in (C). All images are in BSE mode. FFT was used to remove curtaining marks for clarity.

neutralise the charge on the surface. This is of note because it is only the case when imaging is done at cryogenic temperatures, the images taken above, of very similar materials, did not have this issue when taken at room temperature. There has been a report suggesting that the dark areas surrounding cracks were due to the formation of the SEI in LPSCl.[203] There appear to be areas identical to this around the cracks in the SSE in (B). However, there is no variation in the BSE image in (A), suggesting that there is no Z differential. Additionally, in the BSE image the back of the voids can be observed, showing that they are not filled with Li, so it would not make sense for an SEI layer to have formed. Therefore, other higher magnification methods are needed to investigate degradation at the interface due to SEI formation.

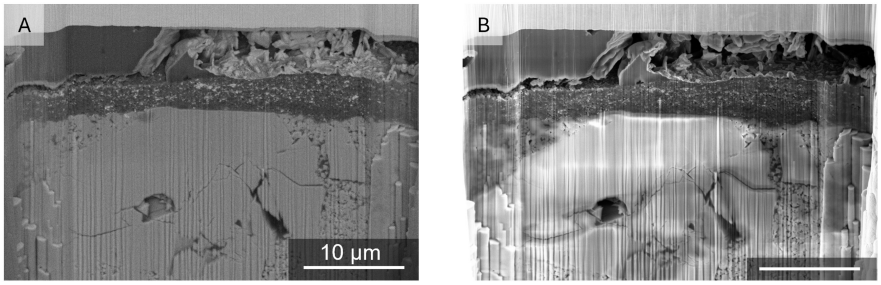


Figure 3.15: The same area of the 30 °C interlayer sample imaged in (A)BSE and (B)SE mode.

3.4 Conclusion

Understanding degradation phenomena at battery interfaces is key to unlocking performance improvements. However, in solid-state batteries revealing these interfaces without introducing artefacts is non-trivial. Here, the the interface between Li-based electrodes and LPSCl-based SSE were investigated using plasma FIB-SEM. Li-Mg alloys were shown to be a good Li proxy for FIB characterisation, but not sufficiently stable for TEM studies. The ability of Li-Mg alloys to combat common interfacial degradation mechanisms was then investigated, and unfortunately found to be ineffective. As Li-alloys were shown to be stable to ion milling, the microstructural evolution of Li-In alloys during discharge was evaluated to understand the benefits of a layered morphology, enhancing understanding of this commonly-used reference electrode. Then, the speed of plasma FIB was utilised to characterise the morphology of a TSE and evaluate its degradation at end of life with cryo-FIB. Finally, the effect of temperature on deposition with a Ag-C interlayer was shown to be highly significant. Throughout, the abilities and difficulties of PFIB-SEM analysis were discussed within the context of ASSB characterisation to improve our understanding of how this technique can reveal insights into ASSB interfaces.

3.5 Experimental Detail

3.5.1 Plasma Focused Ion Beam - Scanning Electron Microscopy

All samples were stored in an Ar glovebox with H_2O and $O_2 < 0.1$ ppm prior to imaging. They were transferred to the FIB using a Gatan iLoad airless transfer vessel. A Helios G4 PFIB CXe DualBeam (Thermo Scientific) was used for all all cross-sectioning and imaging work. All milling was done at 30 kV, except for final thinning of the TEM lamella, which was done at 5 kV. Standard milling procedure with use with regular cross sectioning starting at 0.2 μA in all cases except the Li-In case, where 0.5 μA was used initially due to time constraints. The regular cross-section pattern scans across the designated, moving line-by-line closer to the edge. Lines are repeated as necessary to reach the desired depth which is calibrated to Si (LPSCl at room temperature and Li at cryo both mill at approximately 2x the rate of Si). A cleaning cross section involves a similar mechanism but in as single pass and was used after the initial rough section at lower current densities. This cross-section pattern keeps the beam close to the interface to reduce redeposition. Final polishing currents are specified in the above text, if not specified they are 15 nA, again with the exception of the TEM lamella which was 1 nA. Unless specified in the text, all images were taken in SE mode at 5 kV 0.1 nA.

Samples milled at cryogenic temperatures were milled at -150 °C using a Gatan cryo stage. Images were taken at room temperature unless specified otherwise. A thermocouple attached to the stage was used to confirm the stage temperature and the stage was held at -150 °C for 15 minutes prior to milling to ensure that the sample itself had reached this temperature. An anti-contaminator held at a lower temperature to prevent condensation on the sample surface was placed above the sample, somewhat limiting stage mobility. Once the stage had reached cryogenic temperatures it was not able to be moved more than very small amounts due to the potential to damage the stage or wires.

3.5.2 Energy Dispersive X-Ray Spectroscopy

EDX was acquired in the same microscope with an Oxford Instruments Ultim Max 170 X-ray detector with an accelerating voltage of 5 kV, except in the case of the Li-In sample where 10 kV was used, and an operating current of 0.8 nA.

3.5.3 Transmission Electron Microscopy

Samples were transferred from the glovebox to the TEM in a JEOL anaerobic transfer holder, after being loaded in the glovebox. TEM was carried out in an aberration-corrected JEOL ARM200F microscope operated at 200 kV. Dose information is based on calibration done in January 2020, which is the most recent available, using a 20 μm aperture and 10C spot size.

3.5.4 Sample Preparation

Li-Mg Alloys

Li (99.9%, Alfa Aesar) and Mg (99.98%, Alfa Aesar) were heated to 450 °C in an Ar-filled glovebox (H_2O and $O_2 < 0.1$ ppm) in a box furnace (MTI KSL-1200X-J-UL) and slow-cooled in the furnace to room temperature.

Electrochemical measurements were done in an environmental chamber at 30 °C. 100 mg of LPSCl (Ampcera 10 μm) pellets were pressed within custom Macor ceramic cells (diameter 10 mm) with stainless steel plungers, then densified at 370 MPa for 300 s. Alloys were calendared to 50 - 150 μm thick then attached to the LPSCl at 80 MPa. A constant pressure of 5 MPa was applied while during testing. Symmetric cells were tested for chronopotentiometric stripping and were rested for 18 h before testing to ensure stability.

These samples were prepared by Jack Aspinall.

Li-In alloys

The cast sample was prepared by combining In (Alfa Aesar 99.99%) and Li (Alfa Aesar 99.9%) in a 75:25 wt% ratio then heated to 700 °C in an Ar-filled glovebox (H_2O and $O_2 < 0.1$ ppm) in a box furnace (MTI KSL-1200X-J-UL) and slow-cooled

in the furnace to room temperature. The alloy was cleaned and calendared to approximately 200 μm and attached to a LPSCl pellet at 80 MPa.

The layered structure was prepared by forming a Li-In alloy with a 50:50 wt% ratio, grinding with a mortar and pestle, then ball milling (Fritsch Pulverisette 7) all within an Ar glovebox. In foil of 120 (Alfa Aesar) or 20 (Kisco) μm was punched to 10 mm diameter. 70 mg of ball-milled Li-In was added to the densified LPSCl pellet and densified at 370 MPa for 300 s.

Electrochemical measurements were done in an environmental chamber at 30 °C. 100 mg of LPSCl (Ampcera 10 μm) pellets were pressed within custom Macor ceramic cells (diameter 10 mm) with stainless steel plungers, then densified at 370 MPa for 300 s. A constant pressure of 5 MPa was applied during chronopotiometric stripping at the current densities specified in the text above.

XRT: A custom cell was designed for 3-D XRT. The body of the cell was Polyether ether ketone (PEEK) with stainless steel pistons. The inner cell diameter was 1 mm to enable μm level resolution using a Zeiss Xradia 610 Versa desktop XRT. 1 mg of LPSCl was pressed at 330 MPa followed by 0.7 mg of Li-In at the same pressure. In foils were cut with a biopsy punch and added afterwards. A constant pressure of 5 MPa was used during discharge at 30 °C. XRT was conducted at 130 kV, power of 19.5 W, exposure time of 17.5 s, voxel size of 1 μm, 4x objetive lens and Xradia filter (HE5). 3201 equally-spaced projections were acquired through 360 ° of rotation. Projections were reconstructed using Scout-and-Scan(TM) Reconstructor software (Zeiss) with a beam hardening correction of 0.5 used for beam hardening artifacts of highly attenuating materials. Visualisation and analysis was conducted in Fiji and Avizo Software.

Samples were prepared by Jack Aspinall. XRT was conducted by Pranay Shrestha.

Thin Solid Electrolytes

LPSCl (99.9 %, Ampcera, 1 μm) and XNBR (99.8 %, Sigma Aldrich) were combined in a mortar and pestle. The composite was then placed between Si-

coated polyethylene terephthalate films (PET, thickness 50 µm) and calendared (MTI corp., MSK-2150) to form thin films of desired thickness. Films were left to dry overnight then pressed for 3 minutes at the 0, 50, 100, or 200 MPa. All processes were carried out in an Ar-filled glovebox (H_2O and $O_2 < 0.1$ ppm, MBraun).

For symmetric Li-Li cycling, two 100 µm thick Li-metal anodes (Sigma Aldrich) with a diameter were cleaned and calendared before attaching to either side of the TSE. 5 MPa of pressure was applied to the configuration for 1 min to ensure good contact. They were cycled at <1 MPa (in a coin cell) at 30 °C in a environmentally controlled chamber. Specific cycling conditions are given in the main text.

Samples prepared by Soochan Kim.

Interlayer

100 mg of LPSCl (99.9 %, Ampcera, 10 μm) was pressed at 200 MPa 1s, then the Ag-C interlayer was added and pressed together at 400 MPa for 1 minute. The Ag - C interlayer was prepared by mixing Polyvinylidene fluoride (PVdF), Ag (approximately 10 nm), and carbon black in a 21.5:64.5:14 weight ratio. Li (Sigma Alrich, 99.9%) was cleaned and calendared before attachment to the other side of the LPSCl pellet. An excess of Li was used. All processes were carried out in an Ar-filled glovebox (H_2O and $O_2 < 0.1$ ppm, MBraun).

Cycling occurred in an environmental chamber held at either 30 or 60 °C as specified in the text. 6.2 mAh cm^{-2} of capacity was plated at a current density of 0.31 mA cm^{-2} under a constant pressure of 5 MPa.

Samples prepared by Yoshifumi Mizuno.

All sorts of things can happen when you're open to new ideas and playing around with things.

— Stephanie Kwolek, Chemist who invented Kevlar

4

Technique Development for Nano-structural Analysis of the Li-Solid Electrolyte Interphase in Solid State Batteries

Contents

4.1 Abstract 94
4.2 Introduction 94
4.3 Results and Discussion 95
4.3.1 Sample Extraction 95
4.3.2 Sample Thinning 100
4.3.3 Microscope Workflow 103
4.3.4 4D-STEM Validation 104
4.4 Conclusion 108
4.5 Experimental Detail 109
4.5.1 Materials 109
4.5.2 Cell Preparation 109
4.5.3 Electrochemistry 110
4.5.4 Focused-Ion Beam Thinning 110
4.5.5 4D-STEM 110

4.1 Abstract

ASSBs have attracted interest due to their potential safety and high energy density due to compatibility with Li metal anodes. However, most commercially promising solid state electrolytes (SSEs) react with Li metal. The structure of this solid electrolyte interphase (SEI) has not been well investigated due to its inherent beam- and air- sensitivity which makes it difficult to characterise. Here, we develop a novel sample-preparation workflow to isolate the Li-SEI-SE interface by incorporating a TEM grid into a SSB, thinning with a Xe^+ focused ion beam and imaging using low-dose 4D-scanning transmission electron microscopy at room temperature. All processes occur without air exposure and with minimal artifact generation. This enables component identification and, for the first time, mapping of the SEI which forms between Li_6PS_5Cl and Li metal.

4.2 Introduction

Li reacts with most SSEs, leading to a SEI which can increase resistance and exacerbate other degradation mechanisms such as dendritic growth.[99, 106, 135] This means, as with liquid electrolytes, the SEI is an important factor in the performance of ASSBs. Characterising the SEI with a SSE includes additional challenges to liquids. In both cases, the SEI is highly air- and beam- sensitive. Cryo-microscopy has enabled imaging of the SEI in liquid electrolytes, with the majority of samples prepared by washing a TEM grid which has Li electrochemically plated onto it.[56, 223] This is not possible with solid electrolytes, so alternative sample preparation workflows must be developed.

Using cryo-FIB and cryo-TEM, the Meng group revealed a layered SEI structure with LiPON. They observed Li_2O forming next to the Li, then Li_3N and Li_3PO_4 towards the LiPON.[157] The overall structure was that of crystallites within an amorphous matrix, as has been observed with liquid electrolytes.[44] LiPON can be formed into thin, dense layers which are sufficiently mechanically stable and thin to be able to quickly and easily produce FIB lamella. Zhang et al. used

cryo-ultramicrotomy with cryo-TEM to investigate the Li-PEO interface, revealing a SEI composed of Li_2O, Li_2CO_3, LiH, and LiOH with EELS.[224] The ductility and high fracture toughness of polymer SSEs like PEO allows techniques such as cryo-ultramicrotomy to be utilised.

While these studies have pioneered investigations into the SEI in ASSBs, PEO and LiPON are too ionically resistive for most commercial applications.[97] Sulphide argyrodites, which can achieve the necessary ionic conductivities, have only been investigated in one study as their brittle nature and greater difficulty in forming a dense structure makes the techniques used above without generating artifacts more challenging. Luo et al. mechanically detached dendrites from a LPSCl SSE to investigate the SEI with cryo-TEM without difficult sample preparation procedures.[154] While this was the first time the SEI was imaged in the TEM with this promising SSE, the sample preparation method may have affected the observations as the full SSE-SEI-Li cross-section was not preserved.

Here, I present a workflow to prepare samples and image the SEI formed between Li and LPSCl. This workflow preserves the SSE-SEI-Li cross-section and enables room-temperature imaging, while minimising the introduction of artifacts. It does so by incorporating a TEM grid into an ASSB to electrodeposit Li, then cryo-FIB thinning of relevant areas on a removal, and finally low-dose 4D-STEM imaging of the interface, all without air exposure. A schematic of the workflow can be seen in Figure 4.1.

4.3 Results and Discussion

4.3.1 Sample Extraction

The first step in sample preparation is removal of the Area of interest (AOI) without artifact generation. A standard FIB liftout could not be used because high milling currents with Li metal caused arcing of the FIB source. Using lower currents would be time-preventative. To get around this issue, the cell was made smaller so that milling time would be minimised, especially through the highly-sensitive Li. Some examples are shown in Figure 4.2. A standard lab-prepared ASS cell utilises 100

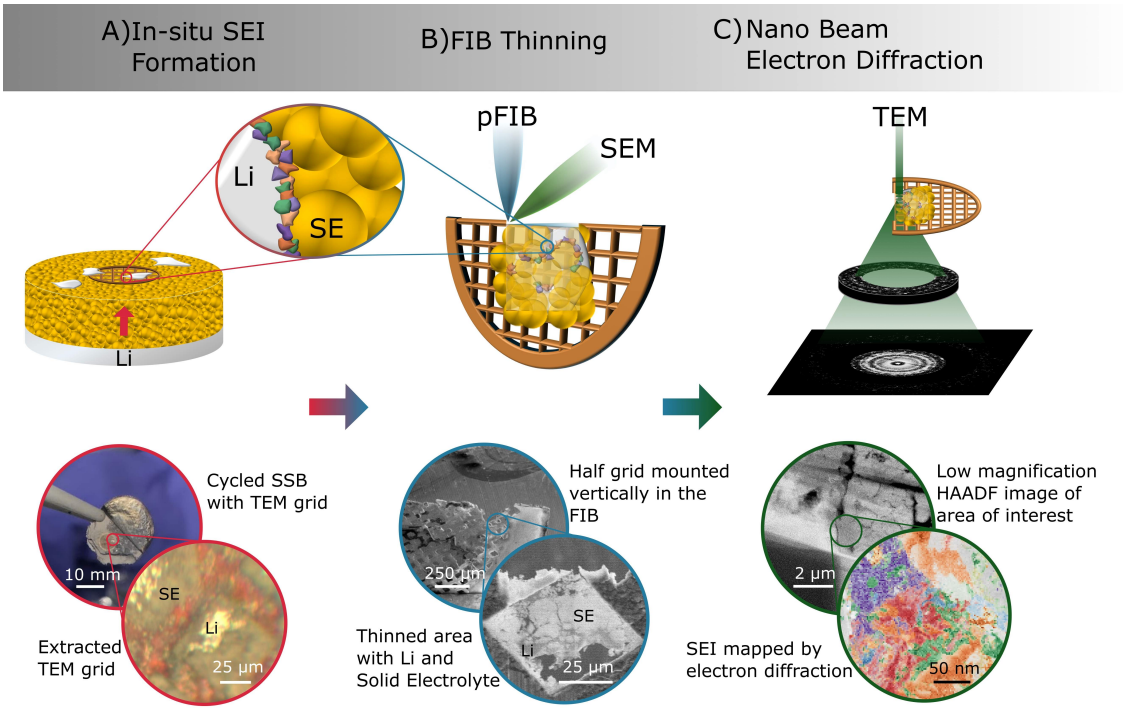


Figure 4.1: Solid Electrolyte Interphase characterization, from sample preparation to 4D-STEM acquisition. The top row denotes the individual workflow steps, from (A) in-situ SEI formation, to (B) FIB thinning and (C) 4D-STEM. The second row displays schematics of the sample at each step. In brief, (A) Li is electrochemically plated onto a TEM grid incorporated into a regular ASSB pellet. Shown are optical micrographs of the pellet and the Li-SEI-SSE interface formed between the TEM bars during plating. (B) Following cycling, the TEM grid is removed, cut in half, and Li-rich areas are thinned to electron transparency with a Xe^+ focused ion beam (FIB). SEM images show the grid pre- and post-selective area thinning. (C) Finally, thinned areas are characterized via nano-beam electron diffraction microscopy (NBED) 4D-STEM providing spatio-compositional maps of the imaged SEI. Displayed are a high-angle annular dark field (HAADF) image at low magnification of a thinned area and a NBED image post-principal component analysis.

mg of LPSCl in a 10 mm diameter PEEK mould, which generates a SSE which is approximately 700 μm thick. This is too thick to mill through even for a the high currents enabled by an ICP source. To combat this, the cell was sectioned with a razor blade (Figure 4.2 (A)). While this was effective at reducing the overall size of the sample, it did not sufficiently thin the SSE. Next, smaller amounts of LPSCl were used (Figure 4.2 (B)). This made the SSE even more brittle to the extent that it cracked during preparation or shorted during electrodeposition. Finally, 'micro-batteries' were produced using a similar technique as to what was applied in the previous section to produce the XRT sample, by using an 1 mm radius insert

into the cell (Figure 4.2 (C)). This produced a much smaller battery, which was able to be cycled, but was difficult to handle and electrode placement was difficult to ensure (see inset). Additionally, the thickness of the SSE was still such that, even with high (1 μA) currents and overnight milling it took too long to thin the specimens, and other issues were observed during this high-current milling such as cracking and sample movement (Figure 4.2 (D-F)).

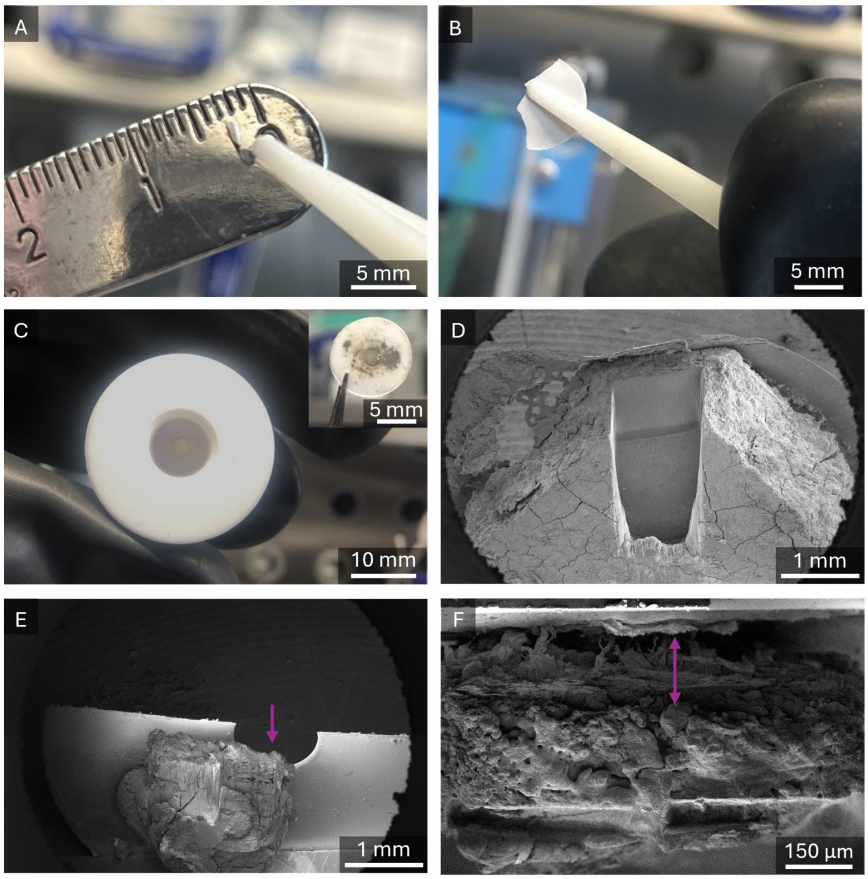


Figure 4.2: (A) Portion of a standard ASSB after sectioning with a razor blade. (B) Fractured SSE prepared with 50 mg of LSPCl. (C) 'Micro-battery' prepared with a 1 mm radius insert, with inset image showing the difficulty of ensuring correct placement of the Li electrode. (D) TEM grid incorporated into sample after overnight milling, showing severe cracking and a thick layer of SSE still to remove. (E) 'Micro-battery' sample dropping after overnight milling and securing to a TEM half-grid with Ag-eletrodag. (F) The same sample as in (E) showing the approximately 300 μm gap shown between the sample and the half-grid after overnight milling.

In Figure 4.2 (D), a TEM grid was incorporated into the SSE, but was unable to be removed without excessive damage, hence a large volume of SSE needed to be

milled. This initially suggested that incorporating a TEM grid into a cell, as is done with liquid electrolytes, is not possible with ASSBs.[56] With optimisation, this was shown to be a false assumption. As can be seen in Figure 4.3, with multi-step densification of the electrolyte, a TEM grid can be incorporated, elecotroplated with Li, and removed for thinning in the FIB. The difference with this method is that by initially compacting just the SSE at 50 MPa and then completing densification with both the TEM grid and current collector in place at 500 MPa, the SSE is incorporated into the holes in the TEM grid without covering it fully, reducing the force needed to extract it. Additionally, using lacey or holey C grids with the C-side facing the electrolyte makes them easier to extract and improves current distribution. While this method works, it was inconsistent with Cu grids and often resulted in grids which were too bent to undergo thinning or imaging easily. Using Ni grids, which do not alloy with Li, removes the potential for alloying to affect the SEI development, and their stronger mechanical properties makes it easier to extract grids without deformation.[135] This enables in-situ formation of the SEI in the cell before imaging.

To ensure that the incorporation of a TEM grid into the cell was not significantly affecting the results of electroplating, a comparison was made between a Li-Li cell without a TEM grid, and a Li half cell with a half and full Cu grid, and a full Ni grid (all with lacey C). The results are shown in Figure 4.4 (A). As can be seen, the initial deposition of Li in the half cells means that it takes longer for them to reach the stable plating voltage than the Li-Li cell which will have already formed a SEI layer, the voltage during chronopotentiometric deposition is very similar. The demonstrates no significant differential between the case with and without a TEM grid incorporated into the cell. The only significant difference is with the half-grid Cu, which undergoes a short-circuit after approximately 9 h of plating. For this reason, full grids were incorporated directly into cells, then halved with a razor blade after electroplating. Figure 4.4 (B) shows the Open Current Voltage (OCV) and electroplating profile for a representative cell using a Ni TEM grid. The stabilisation of the OCV over the 10 h resting period is visible. The trace in

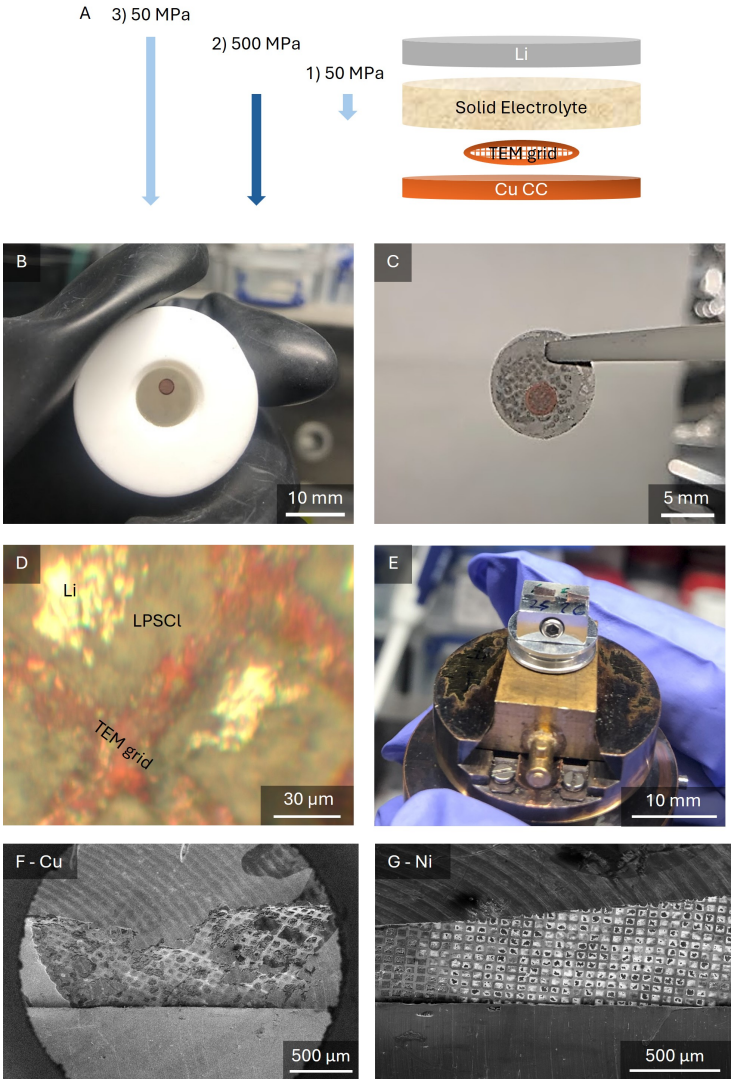


Figure 4.3: (A) Schematic of multi-step densification to incorporate a TEM grid into an ASSB and remove it for characterisation. This involves initial densification of the SSE at 50 MPa for 30 s, then full densification at 500 MPa for 3 min with the TEM grid and current collector, and finally attachment of Li at 50 MPa for 30 s. (B) TEM grid in cell casing before densification. (C) SSE and TEM grid removed from casing after Li electroplating. (D) Optical micrograph of Li and LPSCl incorporated between the bars of the TEM grid. (E) Two halves of a TEM grid mounted in a vertical holder for transfer to the FIB. (F) Cu half grid mounted vertically in the FIB after extraction from the SSE. (G) Ni half grid mounted vertically in the FIB after extraction from the SSE.

(B) is from the same cell as will be discussed later for analysis. The purple box corresponds to the electroplating section which is shown in (A).

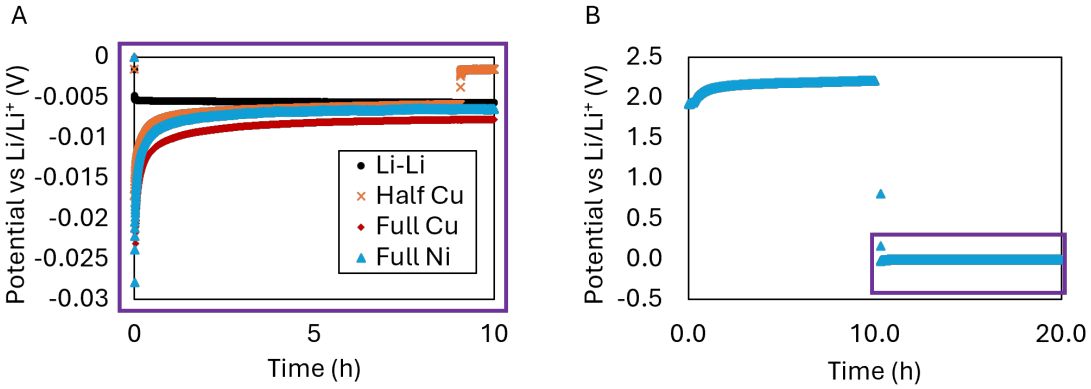


Figure 4.4: (A) Electroplating of Li in 4 cells, all using a LPSCl SSE for 10 h at 0.1 mA cm^{-1}. The Li-Li cell does not include a TEM grid (black circle), while the others include half a Cu TEM grid (orange cross), a full Cu grid (red diamond), and a full Ni grid (blur triangle). All grids are coated with lacey C and have been rested to stabilise for 10 h prior to electroplating. (B) shows the full OCV and chronopotentiometric electrodeposition of Li for the cell containing the Ni grid. This sample is used as an example for analysis discussion below.

4.3.2 Sample Thinning

The halved grids were brought into the FIB via airless transfer. An AOI must be found that has an interface between Li and the LPSCl SSE. These areas are identified through a combination of EDX and SE and BSE, as seen in Figure 4.5. The SSE can be identified in EDX from the S signal and the grid by the Cu (or Ni) signal. The P and Cl signals are in the same locations as the S signal but are fainter. The Li signal appears homogeneous because its energy is too low to be registered by the detector. The O signal can sometimes be used instead, as Li oxidises very easily, even within the microscope vacuum.[137] The EDX shown here is particularly faint as it was stopped as soon as the different areas could be confirmed, rather than waiting for a strong signal, to minimise any potential damage from continuous electron irradiation.

As can be seen in Figure 4.5 (B) and (C), sometimes the different components are clearer via SEM imaging. The low Z of Li gives good contrast with other components even in SE imaging. The areas close to where the Li has plated even appears darker, presumably due to alloying with Li. The BSE image in (C) shows the same pattern, with better contrast between the SSE and Li. This shows that

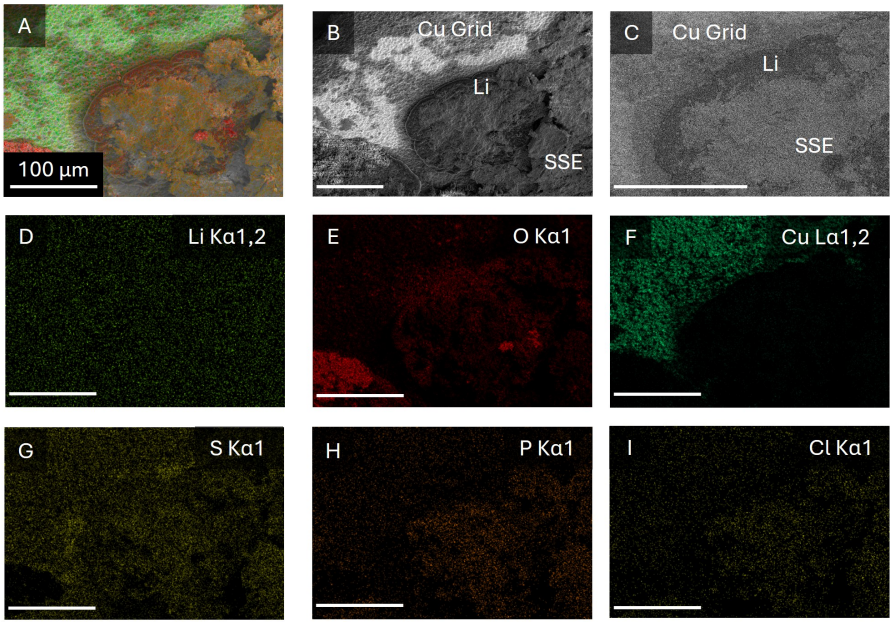


Figure 4.5: (A) EDX map of all components showing an area of interest. Single component maps shown below. (B) SE SEM image of the same area with the Cu grid, Li and SSE labelled. (C)BSE SEM image of the same are at a slightly higher magnification. All scale bars are 100 μm.

while, usually, the SE image is sufficient to determine AOIs for thinning, in some cases EDX and BSE may be helpful, in particular in cases like this where the variation in Z could be due to SSE or oxide formation.

Once an AOI has been identified, an initial high (60 nA) current mill is used to remove the grid between the interface and the AOI. This is why the grid is cut in half, to reduce the distance for this cut. The AOI should also be chosen far enough away from the edge of the grid that it has not been deformed by halving of the grid. One row of grid squares is usually sufficient. A sample after this initial mill is shown in Figure 4.6 (A). The angle of the sample is adjusted to make sure it is perfectly vertical as once the stage is cooled only small adjustments to the stage location. Necessary adjustments are usually due to bent grids which were minimised once Ni was used. A Pt protective layer is not needed as the grid bar fulfils this function, this is particularly useful when using a cryo-stage.[225] The stage is cooled and cleaning cross sections are used to thin the sample down to approximately 1 μm with 30 kV and steadily decreasing current down to approximately 4 nA. A BSE image of the same sample at this stage can be seen in (B), showing a clear

interface between the Li and SSE remains. After this, the stage is tilted between ± 0.5° and polished with 5 kV and decreasing currents down to 1 nA. Figure 4.6 (C) shows a SE image of a thin section during this final thinning process. Because of the porous and brittle nature of the LPSCl SSE, this process was not often not able to be carried out all the way through as the sample would start to crumble. It should also be noted, that while a higher current may have been used for thinning than usual, because of the wider spread of a plasma beam, the beam tails were used for thinning to prevent over-milling.

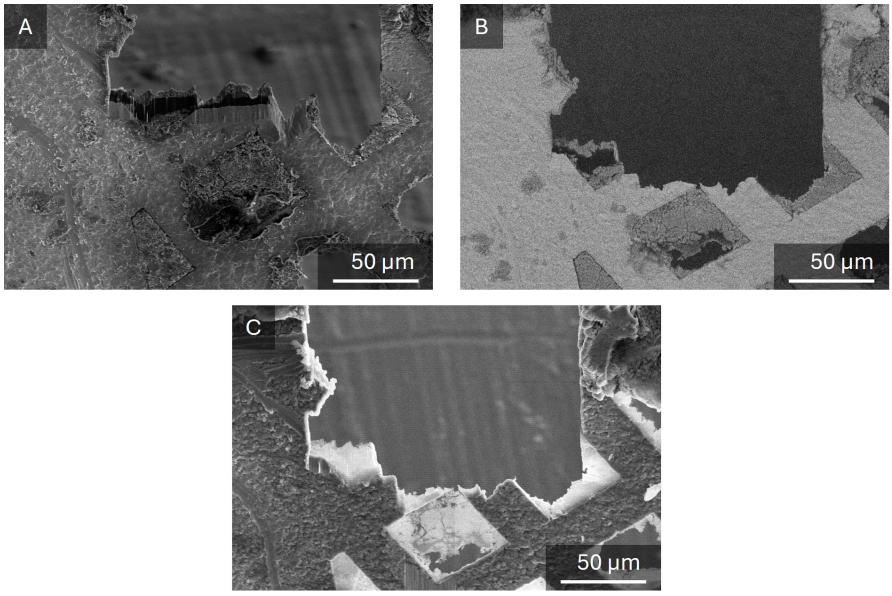


Figure 4.6: (A) SE SEM image of an AOI after inital high-current mill to access the area. (B) BSE SEM image after initial thinning without tilting the sample. (C) SE image of the same during tilting sample of the sample. Note that the AOI is not centred because the stage could not be moved once it was cooled beyond a few degrees tilting.

Incorporating the SSE and Li into a Ni grid, rather than performing a standard FIB thin-section and lift-out procedure has several benefits that can broadly be classified into two categories, sample-representativeness and ease of fabrication. The samples are more representative as the absence of a thin-section lift-out step and the associated use of organometallics during the deposition of protective layers and transport, eliminates possible detrimental side reactions between organometallics and the highly-reactive battery components. The TEM grid bars can instead act as a protective layer on top of the AOI, reducing the risk of altering the sample

during the final milling steps. The attachment of the sample to a wider frame makes it easier for heat to dissipate. The grid structure also provides support from multiple sides, and is thicker in some areas, protecting the AOI and allowing for protective membrane boxes and lint-free paper to be used to protect the sample during transport and storage without direct contact with AOI which could cause side reactions, changing the structure of the Li, SSE, and SEI.

Sample preparation in this way aids ease of fabrication as multiple areas can be located or prepared on the same grid, alleviating over-thinning or thin-section fracture concerns during thin section preparation or lift-out. The latter is particularly useful when using a plasma FIB as the large beam-tails make it challenging to produce high-quality thin sections.[226] A plasma FIB is needed, as Ga and other metals alloy with Li and can lead to artifact phases.[189] As the FIB source has been observed to arc when milling Li at mid-low currents (> 4 nA) due to Li travelling up the column, this minimises the need for Li milling, reducing the time needed to thin each section. Two thinned areas can reliably be produced within 8 hours. If Li is observed to already be thin enough in a given AOI, cryogenic temperatures may not even be necessary for milling if the Li can be avoided.

4.3.3 Microscope Workflow

With such reactive samples, it is imperative that they do not come into contact with air. In previous works, they have used cryogenic transfer holders to avoid reactions by keeping samples at cryogenic temperatures despite short periods of transfer in air.[56] In this case, the only cryogenic temperatures used were doing FIB of Li. Therefore, extreme care had to be taken to avoid exposure. This involved using the specially designed holders shown in Figure 4.7 to transport samples between Ar gloveboxes (O_2 and $H_2O < 0.1$ ppm) and the microscopes. The only time samples were not in these holders or stored in a glovebox was during transport between microscopy facilities. During transport, the samples were protected by membrane boxes vacuum sealed in pouches for batteries within a glovebox and then triple bagged within the glovebox to ensure an inert atmosphere

was maintained. On removal of packaging before loading into the TEM holder there was no observable spike in O_2 or H_2O level and the Li on the grids still appeared shiny, showing that it had not oxidised.

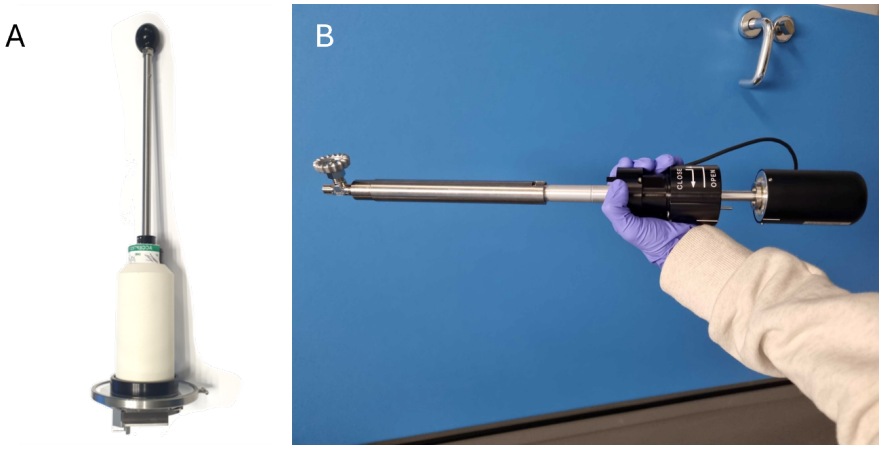


Figure 4.7: (A) Gatan iLoad holder used to transfer samples between the glovebox and the FIB. Loaded and unloaded within the glovebox. (B) JEOL air-isolation Beryllium Transfer holder used to transfer samples from the glovebox into the TEM.

The majority of previous studies on the SEI have used cryo-TEM to enable imaging of the highly beam-sensitive Li, SSE, and SEI components via high-resolution imaging, EELS or EDX, which all require high electron doses.[56, 61, 157] That was the initial direction of this investigation as well. There are significant technical challenges to utilising cryo-TEM. Figure 4.8 shows some of the challenges uncovered during attempts at cryo-TEM early in this study. (A)-(D) are from the development of a cryo-FIB-TEM workflow during a stint with the Warner lab. While the system was developed to the extent where FIB samples could be created with liquid electrolytes, the image in (D) is the only sample to make it into the TEM, and it was too covered in ice to obtain meaningful data. On returning to Oxford, we attempted to develop a cryo-workflow here. Unfortunately, these efforts were held back by holder functionality and ice-formation issues ((F) an (G)).

4.3.4 4D-STEM Validation

To image the samples, 4D-STEM was used as analysis of the diffraction patterns should enable component mapping of the SEI using much lower doses than with

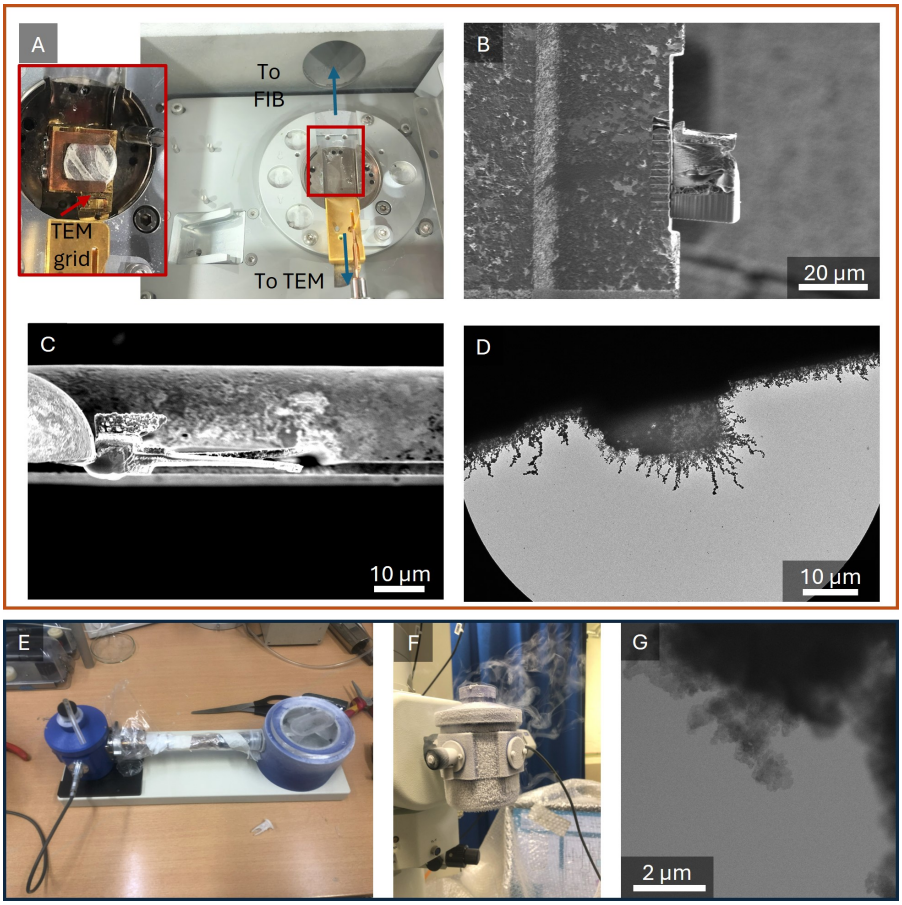


Figure 4.8: Images from work with the Warner group at UT Austin are within the dark orange box. Images from work at Oxford are within the dark blue box. (A) Leica vacuum cryo transfer system utilised to transfer samples under cryogenic conditions between the glovebox, FIB, and TEM. (B) Li-frozen liquid electrolyte FIB lamella after attachment to a FIB grid via redeposition. (C) The same lamella after further thinning resulting in separation between the electrolyte and Li. (D) Low magnification BF TEM image of a Li-frozen electrolyte lamella loaded into the TEM covered in ice. (E) Fischione 2550 Cryo Transfer Tomography Holder used at Oxford. (F) Frosty outside of the Fischione holder showing that there was an issue with the vacuum jacket so it was not able to hold temperature. (G) BF TEM image of sample brought into the TEM at Oxford with significant ice build-up.

other techniques such as EDX or EELS.[174] This technique had never been used to investigate the SEI on Li metal until it was reported earlier this year, after this work had been completed.[227] An appropriate camera length was chosen to ensure that the majority of the diffraction spots were visible while ensuring a good spread of the points for ease of analysis, as shown in Figure 4.9 this was 40 cm. A low convergence angle (1 mrad) improves resolution in reciprocal space and a reasonable probe size (approximately 1 nm). An accelerating voltage of 300 kV was used. While this would

also exacerbate knock-on damage, the low Z of the elements being investigated make this hard to avoid even when relatively low accelerating voltages are used.[182] Finally, because the components can be determined from the diffraction pattern in 4D-STEM, a larger field of view can be used to map across the interface at a mid-resolution, rather than having to use high resolution to obtain lattice contrast.

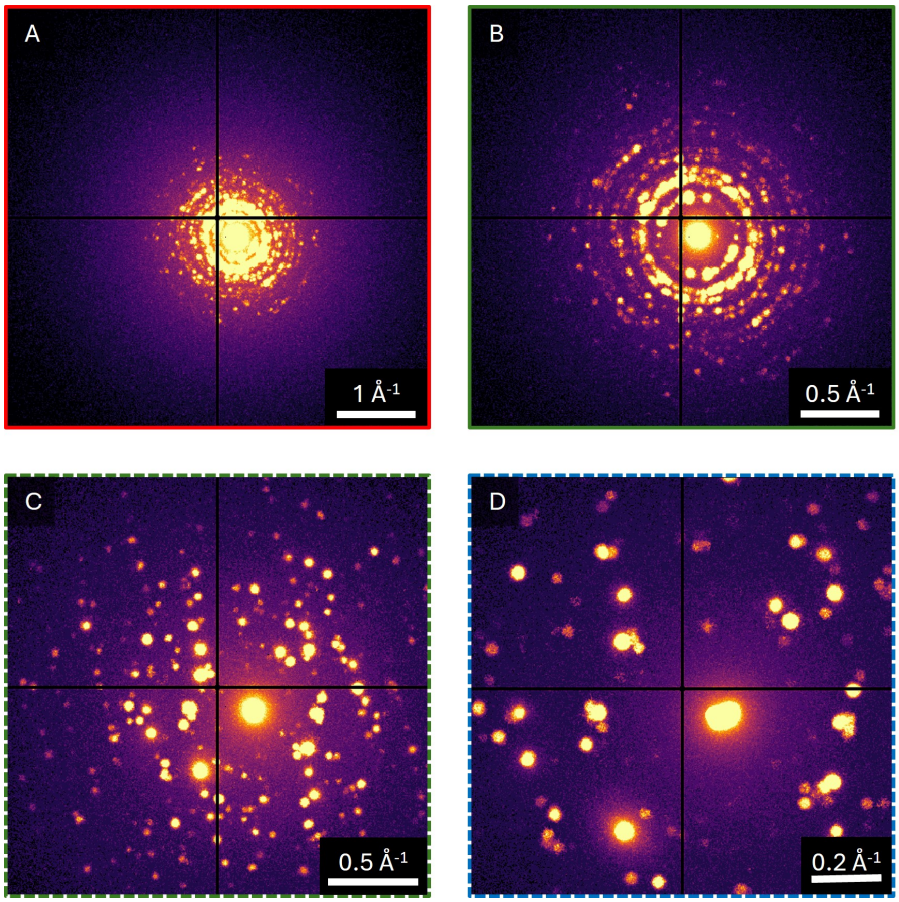


Figure 4.9: (A) Summed diffraction pattern across a sample area at 20 cm camera length. (B) Summed diffraction pattern across the same sample area as in (A) but at 40 cm camera length. (C) Different area of the sample summed diffraction pattern at a camera length of 40 cm. (D) Same sample area as (C) summed diffraction pattern at a camera length of 80 cm.

To ensure minimisation of radiation damage, diffraction patterns were compared after imaging at different locations in the sample. As representative set of images is shown in Figure 4.10. The top row shows virtual BF images of the sample location, with the difference between the two images shown in (C).[215] The respective images for the summed diffraction pattern across this area are shown in the row below

((D)-(F)). The dose between the first and second set of images is approximately 12 e^{-} $Å^{-2}$. As can be seen in (C) and (F), there are some small differences in the images which appear to mainly be associated with very thin areas of the sample. While there is some difference in the brightness of spots in the diffraction patterns, none have fully disappeared. This electron dose was deemed to be sufficient to obtain good diffraction patterns without significant sample damage. This electron dose is more than an order of magnitude below what has been used to investigate the SEI in samples with cryo-TEM, because these use techniques such as EDX and EELS which require much higher doses to obtain sufficient signal-to-noise ratios.[56, 61, 180] As 4D-STEM relies on coherent scattering for component determination, and this is much more dose efficient with at direct electron detector, much lower doses can be used.[173, 227–229]

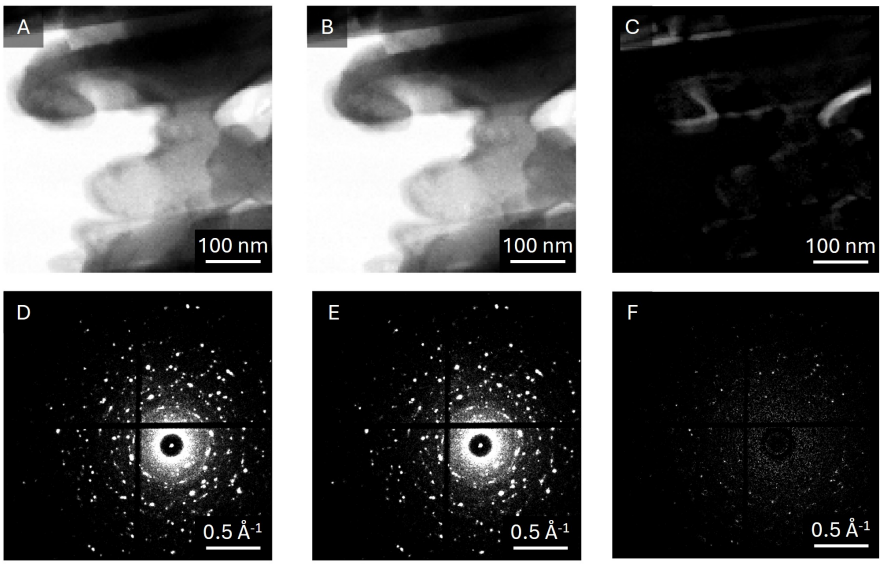


Figure 4.10: (A) and (B) are the intensity (BF) images of same area, with (B) taken after (A). (C) Is the difference between the two images. The electron dose per image taken is approximately 4.16 e^{-} $Å^{-2}$ and two other images were taken between (A) and (B) so the total dose extra dose received by (B) is approximately 12.48 e^{-} $Å^{-2}$. (D) and (E) are the summed diffraction patterns corresponding to (A) and (B), respectively. (F) is the difference between the two.

Finally, to ensure that the expected components are attributable via 4D-STEM, initial component matching was done. Using the area shown in Figure 4.11, the diffraction pattern was converted to a radial profile spectrum and the peaks were

matched to the expected component with a peak at lowest error. This method identified all expected SEI components (Li_xP, LiCl, and Li_2S) as well as the SSE (LPSCl), and evidence of Li (Li_2O). This shows that this technique can be used to identify components at the SSE-SEI-Li interface. As 4D-STEM is a very powerful technique for analysis, there are a wide variety of analytical workflows which could be applied to these datasets. This will be explored further in the next chapter.

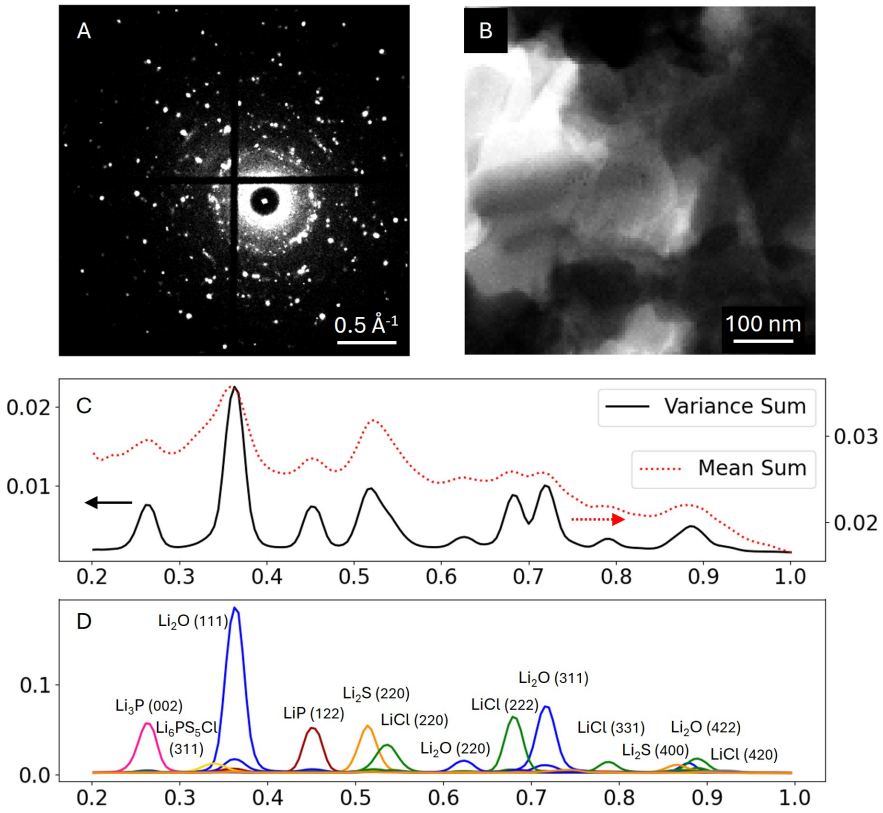


Figure 4.11: (A) Summed diffraction pattern across the area shown in (B). (B) Shows the intensity (BF) image for the sample area. (C) Shows the diffraction pattern converted to a 1D radial distribution function as a variance (black solid line) and mean (red dashed line) sum. (D) Shows the different peaks in the radial distribution function attributed to the most likely component.

4.4 Conclusion

Here, a novel method for preparing and analysing samples to investigate the SEI in between Li and SSEs has been presented. A TEM grid was incorporated into

an ASSB via a multi-step densification process, allowing it to be removed after electrodeposition without significant deformation. It was then thinned via cryo-FIB to electron transparency and imaged via 4D-STEM. Throughout, care was taken to ensure that the samples were not exposed to air and any artifacts due to beam damage were investigated and minimised. This technique would be applicable to a wide array of SSEs, not just LPSCl which was used to demonstrate it here. It is also compatible with incorporation into ASSBs for analysis of changes in the SEI with different cycling conditions. Further analysis of the datasets generated via this technique will be discussed in the next chapter.

4.5 Experimental Detail

4.5.1 Materials

Li_6PS_5Cl solid electrolyte, 10 μm particle size, was purchased from Ampcera (99.9%). TEM grids were purchased from Agar Scientific (400 mesh Ni and Cu grids with lacey carbon). Current collectors were punched as 10 mm disks from Ni (Advent Research Materials, 99.95 %) and stainless steel (Goodfellow) sheets. The current collectors were washed with ethanol and acetone and left to dry in a vacuum oven at 60 °C overnight. Li metal foil (99.9%) was purchased from Alfa Aesar. Before use the oxide surface layer was mechanically removed and the Li foil calendared ($\approx$ 200 μm). Lastly, 10 mm disks were punched out of the Li and Ni foil. All operations were carried out and materials stored in an Ar glovebox (MBraun; H_2O <0.1 ppm, O_2 <0.1 ppm) unless stated otherwise.

4.5.2 Cell Preparation

ASSBs were assembled and cycled using an air-tight cycling rig, consisting of an outer steel casing and an interior Maccor tube in which the cell components are assembled. The ASSB is cycled at fixed pressure of 5 MPa, applied by spring-loaded stainless steel pistons placed on either side of the ASSB. 100 mg of LPSCl was added to the Maccor tube, compacted at 50 MPa for 30s using a hydrostatic press, then the TEM grid and current collector were added on the same side and

the stack was densified at 500 MPa for 180 s. Li was attached to the opposite side by pressing at 50 MPa for 30 s.

4.5.3 Electrochemistry

Cells were cycled within an environmental chamber at a temperature of 30 , under 5 MPa. Cells were left to rest for 10 h to allow their temperature and open-circuit voltage to stabilize. Li was plated onto the Ni current collector and TEM grid at 0.1 mA cm^{-2} using a Biologic VMP3 potentiostat for 10 h.

4.5.4 Focused-Ion Beam Thinning

After cell disassembly, the grids were removed from the cells with tweezers and cut in half with a razor. The half-grids were mounted vertically on vice stubs and transferred to a plasma FIB-SEM (Helios G4 PFIB CXe DualBeam) in an airless transfer vessel (Gatan iLoad). Areas of interest, were identified and the surrounding area was cleared using high current milling (30 keV, 0.2 μA), then the area of interest was thinned using progressively lower currents to electron transparency (minimum 5 kV, 1 nA). The final milling steps were performed using the beam tails by slightly offsetting the milling position. The half-grids with thinned areas were then transferred back into the glovebox, and placed in a membrane box between layers of lint-free paper and vacuum-sealed within a pouch. The latter was deemed necessary to protect the samples against mechanical damage and chemical changes prior to TEM examination.

4.5.5 4D-STEM

Samples were loaded into a JEOL Air-isolation Beryllium Transfer holder (EM-01380STBTH) and transferred into the TEM without air exposure. A JEOL ARM300CF microscope using a current of approximately 0.4 pA (0.5-0.6 pA measured by Faraday cup with 0.1-0.2 pA dark current)., measured with a Faraday cup, in nanobeam mode with a convergence angle of approximately 1 mrad, and accelerating voltage of 300 kV was used to collect diffraction pattern on a Merlin

MediPix direct electron detector, with an active area of 28 mm^2 and 512 $\times$ 512 pixels (pixel size 55 μm^2). NBED images were recorded using a scanning nanobeam of 1 nm across a 256 x 256 scanning grid. The pixel dwell time was 600 μs, providing a sufficient signal-to-noise ratio for data collection, while avoiding radiation damage.

If you think about a crystal or just anything around you, when you put it in a microscope, suddenly you see it in a totally different way.

— Lena Kourkoutis, Professor at Cornell University, renowned electron microscopist especially for her work in cryo-microscopy

5

Characterisation of the Li-Solid Electrolyte Interphase formed with Sulphide Argyrodites

Contents

5.1 Abstract 114
5.2 Introduction 114
5.3 Results and Discussion 116
5.3.1 Set-up and Calibration 116
5.3.2 Component Matching 116
5.3.3 Algorithm Choice 119
5.3.4 Spatial and Compositional Analysis 121
5.3.5 Comparison with LPSClBr 125
5.4 Conclusion 127
5.5 Experimental Details 127
5.5.1 Materials 127
5.5.2 Sample Preparation 128
5.5.3 4D-Scanning Transmission Electron Microscopy 129
5.5.4 Calibration 129
5.5.5 Electron Diffraction Image Analysis 129
5.5.6 Virtual Electrode Plating - X-Ray Photoelectron Spectroscopy (VEP - XPS) 131

5.1 Abstract

All-solid-state batteries with a Li metal anode, promise improvements in energy density and safety compared to current Li-ion technologies. Understanding the solid electrolyte interphase (SEI) is crucial to the development and optimization of ASSBs. This is a nanoscale and heterogeneous layer which forms between Li and the solid electrolyte due to chemical and electrochemical reactions. However, charactering the SEI has proven challenging due to its size, buried, and reactive nature. Here, 4D-STEM is used to map the spatio-compositional structure of the interphase at room temperature. The capabilities of this approach are showcased by characterizing the SEI formed between Li_6PS_5Cl and Li, and comparing it to that formed with $Li_{5.5}PS_{4.5}Cl_{0.75}Br_{0.75}$.

5.2 Introduction

ASSBs, integrating a SSE and Li metal negative electrode, would provide a step-increase in energy density and safety compared to traditional lithium-ion batteries[95, 97]. Crucial to their performance and optimisation is an in-depth understanding of the SEI. The SEI is a reactive layer which forms between Li and electrolytes due to the high reactivity of Li. It has been observed to be on the order of 10s to 100s nm thick, depending on characterisation technique, electrolyte, and cycling conditions.[56, 106, 125, 135, 223] While there is no consensus regarding SEI structure, in particular in ASSBs, a heterogeneous structure of Li-rich SSE decomposition products containing nano-crystalline domains within an amorphous matrix, and layered structures are commonly suggested.[44, 64] Ideally, a SEI should be electronically insulating (self-passivating), ionically conductive, and homogeneous in composition to promote homogeneous stripping and plating without continuous growth.

With promising SSEs, the SEI has been shown to deviate from these conditions as well as changing with cycling conditions.[135, 230, 231] Differences in the composition, structure, and thickness of the SEI can affect the interfacial resistance,

plating behaviour and cause battery failure.[99, 155] Despite its importance, the SEI in ASSBs has been challenging to characterise due to its thin, buried, and reactive nature. Electrochemical techniques have indirectly tracked its behaviour, but physical characterisation remains challenging.[135, 231, 232] XPS has confirmed the chemical components in the SEI, but its low penetration depth and spatial resolution prevent a direct measure of the SEI structure.[139, 230, 232] ToF-SIMS combined with AFM has a much higher spatial resolution, but differences in milling rates and complex analysis introduce uncertainty in the exact composition and structure.[125, 233] Cryo-TEM has enabled atomic-resolution SEI characterisation in liquid electrolyte systems, but sample preparation challenges have limited its use with ASSBs.[56, 61, 223] The fragility, reactivity, and radiation-sensitivity of ASSB components make preparation and lift-out of thin sections ($<$ 100 nm thick) challenging . Only LiPON and polymer SSEs, which form dense, thin, and robust films have had the full SSE-SEI-Li interface characterized via TEM.[157, 234] For the commercially-promising sulphide argyrodites, a singular publication mechanically detached dendrites from ASSBs, but were not able to image the full SSE-SEI-Li cross-section[154]

Building on the technique development discussed in the previous chapter, this chapter will discuss analysis of the 4D-STEM datasets, confirmation of components with XPS and statistical analysis of the component co-location in the SEI. Analysis confirmed a complex structure. The size of crystallites within the SEI is shown to be significantly larger than reported with other SSEs and liquid electrolytes. While the average size is around 20 nm^2, SEI crystallites are observed on the order of 100 nm^2. Finally, a comparison is made with LPSClBr, which has a much finer nanostructure. Statistical analysis shows that despite the difference in the crystallite size, a similar structure is observed.

5.3 Results and Discussion

5.3.1 Set-up and Calibration

To discuss the analysis of the 4D-STEM datasets generated, an example dataset will be used; the same as shown in Figure 4.11. It consists of a Li electroplated onto a Ni TEM grid incorporating LPSCl. 1 mAh cm^{-2} of Li was plated at 0.1 mA cm^{-2}, followed by grid removal and thinning with cryo-FIB. The sample was then transferred under inert conditions to a JEOL ARM300CF for imaging with low-dose 4D-STEM. A combination of low magnification (20kx) HAADF images and 'blind' 4D-STEM mapping at higher magnification (200kx) was used to minimise beam exposure. Each 4D-STEM image used a probe size of approximately 1 nm, a dwell time of 600 μs, and a current of approximately 0.4 pA, resulting in a sample exposure of ≈ 4 e^{-} $Å^{-2}$. As shown in Figure 4.10 this does not induce significant sample damage. A low convergence angle was used (approximately 1 mrad) t lower electron dose per area onto the sample and improve reciprocal space resolution.[172]

Once collected, the datasets were corrected via established py4DSTEM workflows.[174] An example is shown in Figure 5.1 (A-F). This ensured that the data was aligned, any ellipticity was removed, and hot pixels were corrected. The data was then converted to 1D radial variance profiles using scripts written provided by ePSIC (Figure 5.1 (G-H).

5.3.2 Component Matching

Component Corroboration

The 1D Diffraction pattern (DP) can be matched to components based on the spacing of peaks and theoretical d-spacings of these components. The most common way to determine the chemical components of the reaction between Li and LPSCl is XPS.[106, 139] This was used here to confirm components for peak matching. Li was plated using the electron beam as a "virtual" electrode and alternated with spectrum collection.[159] The changes in binding energy and peak intensity can be attributed to reactions between Li and the LPSCl; SEI formation and inter-SEI reactions.

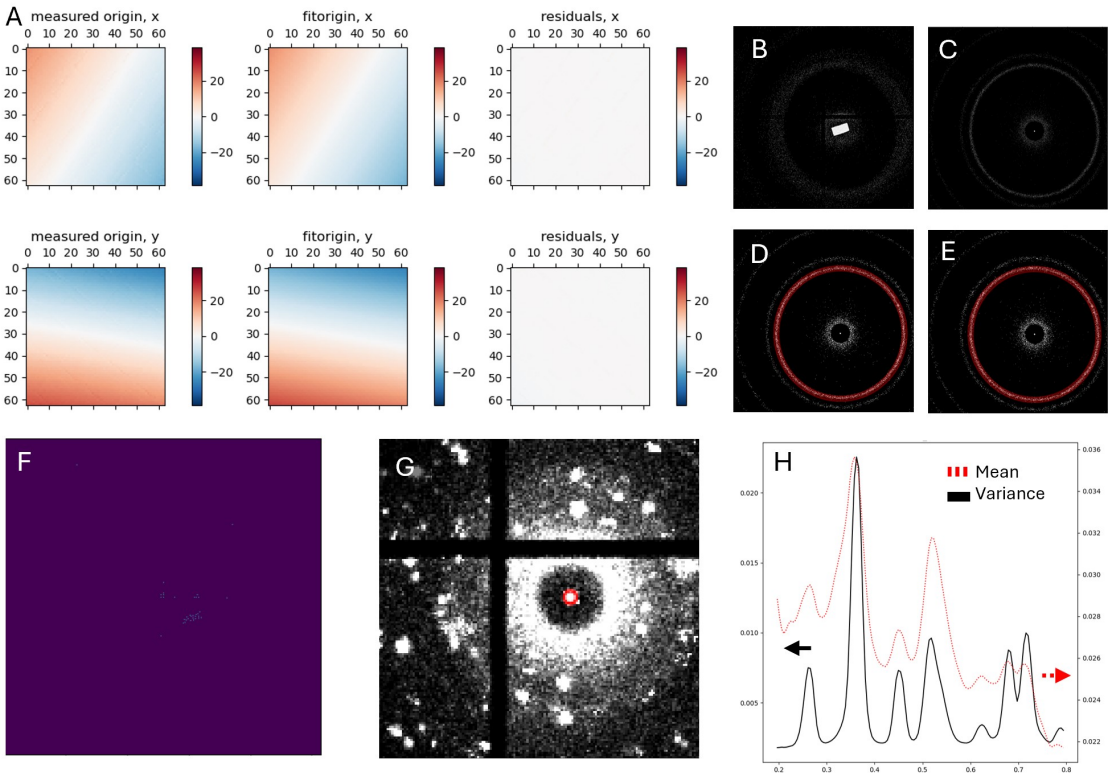


Figure 5.1: Calibration steps for the analysis of the 4D-STEM data. (A) shows the fitting of a plane to the beam centre to ensure it is aligned with (B) and (C) showing the diffraction pattern alignment before and after fitting of this plane. (D) and (E) show before and after correcting for elliptical distortions. (F) shows the mask used for the removal of hot pixels. These corrections were done using py4DSTEM scripts.[174] (G) shows the summed diffraction pattern for a dataset after alignment with (H) showing the same dataset converted to a 1D pattern as a mean or variance-based radial profile.

As Li plates onto the SSE, the Binding energy (BE) of Li, initially reflective of LPSCl, reduces in response to the formation of a SEI layer on top the SSE. Following a cumulative 12.7 s of plating, a peak indicative of Li metal appears at an even lower BE.[106] This peak grows in prominence with continued plating, while the contribution from Li_6PS_5Cl decreases due to XPS probe depth limitations ($<$ 10 nm). With Li plating, the P signal also reduces in BE, first from PS_4 to Li_xP, then a Li_3P peak appears after 8.5 s. The Li_xP signal shifts towards the Li_3P with further plating, indicating an increase in the value of x. The S signal shifts towards Li_2S at lower BE as Li plates, and by the time a Li metal signal appears the PS_4 contribution has almost entirely vanished, demonstrating decomposition of the Li_6PS_5Cl into Li_2S. The Cl signal shows no change in BE, as the BE of the

thermodynamically favourable decomposition product, LiCl, is indistinguishable from that of Li_6PS_5Cl.[99, 235] Finally, at the same point that Li metal appears, so does Li_2O, demonstrating that even in the high vacuum of the XPS Li will oxidize, therefore Li_2O co-locates with Li.[137]

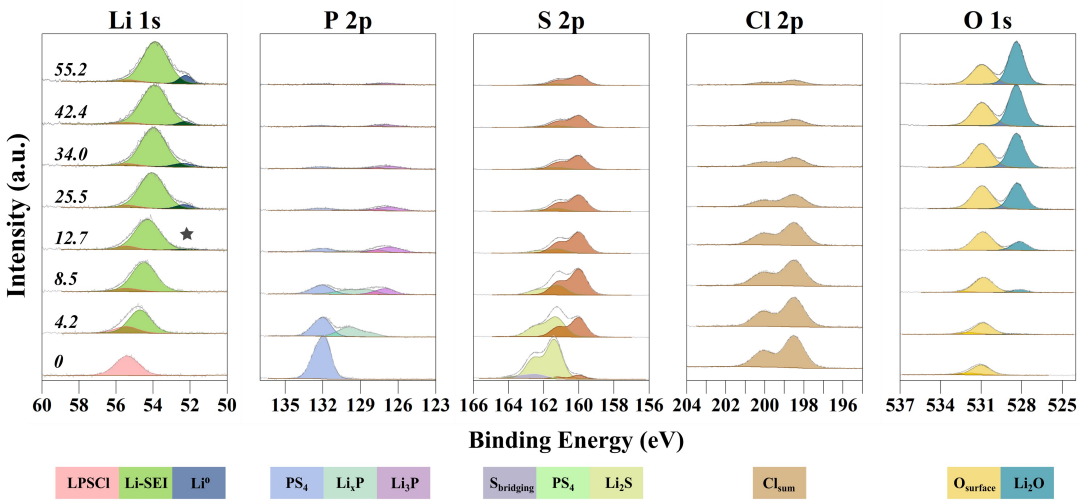


Figure 5.2: Virtual Electrode Plating - X-Ray Photoelectron Spectroscopy of Li being plated through LPSCl. Li is plated as you move up the figure, according to the time stamp along the left-hand side in seconds. The different columns correspond to different elemental changes and the compounds they have been matched to are along the bottom of the image. XPS and signal attribution conducted by Yi Liang.

Peak Choice Algorithm

The expected components (LPSCl, Li, Li_2O, Li_3P, LiP, Li_2S, and LiCl) were matched to loading vectors by finding the lowest error between theoretical electron diffraction plane positions for all expected components and the peak position of the loading vector. Matching of prominent loading vectors included structure factor considerations, limiting the pool of theoretical planes to those which diffract more strongly.[236] For loading vectors where multiple components could be matched, the error comparison for secondary peaks was also considered. Further information can be found in the Experimental Methods or the code itself in Appendix A. The Z and crystallinity dependence of electron diffraction means that higher-Z and more crystalline components are easier to identify.

5.3.3 Algorithm Choice

Three algorithms were investigated for deconvolution of the datasets into components. Principal component analysis (PCA) has been utilised for analysis of spectral datasets from TEM such as EELS and EDX.[237] However, in this case negative value generation led to complex component vectors which were difficult to interpret physically. This can be seen in Figure 5.3 (B). The Ordering points to identify the clustering structure (OPTICS) clustering algorithm has been used to automatically group EELS data into physically meaningful clusters.[238] Due to the complexity of data, the input parameters (minimum cluster size, steepness change between clusters, and minimum sampling number) had a significant impact on the cluster size and location, reducing the value of this algorithm for this application. Non-negative matrix factorisation (NMF) is similar to PCA, but only allows positive values in the separated DPs. This provided clear and easily interpretable peak locations.[239] Across all three of these algorithms similar clusters were established, as can be seen in the maps in Figure 5.3. NMF provides the clearest maps and easiest data for interpretation so it was used for this further analysis.

Error analysis was performed to determine the optimal number of loading vectors (component DPs) to use for NMF.[240] The mean squared error was evaluated with an increasing number of loading vectors. The percentage change in error was calculated to determine when the marginal improvement in error became insignificant. This is shown in Figure 5.4. After 13 loading vectors, the change in error plateaued below 1.5 %, indicating only marginal benefits from incorporating further loading vectors.

Spatial distribution analysis of the components was performed by summing the data for each loading vector assigned to a single component. A Density-Based Spatial Clustering of Applications with Noise (DBSCAN) algorithm clustered the data, then it was converted to Polygons in Shapely for analysis. The results of this process on the dataset discussed above can be seen in 5.5. The algorithms used to produce generate these shapes and analyse their relationship are shown in Appendix A.2.

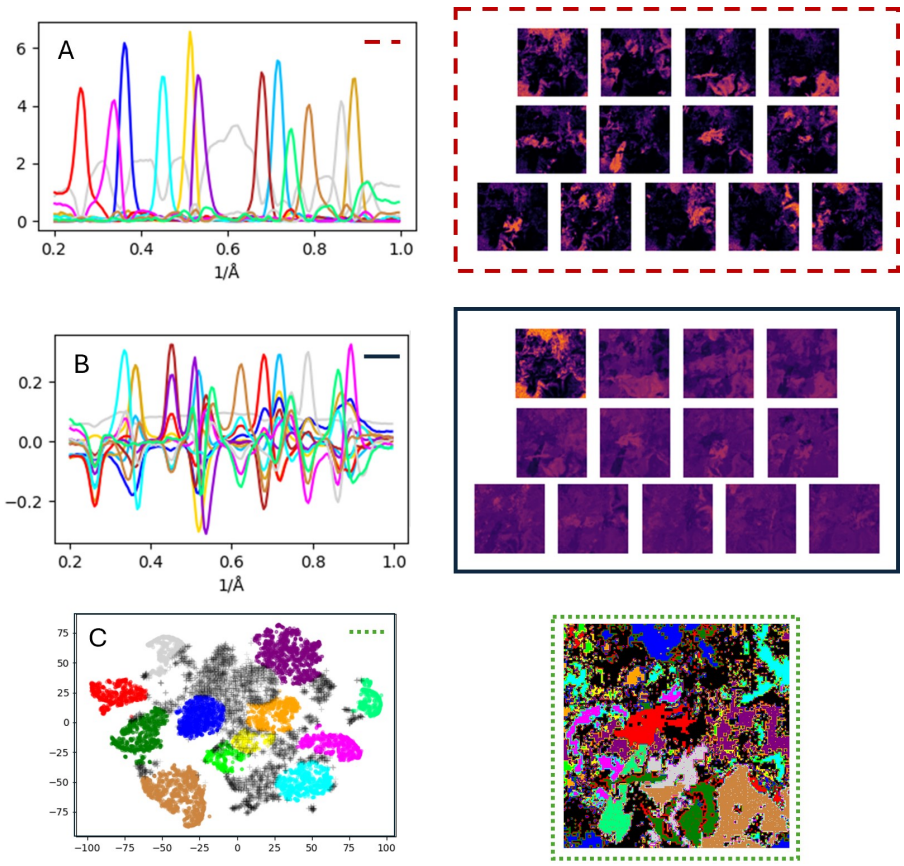


Figure 5.3: (A) Decomposition of variance radial profile shown in Figure 5.1 (H) via NMF with 13 loading vectors. The corresponding maps are shown in the red dashed box. (B) Decomposition of the same profile by PCA with 13 loading vectors. The corresponding maps are shown below in a blue solid box. (C) Automatic clustering of the same data using OPTICS.[238] The corresponding map is shown in the green short-dashed box.

To obtain a statistical analysis of the spatial relationship between the different components, multiple areas of the sample analysed in the way described above. The Pearson correlation coefficient between each pair of components was analysed by comparing the intensities of the component maps, and the distance between the components was determined using the distances between the centres of the shapes generated as described in Figure 5.5. For the LPSCl sample which has been discussed up to this point, 7 areas were averaged for the statistical results. In addition, a LPSClBr sample was analysed as a comparison point with different chemical and morphological properties. In that case, 4 areas were averaged for the statistical results. The colour maps for these areas can be seen in Figure 5.6.

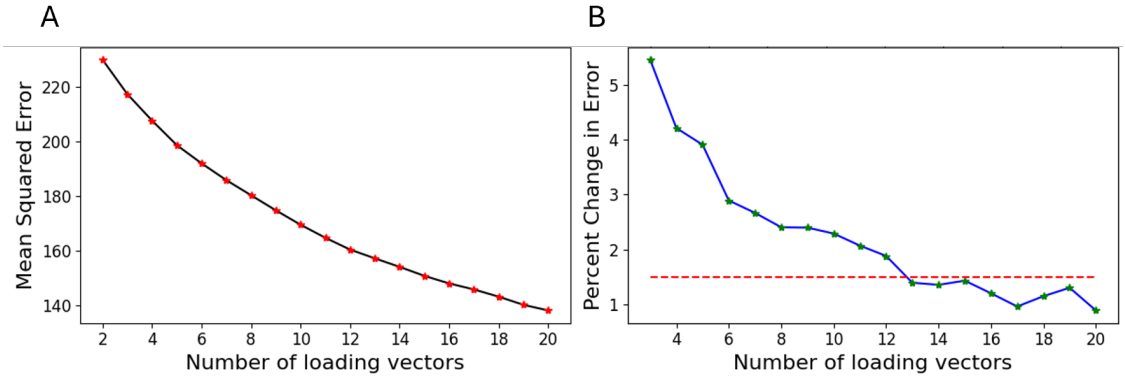


Figure 5.4: (A) Mean squared error between the loading vectors and original variance dataset with increasing number of loading vectors. (B) Percent change in error to add the loading vector shown on the x axis. The red dashed line is 1.5 %.

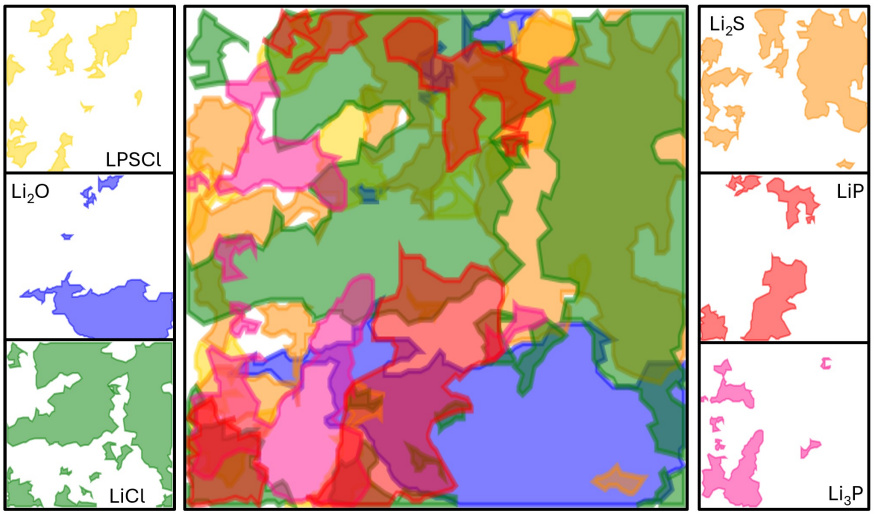


Figure 5.5: Component cluster maps on either side of an overall map of all the component clusters based on DBSCAN and then conversion to a Shapely Polygon for further spatial analysis.

5.3.4 Spatial and Compositional Analysis

Analysis of a Representative Dataset

The nano-structure of the SSE-SEI-Li interface formed with sulphide argyrodite SSEs has not been characterised, despite significant research efforts into the composition and structure of this interphase.[106, 125, 135, 154] As can be seen in Figure 5.7, the components are able to be mapped across the full SSE-SEI-Li interface using low-dose 4D-STEM. (A) and (E) show the virtual BF image and compositional map for this area, respectively. The radial variance profile (1D DP) for mean and variance

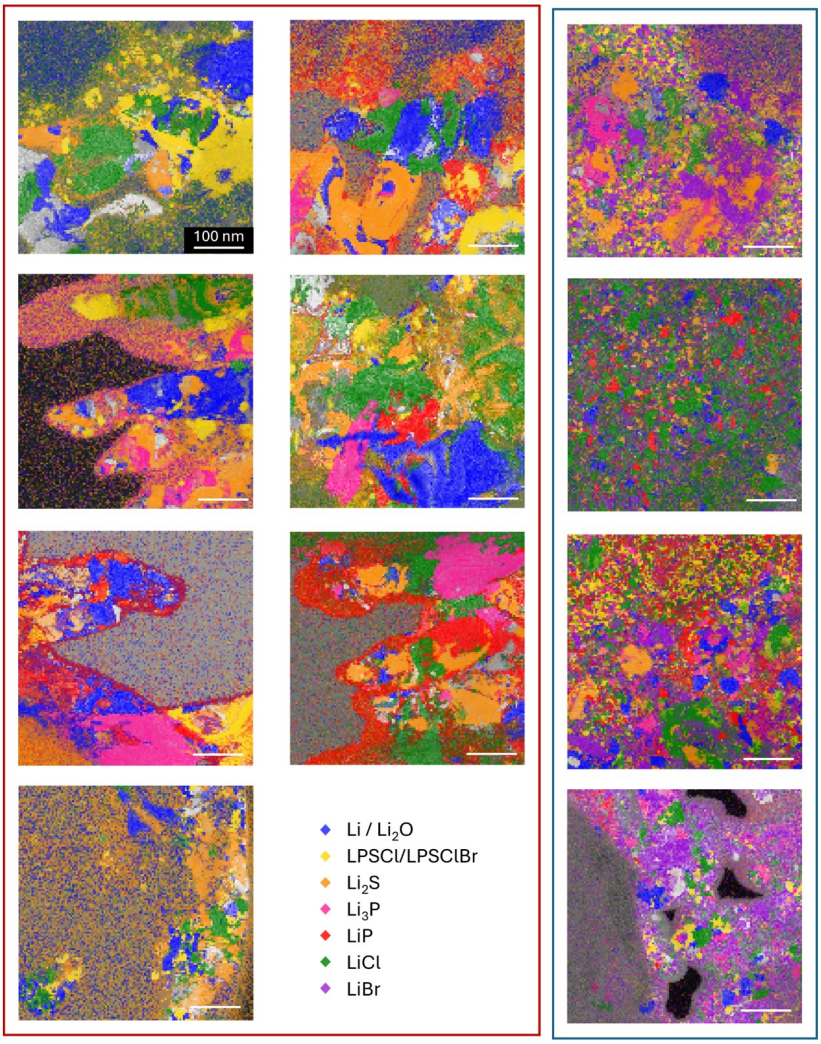


Figure 5.6: Compositional colour maps of all the areas of the samples used for statistical analysis. Red box: areas used for statistical analysis for LPSCl SEI. Blue box: areas used for statistical analysis for LPSClBr SEI. The key corresponds to both solid electrolytes. All scale bars correspond to 100 nm.

profiles summed across the sample can be seen in (B). The image in (C) then shows the mean profile for each loading vector across the sample, showing a good match with the variance profile in (B). Two loading vectors maps not shown were labelled as noise. Their mean loading vectors are shown in grey but are not labelled.

The individual component maps are shown in Figure 5.7. For all SEI components, but particularly LiCl, LiP and Li_3P, large crystallites on the order of several 10s nm^2 are visible, as well as smaller crystallites. Although Li is not directly observed, this is expected due to its low Z. Li_2O can be used as a proxy as Li will oxidise

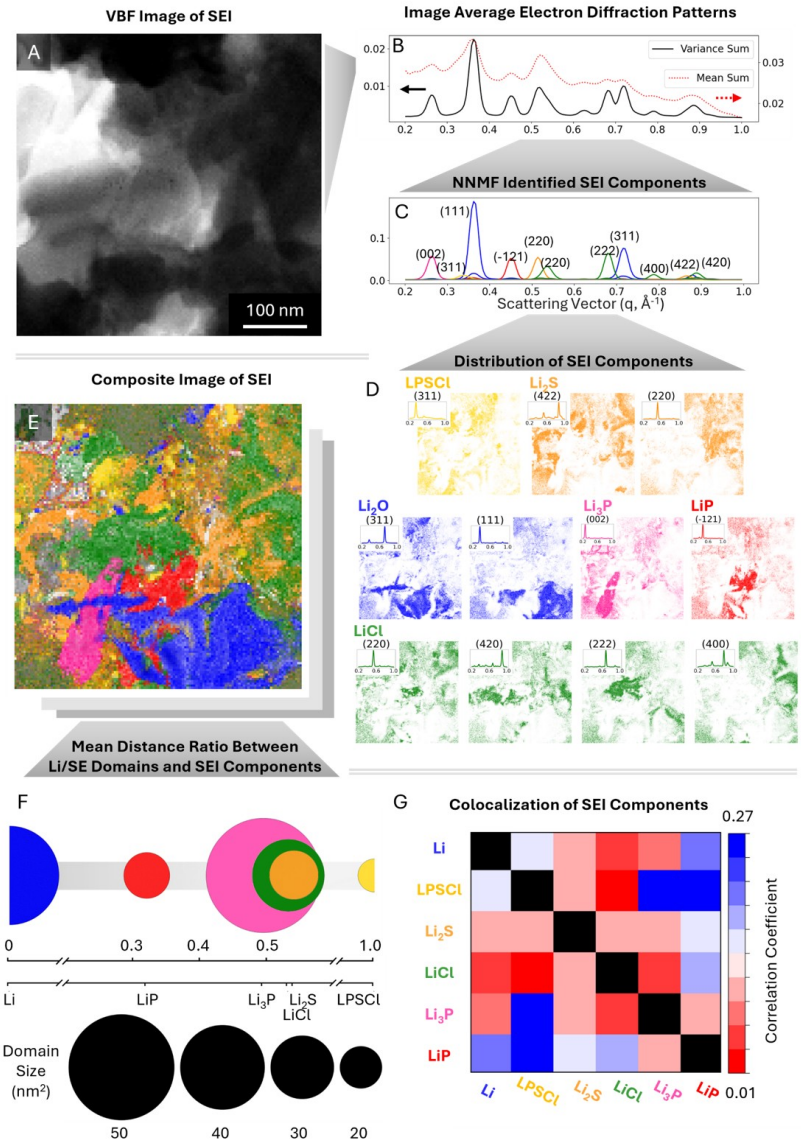


Figure 5.7: (A) Virtual BF image of the SSE-SEI-Li interface. (B) 1D mean and variance radial profiles (C) Individual loading vectors scaled to their intensity in the variance radial profile. (D) Individual component maps corresponding to each loading vector labelled with their plane orientation. (E) Compositional colour map containing all matched loading vectors. (F) Bubble plot showing the average distance of SEI components to Li (left) or LPSCl (right). The Bubble size represents the average domain size. (G) Correlation coefficients between the different components.

even in UHV environments, as noted in the XPS section and literature.[137] Based on the size of the SEI component crystallites and the spacing of Li and LPSCl above, an SEI thickness on the order of 200 - 300 nm is expected, which agrees with observations from ToF-SIMS and XPS.[125, 139] The mean DPs in (D) and

the inset mean DPs for each loading vector show that the SEI components diffract strongly compared to LPSCl, indicating the crystallinity of these components.

To better understand the spatial distribution of the SEI components and verify visual impressions, I conducted statistical analysis across seven independently collected datasets to investigate the average SEI domain size, the 'near-neighbour' distance between SEI components, and component cross-correlation, as shown in Figures 5.7 F and G. The average distances between SEI components, Li and LPSCl, along with their domain sizes, are shown in Figure 5.7 F. The average domain sizes for SEI species are larger than have been shown in previous reports, with some reaching a domain size approximately 100 nm^2. Li_3P domains on average are the largest (approx. 54 nm^2), while LiP, Li_2S and LiCl (approx. 22, 23, 34 nm^2, respectively).[44, 56, 157] The Li_3P domains are noteworthy as their high Li diffusivity is suggested to contribute to the continuous degradation of LSPCl and larger domains may contribute to longer diffusion pathways for SE breakdown.[231]

The relative distance between Li and the SEI components is very similar for Li_2S, LiCl, and Li_3P, with LiP located nearest to the Li domains. This contrasts with the Pearson correlation shown in Figure 5.7G, where LPSCl has the highest cross-correlations with the phosphide species. Notably, the cross-correlations across all samples are only weakly positive cross-correlated. The absence of strong positive correlations, particularly between the SE and SEI components, supports a successful isolation of the SEI layer, while the lack of strong negative correlations suggests the formation of a 3D multilayered SEI.[125, 154] A multilayer structure would average correlations along the imaging direction. The observed tendency toward positive correlations suggests complex interrelations between the SEI components, with the current sample state likely reflecting an incomplete or kinetically halted SE and Li degradation process.[135, 158, 231] Combined, the correlation and spatial separation of the SEI components align with the diffusion-controlled SEI growth mechanism currently suggested in Li-LPSCl systems, where Li and P migration drive the formation of complex SEI structures.

5.3.5 Comparison with LPSClBr

Solid electrolyte chemistry and microstructure, among other factors, are known to influence the structure of the SEI. To assess whether this approach can detect these influences, I imaged the SEI formed between Li metal and LPSClBr. LPSClBr is a high-entropy sulphide SE with a higher ionic conductivity than LPSCl that differs in composition and microstructure. Specifically, the LPSClBr used here has a particle size of approximately 1 μm, compared to 10 μm for the LPSCl. To form the SEI, Li was also plated at a current density of 0.1 mA cm^{-2} for 10 hours. Figures 5.8 A-G show the same NBED microscopy analysis as was shown for the LPSCl SEI. The SEI formed with LPSClBr exhibits two key differences. First, while both SEIs have a similar composition and show stratification, with phosphide domains slightly more likely to form closer to Li, suggesting a largely unchanged SEI growth mechanism, LiBr is detected as an additional SEI component. The detection is expected, as LiBr is both a minor native SE impurity and a decomposition product of the SE.[129] LiBr is located closer to the SE. Second, the SEI structure is much finer than that formed with LPSCl.

The difference in microstructure likely originates from SE particle size differences. The SEI formed with the large-grained LPSCl exhibits a granular structure, with domain sizes varying widely but generally larger. In contrast, the SEI formed with the fine-grained LPSClBr displays a finer, mosaic-like structure. The SEI domains exhibit far less variability in size, with an average domain size of less than 10 nm^2. This finer microstructure closely resembles that of SEIs observed in systems utilizing liquid electrolytes.[56, 61, 223] Accordingly, the LPSClBr SEI also contains a higher spatial density of smaller Li domains. Indicative of a larger number of Li plating sites and reduced current focusing compared to LPSCl. These microstructural differences may partially explain the reported increase in critical current density for the high-entropy LPSClBr compared to LPSCl.[129] Speculatively, a higher density of smaller Li nucleation sites leads to more homogeneous plating and, in principle, a more homogeneous SEI structure. While the smaller domain sizes could

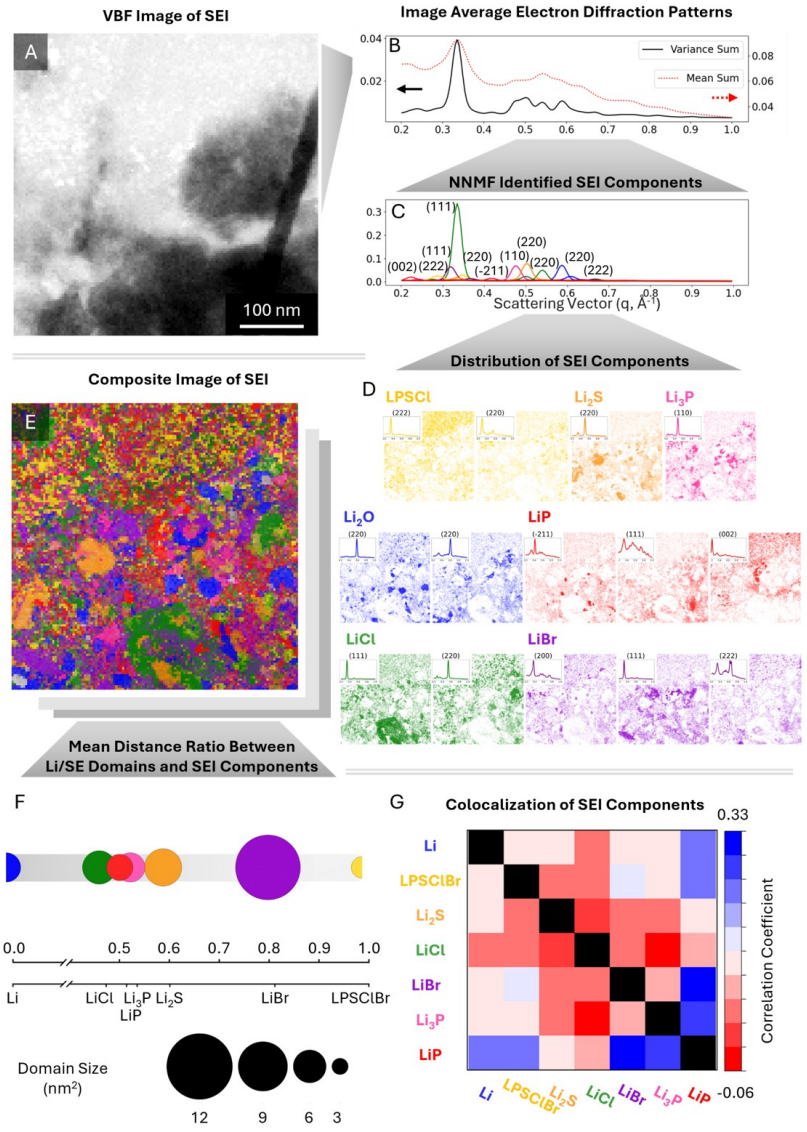


Figure 5.8: (A) Virtual BF image of the SSE-SEI-Li interface in a LPSClBr sample. (B) 1D mean and variance radial profiles (C) Individual loading vectors scaled to their intensity in the variance radial profile. (D) Individual component maps corresponding to each loading vector labelled with their plane orientation. (E) Compositional colour map containing all matched loading vectors. (F) Bubble plot showing the average distance of SEI components to Li (left) or LPSCl (right). The Bubble size represents the average domain size. (G) Correlation coefficients between the different components.

reduce the ability of Li to diffuse through the SEI due to a lack of continuous pathways, slowing or stopping its growth.[44, 135, 231]

Despite the differences in particle size, the trend in SEI structure across these two SSEs is similar. This suggests that the SEI growth mechanism has not changed significantly. The analysis shown here demonstrates the value of this technique

in characterising the SEI for ASSBs and expanding our understanding of the SEI with two promising sulphide SSEs.

5.4 Conclusion

Here, the full SSE-SEI-Li interface is mapped using low-dose 4D-STEM. The combination of sample preparation protocol and low-dose imaging allows imaging of the SEI in ASSBs at room-temperature. Initial results demonstrate a complex structure with intermixing of components and no clear layer. The location of LiCl in the SEI was noted for the first time, which had not been possible with XPS as it is indistinguishable from LPSCl.[125, 139, 158] The SEI particles observed with LPSCl are larger than have been observed with other electrolytes. The differential in conductivities of the different components may contribute to heterogeneous plating. The smaller SEI particle size observed with LPSClBr could help combat this effect, as the smaller particles could increase the homogeneity of the structure.

This analysis opens up many opportunities for further investigations of the SEI in ASSBs, including analysis of changes in the SEI with calendar and cycle life and correlation with electrochemical performance to better understand the structure-property relationship. Limitations which still need to be overcome include the difficulty in obtaining strong signal from the weakly-diffracting and sensitive battery materials, and characterisation of amorphous phases. Future studies could investigate burst-sampling techniques to lower dose requirements and the combination with electron pair density function microscopy to image amorphous phases.[**Liu2023iEDP2PDF/iMaterials**, 241, 242]

5.5 Experimental Details

5.5.1 Materials

Li_6PS_5Cl solid electrolyte, 10 μm particle size, was purchased from Ampcera (99.9%). The $Li_{5.5}PS_{4.5}Cl_{0.75}Br_{0.75}$ solid electrolyte, with an particle size of approximately 0.5 μm, was synthesized via a solid-state reaction.[129] TEM grids were purchased

from Agar Scientific (400 mesh Ni grids with lacey carbon). Current collectors were punched as 10 mm disks from Ni (Advent Research Materials, 99.95 %) and stainless steel (Goodfellow) sheets. The current collectors were washed with ethanol and acetone and left to dry in a vacuum oven at 60 degC overnight. Li metal foil (99.9%) was purchased from Alfa Aesar. Before use the oxide surface layer was mechanically removed and the Li foil calendared ($\approx 200\ \mu$m). Lastly, 10 mm disks were punched out of the Li and Ni foil. All operations were carried out and materials stored in an Ar glovebox (MBraun; H_2O <0.1 ppm, O_2 <0.1 ppm) unless stated otherwise.

5.5.2 Sample Preparation

See Chapter 4 for more detail.

ASSBs were assembled and cycled using an air-tight cycling rig, consisting of an outer steel casing and an interior PEEK tube housing a ASSB pellet. Pellets are 10 mm in diameter and 0.5 to 1 mm in height. The SSB is cycled at fixed pressure, applied by spring-loaded stainless steel pistons placed on either side of the SSB pellet. The SE powder, Li, and current collectors were prepared/assembled within the PEEK body, before these components were enclosed in the air-tight casing for electrochemical cycling. Assembly of the cells followed a three-step process. First, the SE powder was compacted at 50 MPa for 30 s using a hydrostatic press, then a TEM grid and Ni current collector were placed on one side of the SE and incorporated into the SE via densification at 500 MPa for 180 s. Finally, Li and a stainless steel current collector were added on the other side of the SE and pressed at approximately 50 MPa for 30 s. For single plating-step samples 100 g of SE powder was used, for more cycles 200 g. The resulting increase in SE layer thickness reduces the chance of early short-circuit occurrence. A lacey carbon-coated Ni TEM grid was used rather than Cu. Ni alloys less with Li, reacts less with the sulphide SE, and has superior mechanical properties which make it easier to extract the grid post Li plating.[135].

5.5.3 4D-Scanning Transmission Electron Microscopy

Samples were loaded into a JEOL Air-isolation Beryllium Transfer holder (EM-01380STBTH) and transferred into the TEM without air exposure. A JEOL ARM300CF microscope using a current of approximately 0.4 pA, measured with a Faraday cup (0.5-0.6 pA measured with 0.1-0.2 pA measured dark current), in nanobeam mode with a convergence angle of approximately 1 mrad, and accelerating voltage of 300 kV was used to collect diffraction pattern on a Merlin MediPix direct electron detector, with an active area of 28 mm^2 and 512 $\times$ 512 pixels (pixel size 55 μm^2). Images were recorded using a scanning nanobeam of 1 nm across a 256 x 256 scanning grid. The pixel dwell time was 600 μs, providing a sufficient signal-to-noise ratio for data collection, while avoiding radiation damage Figure 4.10. Overview HAADF images were initially acquired to locate regions of interest. Magnification was 20k with a dwell time of 10 μ s to limit deposited dose and radiation damage for these overview images. Zooming in was done 'blind' by highlighting an approximate area in the HAADF scan which corresponds to the area which would be imaged in the higher-magnification 4D-STEM scan.

5.5.4 Calibration

Diffraction pattern calibration was performed using a Au grid as a reference before each acquisition session. Calibration measurements were acquired after instrument alignment but prior to experiments. Calibration workflows published by Savitzky et al. were utilised to align, centre, check the ellipticity, and calibrate the data.[174, 243]

5.5.5 Electron Diffraction Image Analysis

Following beam alignment the acquired 2D diffraction patterns were azimuthally integrated, resulting in a 1D diffraction pattern per scanning point or pixel using scripts provided by ePSIC (`https://github.com/ePSIC-DLS/User-Notebooks`). The acquired diffraction images were analysed using non-negative matrix factorization.[239] The obtained loading vectors were assigned to materials by matching the

vector diffraction pattern to those of likely or previously reported SEI components and cross-confirmed by XPS.

Peak Matching Algorithm

SEI components by matching their Bragg peak positions to those of known or expected SEI components. The list of potential SEI components was limited to those previously reported for Li-LiPSCl systems and those identified in supplementary X-Ray Photoelectron Spectroscopy (XPS) measurements of the SEI (Figure S6). Crystallographic Information Files (CIFs) for these components were sourced from the Crystallographic Open Database (COD). The CIF file of LPSCl was used for LPSCl and LPSClBr, but with slightly different thresholds (90% for LPSCl vs 92% for LPSClBr) due to the higher noise level for LPSClBr, the ratio of thresholds for peak matching and spatial analysis was kept constant. For the physical component assignment, the most prominent or intense reflection in a loading vector was compared with the Bragg reflections of expected SEI components using diffraction pattern simulation software, here CrystalDiffract. A match was identified if the position deviation between the loading vector reflection and the simulated component reflection fell within a $+/-2.5\%$ position tolerance. In cases where multiple component reflections satisfied this criterion, secondary, less intense peaks were considered to refine the assignment. To account for signal-to-noise limitations and limit the number of reflections included in the matching process, reflection intensity thresholds were applied to both the loading vectors and reference pattern. The cutoff threshold for reference pattern is based on the relative intensity on secondary reflections (1/8) compared to the dominant reflection. A relative, rather than a flat cutoff threshold is preferable to account for material scattering differences. A flat threshold was set for the loading vectors, informed by higher order background loading vector contributions. Limits remove low prominence peaks from consideration, unlikely to be detected and readily captured at the given electron dose.

Spatial Separation Algorithm

The DBSCAN clustering algorithm was used to cluster the points associated with each component (`https://scikit-learn.org/stable/modules/generated/sklearn.cluster.DBSCAN.html`). The maximum neighbourhood separation distance (e) and number of samples (m) were modified to ensure representative clustering. The clusters were then converted to Polygons using a modification of a Concave Hull algorithm (`https://github.com/M-Lin-DM/Concave-Hulls`). The average centroid distance between the Polygons for a pair of components was calculated, as well as the distance between the the edges of the polygons if they do not overlap or the % of their area which overlaps if they do, using methods from Shapely (`https://github.com/shapely/`). The script is shown in Appendix A.2.

5.5.6 Virtual Electrode Plating - X-Ray Photoelectron Spectroscopy (VEP - XPS)

This was completed by Yi Liang.

Sample Preparation

The sample consists of a Cu current collector, a Li foil disk 4.7 mm in diameter, and a Li_6PS_5Cl pellet. The pellet was prepared by pressing approximately 30 mg of powder under 500 MPa for 5 minutes using a 5 mm die set. The layers were attached under 40 MPa and the resulting stack attached to an XPS sample holder using conductive carbon tape with the free SSE facing away from the sample holder surface. An air-free transfer vessel was used to transfer the sample from the glovebox into the XPS chamber.

Instrumentation and Data Acquisition

The VEP-XPS experiment was conducted using a PHI Versaprobe III XPS system with a monochromatic Al Kα X-rays source at 1486.6 eV. Experiments were performed under ultrahigh vacuum conditions (10^{-7}). The instrument's electron neutralizer was used to provide a Li migration driving force. The 5 mm diameter

electron beam provides a negative potential on the free SE sample surface facilitating the migration of Li^+ through the electrolyte pellet. On reaching the pellet surface the ions result in Li deposition, electrolyte decomposition and SEI formation. The electron beam was set to 30 μA, corresponding to a current density of approximately 0.15 mA cm^{-2}. The evolution of chemical information at the surface was monitored by alternating between Li plating and XPS measurements. A pass energy of 224 eV was used for survey scans and 55 eV for high-resolution core-level scans. The acquisition of an XPS spectra took 15 minutes.

Analysis

The XPS data was processed using CasaXPS software with the application of a Shirely-type background. XPS spectra were fitted using Gaussian–Lorentzian line shapes and calibrated based on Cl 2p 3/2 to 198.5 eV. The sample-average SEI composition was calculated via component specific peak integration of Li, P, S, and Cl signals.[244]

Focus on the science, not how to make the best battery!

— Ying Shirley Meng, Professor of Molecular Engineering at the University of Chicago and Chief Scientist at Argonne Collaborative Centre for Energy Storage Science

6 Conclusions and Future Work

Contents

6.1 Conclusions 133
6.2 Future Work 134

6.1 Conclusions

This thesis has highlighted the ability of electron microscopy to characterise key degradation mechanisms at the Li-SSE interface in ASSBs. First, Xe PFIB was used to analyse microstructural changes at this interface. It was shown that Li alloys are more stable during ion milling than Li metal, allowing them to be characterised at room temperature. This means that Li-Mg alloys (with their similar potential and mechanical properties) could be used as a proxy for Li for FIB characterisation by scientists without access to cryo-FIB. In addition, the changes in the microstructure of the common reference electrode, Li-In, were able to be characterised, improving understanding of its performance. Access to cryo-FIB then allowed for characterisation of the interface with a pure Li electrode. With a composite TSE the Li ingress into the SSE was shown to be round, differing from most reports in literature, potentially due to the higher ductility of the SSE

with a polymer binder. Finally, the difference in Li plating morphology through a C-Ag interlayer was shown to vary significantly with temperature, highlighting the importance of reporting battery testing under practical conditions. Throughout, the potential artifacts introduced during FIB-SEM investigations were noted, including sample preparation damage and charging artifacts which can appear as cracking or interphase formation, leading to incorrect attribution.

The second part of this thesis described a workflow for the preparation and analysis of the Li-SEI-SSE interface in ASSBs. As it was not possible to image this layer with FIB-SEM, a technique was developed to reliably produce samples of this full interface. This was done by incorporating a TEM grid into an ASSB battery in a multi-step densification process so that it can be removed after electroplating Li. These were then thinned to electron transparency with cryo-FIB and imaged with low-dose room-temperature 4D-STEM, avoiding complications due to use of cryo-transfer into the TEM. Spatio-compositional maps of the interphase were then generated from the 4D-STEM data. A layered structure was identified, as expected, but the crystallite size observed was established to be on the order of 100 nm^2 for most SEI components. This is significantly larger than has been reported for liquid electrolytes or other SSEs, impacting modelling of the properties of this layer. Statistical analysis of the relationship between different components confirmed a layered structure in the SEI with P-species further from the Li and S-species closer. LiCl was also revealed to form closer to Li. The crystallite size in LPSCl was observed to be larger than has been seen with other electrolytes. Finally, a comparison was made between the statistical spatial-compositional analysis of LPSCl and LPSClBr, demonstrating that LPSClBr has a much smaller crystallite size, but the overall layered structure, while less obvious, is still present.

6.2 Future Work

The exact mechanism of Li dendritic nucleation and growth has yet to be established. To complement the work already done with X-Ray techniques, higher resolution 3D Xe PFIB would be able to identify early Li growth in the nucleation process.

Temporal resolution would also be important for these studies. This is more difficult with PFIB than X-Ray tomography as PFIB is destructive, but the high milling rate of Xe will makes the work of comparing multiple samples at different states of Li plating or stripping feasible. Many challenges remain to provide representative samples for this work, including development of in-situ techniques and gentler cell disassembly to minimise artifact generation. As the SSE interface becomes increasing complex, a clear understanding of the relationship between these developments and the Li deposition process is key. The combination of high resolution and minimal artifact generation with cryo-FIB-SEM is uniquely suited to this challenge. In particular, the impact on the morphology of deposited Li with different interlayer materials or morphologies and composite SSEs incorporating polymers have only just begun to be studied.

The technique described in Chapters 4 and 5 of this thesis could be utilised to significantly improve the understanding of the SEI in ASSBs. The technique is applicable to different ASSB chemistries, so a first development, as shown here, was to investigate different SSEs. It could also be expanded further to oxide or halide electrolytes to map the SEI they develop against Li metal. Comparison across several SSE chemistries under the same conditions could provide insight into how to optimise chemistries to minimise degradation due to SEI formation, for example by identifying SEI compounds which lead to growth suppression. As mentioned above, the interfaces in ASSBs are becoming more complex, and the incorporation of interlayers or polymers into the SSE may also have an effect on the SEI which forms. This is another area where this technique could be applied. In particular, to identify if an interlayer may succeed in preventing further SEI growth and electrolyte decomposition.

As well as varying the materials involved, the growth of the SEI over time or cycles can be observed. Investigation of a series of samples prepared over a range of time scales would shine a light on the temporal development of the SEI. This could also be done by preparing a sample quickly and placing it straight into the TEM, then investigating changes in the SEI over time within the isolated TEM chamber.

This could be correlated with electrochemical (EIS) measurements to investigate the structure - property relationship of the SEI as it forms over time. In addition to simple calendar time, the evolution of the SEI over a number of cycles could be investigated. This would involve preparing samples which have undergone different numbers of plate - strip cycles, or even have had different capacities of Li plated or stripped. There is a potential for the structure or chemistry of the SEI to change with cycling, which may stabilize the growth or further SEI or lead to excessive degradation. Ideally, this could be done using some type of in-situ cell in the TEM so changes in the SEI could be investigated over time in the same sample.

Further work to optimise the technique would provide additional information about the SEI in the cases described above. First, optimising the dose and the dwell time during sampling could lead to higher resolution in the measurement, both in real and reciprocal space. This would enable greater detail in the SEI structural analysis, and more robust matching of components in the SEI. This could potentially also lead to investigations into the strain across the SEI, and whether this has any effect on SEI structural development and Li growth. Finally, burst imaging and electron pair distribution functions could be used to increase the resolution without damaging the sample and learn more about amorphous portions of the SEI, respectively.

Appendices

A

4D-STEM Analysis code

Contents

A.1 1D Spectrum Matching Algorithm 140
A.2 Spatial Separation Analysis Algorithm 148

A.1 1D Spectrum Matching Algorithm

Written with help from ChatGPT.[245]

```
def load_crystal_data(file_path, sheet_name):
    """Loads crystal data from an Excel sheet."""
    return pd.read_excel(file_path, sheet_name=sheet_name)



def select_candidates(peaks, prominences, crystals,
big_peak, mid_peak, noise_peak, big_limit, mid_limit,
small_limit, error_limit):

    """Selects candidate matches for the primary peak
    based on error tolerance and intensity limits."""
    candidates = {}
    prominence_value = prominences[0]
    #print('prominence', prominences[0])

    # Set initial intensity threshold based on prominence
    include = crystals['Intensity'] > ( big_limit if
    prominence_value > big_peak else mid_limit if
    prominence_value > mid_peak else small_limit )

    # Function to populate candidates
    def add_candidate(row, error, mark=False,mark2=False):
        """Helper to add a candidate with optional marking."""
        if mark2:
            intensity_value = f"{row['Intensity']}**"
        elif mark:
            intensity_value = f"{row['Intensity']}*"
```

```
        else:
            intensity_value = f"{row['Intensity']}"

        return {
            'Material': row['Material'],
            'Plane': row['Plane'],
            '1/d (1/A)': row['1/d (1/A)'],
            'Intensity': intensity_value,
            'Error': error
        }

    # Main search for candidates based on error tolerance and
    # intensity threshold
    mark = False
    mark2 = False
    if pd.isna(prominences[0]) or (prominences[0] < noise_peak):
        candidates[1] = {
            'Material': 'Noise',
            'Plane': 'N/A',
            '1/d (1/A)': 'N/A',
            'Intensity': 'N/A',
            'Error': 'N/A',
            'Confidence': 'High'
        }

    if not candidates:
        for j, crystal_row in crystals[include].iterrows():
            error = abs(peaks[0] - crystal_row['1/d (1/A)']) / ...
            peaks[0] * 100
            if error < error_limit:
```

```
            candidates[j] = add_candidate(crystal_row, error)

    # If no candidates were found, try again with the lower
    # threshold (mid_limit)
    if not candidates:
        include = crystals['Intensity'] > mid_limit
        for j, crystal_row in crystals[include].iterrows():
            error = abs(peaks[0] - crystal_row['1/d (1/A)']) / ...
            peaks[0] * 100
            if error < error_limit:
                candidates[j] = add_candidate(crystal_row, ...
                error, mark=True)  # Mark these entries with "*"

    # If no candidates were found, try again with the lower
    # threshold (small_limit)
    if not candidates:
        include = crystals['Intensity'] > small_limit
        for j, crystal_row in crystals[include].iterrows():
            error = abs(peaks[0] - crystal_row['1/d (1/A)']) / ...
            peaks[0] * 100
            if error < error_limit:
                if mark:
                    candidates[j] = add_candidate(crystal_row, ...
                    error, mark2=True)  # Mark these entries with "*"
                else:
                    candidates[j] = add_candidate(crystal_row,...
                    error, mark=True)
```

```
    # If peaks[0] is NaN or still no candidates, label as noise
    if not candidates:
        candidates[1] = {
            'Material': 'No Match',
            'Plane': 'N/A',
            '1/d (1/A)': 'N/A',
            'Intensity': 'N/A',
            'Error': 'N/A',
            'Confidence': 'N/A'
        }

    # Return DataFrame sorted by Error
    #print(candidates)
    return pd.DataFrame.from_dict(candidates, orient='index')...
    .sort_values(by='Error')

def assign_confidence(primary_candidates, error_difference,...
peaks, prominence_series, confidence_metric='mean'):
    """
    Assigns confidence based on primary peak and secondary
    peaks matching, using a threshold.

    Parameters:
    - confidence_metric: Defines the threshold type ('mean',
    'median', or percentile as int).
    """

    if primary_candidates.empty:
        return {'Material': 'No Match', 'Plane': 'N/A', ...
        'Confidence': 'N/A'}
```

```
    if (primary_candidates.isin(['Noise']).any().any()):
        return {**primary_candidates.iloc[0]}

    # High confidence if there's a single clear match
    if len(primary_candidates) == 1 or \
       abs(primary_candidates.iloc[1]['Error'] - ...
       primary_candidates.iloc[0]['Error']) > ...
       error_difference:
        return {**primary_candidates.iloc[0],...
        'Confidence': 'High'}

    # Check secondary peaks if multiple similar
    # matches exist
    if len(peaks) > 1:
        return match_with_secondary_peaks(...
        primary_candidates, peaks[1:], prominence_series[1:],..
        confidence_metric)

    # Default to Low confidence for close candidates if
    #no secondary peak available
    return {**primary_candidates.iloc[0], 'Confidence': 'Low'}


def match_with_secondary_peaks(primary_candidates,...
secondary_peaks, prominences, confidence_metric):
    """Matches secondary peaks to reinforce the confidence
    in primary candidates with weighted scoring."""

    # Filter primary candidates within the error difference...
```

```
threshold
min_error = primary_candidates['Error'].min()
filtered_candidates = primary_candidates...
[primary_candidates['Error'] <= min_error + error_difference]
# keep materials within error difference of lowest
filtered_candidates = filtered_candidates.sort_values(by='Error')...
.drop_duplicates(subset='Material', keep='first')
#remove any material duplicates, keep lowest error

#print('Filtered Candidates:', filtered_candidates)
include = (crystals['Intensity'] > small_limit) & ...
(crystals['Material'].isin(filtered_candidates['Material']))

# Initialize weighted scores for each candidate material
candidates_weighted_scores = {candidate['Material']: ...
0 for candidate in filtered_candidates.to_dict('records')}

# Iterate over each secondary peak and its corresponding prominence
for peak, prominence in zip(secondary_peaks, prominences):
    #print('peak',peak,'prominence',prominence)
    for i, row in crystals[include].iterrows():
        # Calculate error for each candidate relative
        # to the secondary peak
        error = abs(peak - row['1/d (1/A)']) / peak * 100
        if error < error_limit:  # Only consider candidates
        #within error tolerance
            # Update weighted score using prominence and
            # inverted error as weights
            candidates_weighted_scores[row['Material']] += ...
            prominence * (error_limit - error)
```

```
    #print(candidates_weighted_scores)
    # Determine the dynamic confidence threshold based on the
    # specified confidence metric
    if confidence_metric == 'mean':
        threshold = prominences.mean()
    elif confidence_metric == 'median':
        threshold = np.median(prominences)
    elif isinstance(confidence_metric, int):
        # Percentile-based threshold
        threshold = np.percentile(prominences, confidence_metric)
    else:
        raise ValueError("Invalid confidence_metric. ...
        Use 'mean', 'median', or an integer for percentile.")
    #print('weighted_scores', candidates_weighted_scores)
    # Identify the candidate with the highest weighted score
    best_material = max(candidates_weighted_scores, ...
    key=candidates_weighted_scores.get)
    #print('best_material',best_material)
    best_match = filtered_candidates[filtered_candidates...
    ['Material'] == best_material].iloc[0]

    # Set confidence based on whether the weighted score...
    meets the dynamic threshold
    max_score = candidates_weighted_scores[best_material]
    confidence = 'Medium' if max_score > threshold else 'Low'

    return {**best_match, 'Confidence': confidence}


# Main loop - example usage
```

```
# Things that could still be added - Li and Li2O co-location
confidence_metric = 'median'  # or set to 'mean' or a
# percentile, e.g., 75 for 75th percentile

file_path = base_dir+'/Crystal Planes.xlsx'
sheet_name = arg
crystals = load_crystal_data(file_path, sheet_name)
maximum = float(prominence_mean_peaks[0].max())

big_peak = maximum/8 # sets the prominence limit for a
#peak to be treated as 'big'
mid_peak = maximum/16
noise_peak = median_first_peak/10 # below classed as noise
print('big_peak',big_peak,'mid_peak',mid_peak,...
'noise_peak',noise_peak)
big_limit = crystals['Intensity'].max()/4  # sets the ...
# minimum intensity of structure factor for a peak
#considered 'big'
mid_limit = crystals['Intensity'].max()/8 # in-between...
#if nothing fits big
small_limit = crystals['Intensity'].max()/100
# sets the minimum intensity of structure factor ...
#for all peaks
print('big_limit',big_limit,'mid_limit',mid_limit,...
'small_limit',small_limit)
error_limit = 5 # maximum error (%) to be considered...
as a potentical peak
error_difference = 2.5 # now made relative, window of...
#error to consider if there are multiple peaks...
#(lowest error + this value = max error)
```

```
matching = {}


for i, peaks in ordered_mean_peaks.iterrows():
    #print('LV',i)
    prominences = prominence_mean_peaks.loc[i]
    #.dropna().values
    # Get prominence values for current peaks
    #print(i,prominences)
    # Select candidates for the primary peak
    primary_candidates = select_candidates(...
    peaks, prominences, crystals, big_peak, mid_peak,...
    noise_peak, big_limit, mid_limit, small_limit, error_limit)
    #print(i,primary_candidates)
    # Assign confidence based on primary and secondary peak
    #matching with prominence weights and confidence threshold
    match = assign_confidence(primary_candidates, ...
    error_difference, peaks, prominences, confidence_metric)


    matching[i] = match


matching_df = pd.DataFrame.from_dict(matching, orient='index')
print(matching_df)
#matching_df[['Material','Plane']]
```

A.2 Spatial Separation Analysis Algorithm

Based on code written by Jinseok Ryu. Edited with help from ChatGPT.[245]

```
try:
    from shapely.geometry import Point
    from shapely.geometry import LineString
```

```
    from shapely.geometry import Polygon


    class ConcaveHull(object):
        '''
        original code: https://github.com/M-Lin-DM/Concave-Hulls
        modified by J. Ryu
        '''
        def __init__(self, points, k, distance_threshold=1e6):
            if isinstance(points, np.core.ndarray):
                self.data_set = points
            elif isinstance(points, list):
                self.data_set = np.array(points)
            else:
                raise ValueError('Please provide an [N,2]...
                numpy array or a list of lists.')

            # Clean up duplicates
            self.data_set = np.unique(self.data_set, axis=0)

# ADDED by YAC
            # Apply distance filtering to remove isolated points
            self.distance_threshold = distance_threshold
            # Distance threshold for isolation check
            self.data_set = self.remove_isolated_points(...
            self.data_set, distance_threshold)
#
#
#             # ADDED by YAC
```

```
            # Create the initial index
            self.indices = np.ones(self.data_set.shape[0],..
            dtype=bool)  # bool of a column of all 1's

            self.k = k

        @staticmethod
        def dist_pt_to_group(a, b):  # a is a (n,2) , b is (1,2) arrays
            d = np.sqrt(np.sum(np.square(np.subtract(a, b)), axis=1))
            return d

        @staticmethod
        def get_lowest_latitude_index(points):
            indices = np.argsort(points[:, 1])
            return indices[0]

        @staticmethod
        def norm_array(v):
        # normalize row vectors in an array.
            norms = np.array(np.sqrt(np.sum...
            (np.square(v), axis=1)), ndmin=2).transpose()
            return np.divide(v, norms)

        @staticmethod
        def norm(v):
        # normalize a single vector
            norms = np.array(np.sqrt(np.sum(np.square(v))))
            return v / norms

#ADDED by YAC - removes isolated points
```

```
        def remove_isolated_points(self, points, distance_threshold):
            """
            Removes points that do not have at least one other
            point within the given distance threshold.
            :param points: numpy array of points
            :param distance_threshold: radial distance within
            which a point should have at least one neighbor
            :return: numpy array of filtered points
            """
            valid_points = []
            for i, point in enumerate(points):
                distances = self.dist_pt_to_group(points, point)
                # Check if there is any other point within
                #the distance threshold
                if np.sum((distances < distance_threshold) & ...
                (distances > 0)) > 0:
                    valid_points.append(point)
            return np.array(valid_points)
    # ADDED by YAC with help from ChatGPT


        def get_k_nearest(self, ix, k):
            """
            Calculates the k nearest point indices to the
            point indexed by ix
            :param ix: Index of the starting point
            :param k: Number of neighbors to consider
            :return: Array of indices into the data set array
            """
            ixs = self.indices
            # base_indices is list of linear indicies that are
```

```
        #TRUE, ie part of dataset
        base_indices = np.arange(len(ixs))[ixs]
        distances = self.dist_pt_to_group(self....
        data_set[ixs, :], self.data_set[ix, :])
        sorted_indices = np.argsort(distances)

        kk = min(k, len(sorted_indices))
        k_nearest = sorted_indices[range(kk)]
        return base_indices[k_nearest]

    def clockwise_angles(self, last, ix, ixs, first):
    # last needs to be the index of the previous current point
        if first == 1:
            last_norm = np.array([-1, 0], ndmin=2)
        elif first == 0:
            last_norm = self.norm(np.subtract(...
            self.data_set[last, :], self.data_set[ix,:]))
            # normalized vector pointing towards previous point
        ixs_norm = self.norm_array(np.subtract(...
        self.data_set[ixs, :], self.data_set[ix,:]))
        # normalized row vectors pointing to set of k nearest ns
        ang = np.zeros((ixs.shape[0], 1))
        for j in range(ixs.shape[0]):
            theta = np.arccos(np.clip(np.dot(last_norm,...
            ixs_norm[j, :]), -1.0, 1.0))
            # slighlty edited by Yvonne to add the clip
            # to avoid arccos errors
            # ang[j,0] = theta
            z_comp = np.cross(last_norm, ixs_norm[j, :])
            # ang[j,2] = z
```

```
            if z_comp <= 0:
                ang[j, 0] = theta
            elif z_comp > 0:
                ang[j, 0] = 2 * np.pi - theta
        return np.squeeze(ang)

    def recurse_calculate(self):
        """
        Calculates the concave hull using the next value
        for k while reusing the distances dictionary
        :return: Concave hull
        """
        recurse = ConcaveHull(self.data_set, self.k + 1)
        if recurse.k >= self.data_set.shape[0]:
            print(" max k reached, at k={0}".format(recurse.k))
            return None
        # print("k={0}".format(recurse.k))
        return recurse.calculate()

    def calculate(self):
        """
        Calculates the convex hull of the data set as an
        array of points
        :return: Array of points (N, 2) with the
        concave hull of the data set
        """
        if self.data_set.shape[0] < 3:
            return None

        if self.data_set.shape[0] == 3:
```

```
    return self.data_set

# Make sure that k neighbors can be found
kk = min(self.k, self.data_set.shape[0])

first_point = self.get_lowest_latitude_index(...
self.data_set)
current_point = first_point
# last_point = current_point

# Note that hull and test_hull are matrices (N, 2)
hull = np.reshape(np.array(...
self.data_set[first_point, :]), (1, 2))
test_hull = hull

# Remove the first point
self.indices[first_point] = False

step = 2
stop = 2 + kk

while ((current_point != first_point) or ...
(step == 2)) and len(self.indices[self.indices]) > 0:
# last condition counts number of ones, points in dataset
    if step == stop:
        self.indices[first_point] = True
    # notice how get_k_nearest doesnt take the
    #data set directly as an arg, as it is implicit
    #that it takes self as an imput because we are
    #inside a class:
```

```
knn = self.get_k_nearest(current_point, kk)
# knn = [3,6,2] or [0,2,7] etc indicies into
#the full dataset (with no points removed)

if step == 2:
    angles = self.clockwise_angles(1, current_point,...
    knn, 1)
else:
    # Calculates the headings between
    #first_point and the knn points
    # Returns angles in the same indexing
    #sequence as in knn
    angles = self.clockwise_angles(last_point,..
    current_point, knn, 0)

# Calculate the candidate indexes
#(largest angles first).
#candidates =[0,1,2]  or [2,1,0] etc if kk=3
candidates = np.argsort(-angles)

i = 0
invalid_hull = True

while invalid_hull and i < len(candidates):
    candidate = candidates[i]

    # Create a test hull to check if there
    # are any self-intersections
    next_point = np.reshape(self. ...
    data_set[knn[candidate], :], (1, 2))
```

```
            test_hull = np.append(hull, next_point,...
            axis=0)

            line = LineString(test_hull)
            invalid_hull = not line.is_simple
            # invalid_hull will remain True for
            #every candidate which creates a line
            #that intersects the hull. as soon as
            #the hull doesnt self intersect, it
            #will become false and the loop will
            #terminate
            i += 1

        if invalid_hull:
            return self.recurse_calculate()

        last_point = current_point
        # record last point for clockwise angles
        current_point = knn[candidate]
        # candidate = 0, 1, or 2 if kk=3
        hull = test_hull

        self.indices[current_point] = False
        # we remove the newly found current point
        #from the "mask" indicies so that it wont
        #be passed to get_k_nearest (within the
        #implicit input, self)
        step += 1

    poly = Polygon(hull)
```

```
            count = 0
            total = self.data_set.shape[0]
            for ix in range(total):
                pt = Point(self.data_set[ix, :])
                if poly.intersects(pt) or pt.within(poly):
                    count += 1
                else:
                    continue
                    # print("point not in polygon")

            if count == total:
                return hull
            else:
                return self.recurse_calculate()

except:
    print('shapely is needed for advanced analysis')

########################################
# This returns the original threshold image and the clustered
# version

import numpy as np
import matplotlib.pyplot as plt
from sklearn.cluster import DBSCAN
plt.close('all')

'''
DBSCAN (Density-Based Spatial Clustering of Applications with
```

```
Noise)
https://scikit-learn.org/stable/modules/generated/sklearn.cluster
.DBSCAN.html

e
The maximum distance between two samples for one to be considered
as in the neighborhood of the other.
This is not a maximum bound on the distances of points within
a cluster.
This is the most important DBSCAN parameter to choose appropriately
for your data set and distance function.

m
The number of samples (or total weight) in a neighborhood for
a point to be considered as a core point.
This includes the point itself.
If min_samples is set to a higher value, DBSCAN will find denser
clusters, whereas if it is set to a lower value, the found clusters
will be more sparse.
'''

e = 3.4
m = 9
#Sparse clusters seem to mess up the ConcaveHull function

clustered_split = []
binary_split = []
save = True

for comp in range(len(comp_maps)):
```

```
clustered_comp = []
binary_comp = []
for i in range(len(run_analysis.subfolders)):
    clustered_sub = []
    binary_sub = []
    num_img = len(run_analysis.radial_var_split[i])
    for j in range(num_img):
        if np.all(comp_maps[comp]==0):
            print(component[comp]+' not in sample,
            skipped for clustering.')
            continue
        db = DBSCAN(eps=e, min_samples=m)
        binary_map = comp_maps[comp]
        sel_coor = np.nonzero(binary_map)
        X = np.stack((sel_coor[0], sel_coor[1]), axis=1)
        db.fit(X)
        label = db.labels_
        # print(label)
        binary_sub.append(binary_map)
        clustered = np.zeros_like(binary_map)
        clustered[X[:, 0], X[:, 1]] = label+1
        clustered_sub.append(clustered)

        fig, ax = plt.subplots(1, 2, figsize=(12, 6))
        ax[0].imshow(binary_map, cmap='gray')
        ax[0].set_xticks([])
        ax[0].set_yticks([])
        ax[1].imshow(clustered, cmap=cluster_color)
        ax[1].set_xticks([])
        ax[1].set_yticks([])
```

```
            fig.suptitle('before - after '+component[comp]+'...
            -- e = '+str(e)+' m = '+str(m) )
            plt.show()
            if save:
                plt.savefig(path + sample  + data_key+'_Before-After...
                Clustering for '+component[comp]+' %d with e = %d, ...
                m = %d.png'%(lv+1,e,m)) #+ thresh

        binary_comp.append(binary_sub)
        clustered_comp.append(clustered_sub)
    binary_split.append(binary_comp)
    clustered_split.append(clustered_comp)

    # returns the centroid and boundaries of the clusters for each lv
# optional - will return mean and max dp but this requires
#a lot of memory
# biggest problem with hull seems to come from sparse points,
# going to reintroduce the distance thing
# using a function based on shapely
plt.close('all')
dt = 2
save = True
dd_dp = False #cuts out the parts which use the big dataset
#for running locally

centroid_split = []
boundary_split = []
comp_label = []
for i in range(len(run_analysis.subfolders)):
    num_img = len(run_analysis.radial_var_split[i])
```

```
    centroid_sub = []
    boundary_sub = []

    for j in range(num_img):
        if dd_dp:
            if run_analysis.new_process_flag:
                dataset = hs.load(run_analysis.loaded_data_path...
                [i][j][:-18]+'corrected_scaled.hspy')
            else:
                cali = py4DSTEM.read(run_analysis.loaded_data_path...
                [i][j][:-13]+"braggdisks_cali.h5")
                dataset = py4DSTEM.read(run_analysis.loaded_data_path...
                [i][j][:-13]+"prepared_data.h5")
                dataset = py4DSTEM.DataCube(dataset.data)
                #dataset = dataset.filter_hot_pixels...
                (thresh=0.1, return_mask=False)
                dataset.calibration = cali.calibration
                dataset.calibrate()

            save_path = os.path.dirname(run_analysis.loaded_data_path...
            [i][j]) # able to change the base directory for saving
            print("save directory: ", save_path)
            data_name = os.path.basename(run_analysis.loaded_data_path...
            [i][j]).split("_")
            data_name = data_name[0]+'_'+data_name[1]
            print("save prefix: ", data_name)

        centroid_comp = []
        boundary_comp = []
        for comp in range(len(comp_maps)):
```

```
if np.all(comp_maps[comp]==0):
    print(component[comp]+' not in sample, skipped.')
    continue
comp_label.append(component[comp])
# print(lv, i, j)
centroid_label = []
boundary_label = []
label_cluster = clustered_split[comp][i][j]
label_list = np.unique(label_cluster)
# print(label_list)

fig, ax = plt.subplots(1, 1, figsize=(6, 6))
ax.imshow(label_cluster, cmap=cluster_color)

for l in label_list[1:]:
    sel_coor = np.where(label_cluster == l)
    xy = np.stack((sel_coor[0], sel_coor[1]), axis=1)

    obj = ConcaveHull(xy, 2,distance_threshold = dt)
    hull = obj.calculate() # boundary pixel positions
    if hull is None:
        print(component[comp]+' - cluster %d did not...
        calculate hull' %l)
        #com_x, com_y = np.mean(sel_coor[1]),...
        np.mean(sel_coor[0])
        centroid_label.append([None, None])
        boundary_label.append(None)
        continue

    com_x, com_y = np.mean(sel_coor[1]),...
```

```
            np.mean(sel_coor[0])
            ax.scatter(com_x, com_y, s=15, c='k', marker='*')
            ax.plot(hull[:, 1], hull[:, 0], 'gray')
            ax.text(com_x, com_y, "%d"%(l), fontsize = 15)
            ax.set_xticks([])
            ax.set_yticks([])

            centroid_label.append([com_y, com_x])
            boundary_label.append(hull)
        if save:
            plt.savefig(path + sample  + data_key+...
            '_Cluster_Bounds_ '+component[comp]+' %d ...
            e=%d,m=%d,dt=%d.png'%(lv+1,e,m,dt)) #+ thresh


            if dd_dp:

                fig_dp, ax_dp = plt.subplots(1, 2, figsize=(10, 5))
                mean_dp = np.sum(dataset.data[sel_coor], axis=0)
                max_dp = np.max(dataset.data[sel_coor], axis=0)
                if save:
                    mean_dp = hs.signals.Signal2D(mean_dp)
                    mean_dp.axes_manager[0].scale = ..
                    run_analysis.radial_var_split[i][j]....
                    axes_manager[-1].scale
                    mean_dp.axes_manager[1].scale = ...
                    run_analysis.radial_var_split[i][j]...
                    axes_manager[-1].scale
                    mean_dp.save(save_path+'/'+data_name+"...
                    _mean_diffraction_pattern_%d_lv_%02d_...
```

```
        cluster.hspy"%(lv+1, l), overwrite=True)
        if also_tiff:
            tifffile.imwrite(save_path+'/...
            '+data_name+"_mean_diffraction_pattern_%02d_
            lv_%02d_cluster.tif"%(lv+1, l), mean_dp.data)

        max_dp = hs.signals.Signal2D(max_dp)
        max_dp.axes_manager[0].scale = run_analysis....
        radial_var_split[i][j].axes_manager[-1].scale
        max_dp.axes_manager[1].scale = run_analysis....
        radial_var_split[i][j].axes_manager[-1].scale
        max_dp.save(save_path+'/'+data_name+"...
        _max_diffraction_pattern_%d_lv_%02d_...
        cluster.hspy"%(lv+1, l), overwrite=True)
        if also_tiff:
            tifffile.imwrite(save_path+'/...
            '+data_name+"_max_diffraction_pattern...
            _%02d_lv_%02d_cluster.tif"...
            %(lv+1, l), max_dp.data)

mean_dp[np.where(mean_dp<=0)] = 1.0
max_dp[np.where(max_dp<=0)] = 1.0
ax_dp[0].imshow(np.log(mean_dp).clip(min=0),...
cmap='gray')
ax_dp[1].imshow(np.log(max_dp).clip(min=0),...
cmap='gray')
fig_dp.suptitle(run_analysis.subfolders[i]+" ...
- "+os.path.basename(run_analysis.loaded_data_path...
[i][j])[:15]+'\n%02d lv %02d cluster'%(lv+1, l))
```

```
            plt.show()
            centroid_comp.append(centroid_label)
            boundary_comp.append(boundary_label)
        centroid_sub.append(centroid_comp)
        boundary_sub.append(boundary_comp)
    centroid_split.append(centroid_sub)
    boundary_split.append(boundary_sub)

# Put all the Polygons for one loading vector into one MultiPolygon..
#object and contain that in a list
#unary_union allows you to do them all at once from a list, but seemed...
#to create one overall Polygon not a MultiPolygon
from shapely.geometry import Polygon, MultiPolygon
from shapely.ops import unary_union
#from shapely.ops import intersection
#comp_colors = ['deepskyblue', 'blue', 'green', 'deeppink', 'red',...
'xkcd:deep red'] # currently this needs to be updated manually...
#could add a little loop to do this for me
#'darkviolet','gold', 'darkorange',
plt.close('all')
comp_multipolys = []
comp_av_centroid = []
comp_multipolys_sep = []
fig_tot,ax_tot = plt.subplots(1)
for comp in range(len(boundary_split[0][0])):
    # if np.all(comp_maps[comp]==0):
    #     print(component[comp]+' not in sample, skipped.')
    #     continue
    fig,ax = plt.subplots(1)
    try:
```

```
        x = boundary_split[0][0][comp][0][0][0]
        y  = boundary_split[0][0][comp][0][0][1]
    except:
        continue
    multipoly = Polygon([(x, y),(x, y),(x, y),(x, y)]) # create 1x1
    #polygon to start off which should be within the first polygon/
    #shouldn't affect the result as it will be incorporated into the
    #first polygon
    poly_list = []
    centroid_list_x = []
    centroid_list_y = []
    for c in range(len(boundary_split[0][0][comp])):
        if boundary_split[0][0][comp][c] is None:
            continue

        ax.fill(boundary_split[0][0][comp][c][:, 1], -boundary_split...
        [0][0][comp][c][:, 0],
                            facecolor=comp_colors[comp],
                            edgecolor=comp_colors[comp], linewidth=3,...
                            alpha=0.5)
        ax_tot.fill(boundary_split[0][0][comp][c][:, 1], -boundary_split...
        [0][0][comp][c][:, 0],
                            facecolor=comp_colors[comp],
                            edgecolor=comp_colors[comp], linewidth=3,...
                            alpha=0.5)
        #ax.set_title(comp_label[comp])
        ax.set_xticks([])
        ax.set_yticks([])
        ax.set_xlim(-1,127)
        ax.set_ylim(-127,2)
```

```
        #ax_tot.set_title(subfolders[0]+' '+data_key)
        ax_tot.set_xticks([])
        ax_tot.set_yticks([])
        ax_tot.set_xlim(-1,127)
        ax_tot.set_ylim(-127,2)
        #plt.axis('scaled')

        poly = Polygon(boundary_split[0][0][comp][c])
        try:
            area51 = (poly.intersection(poly)).area
        except shapely.errors.GEOSException:
            print(f"Intersection error between polygons {i} and {j}....
            Skipping these polygons.")
            continue
        poly_list.append(poly)

        centroid_x = centroid_split[0][0][comp][c][0]
        centroid_y = centroid_split[0][0][comp][c][1]
        centroid_list_x.append(centroid_x)
        centroid_list_y.append(centroid_y)

    comp_multipolys_sep.append(poly_list)

    multipoly = MultiPolygon(poly_list) if len(poly_list) > 1...
    else poly_list[0]
        # multipoly = Polygon(boundary_split[0][0][lv][c])
        # multipoly =  multipoly.union(poly)
    comp_multipolys.append(multipoly)
```

```
    comp_av_centroid.append([np.mean(centroid_list_x),np.mean...
    (centroid_list_y)])
    if save:
        fig.savefig(path + sample  + data_key+'_Clusters_...
        '+comp_label[comp]+'.png') #+ thresh
if save:
    fig_tot.savefig(path + sample  + data_key+'_All_Clusters.png')
```

References

1. Dunn, B. *et al.* Electrical Energy Storage for the Grid: A Battery of Choices System power ratings, module size. *Science* **334,** 928–935 (2011).
2. Thackeray, M. M. *et al.* Electrical energy storage for transportation - Approaching the limits of, and going beyond, lithium-ion batteries. *Energy and Environmental Science* **5,** 7854–7863 (2012).
3. Zhu, Z. *et al.* Rechargeable Batteries for Grid Scale Energy Storage. *Chemical Reviews* **122,** 16610–16751 (2022).
4. Bruce, P. G. *et al.* Li-O2 and Li-S batteries with high energy storage. *Nature Materials* **11,** 19–29 (2012).
5. Newman, J. *et al. Electrochemical Systems* 3rd (John Wiley & Sons, 2004).
6. Bloom, I. *et al.* An accelerated calendar and cycle life study of Li-ion cells. *Journal of Power Sources* **101,** 238–247 (2001).
7. Xiao, J. *et al.* Understanding and applying coulombic efficiency in lithium metal batteries. *Nature Energy* **5,** 561–568 (2020).
8. Chen, L. *et al.* Toward wide-temperature electrolyte for lithium–ion batteries. *Battery Energy* **1** (2022).
9. Ouyang, D. *et al.* Influence of Current Rate on the Degradation Behavior of Lithium-Ion Battery under Overcharge Condition. *Journal of The Electrochemical Society* **166,** A2697–A2706 (2019).
10. Lin, Z. *et al.* Aligning academia and industry for unified battery performance metrics. *Nature Communications* **9** (2018).
11. Auston, D. *et al.* in *Collabra* 1 (University of California Press, 2016).
12. Dahn, J. R. *et al.* Structure and electrochemistry of LixMoO2. *Solid State Ionics* **23,** 1–7 (1987).
13. Whittingham, M. Electrical Energy Storage and Intercalation Chemistry. *Science* **192,** 1126–1127 (1976).
14. Mizushima, K. *et al.* LixCoO2 (0<x
1): A new cathode material for batteries of highe energy density. *Materials Reserach Bulletin* **15,** 783–789 (1980).
15. Yoshino, A. *et al. Secondary Battery* 1987.
16. Liu, Y. K. *et al.* Research Progresses of Liquid Electrolytes in Lithium-Ion Batteries. *Small* **19** (2023).

17. Gond, R. *et al.* Non-flammable liquid electrolytes for safe batteries. *Materials Horizons* **8,** 2913–2928 (2021).

18. Muralidharan, N. *et al.* Next-Generation Cobalt-Free Cathodes – A Prospective Solution to the Battery Industry's Cobalt Problem. *Advanced Energy Materials* **12** (2022).

19. Satyavani, T. V. *et al.* Methods of synthesis and performance improvement of lithium iron phosphate for high rate Li-ion batteries: A review. *Engineering Science and Technology, an International Journal* **19,** 178–188 (2016).

20. Wang, J. *et al.* A homogeneous intergrown material of LiMn2O4 and LiNi0.5Mn1.5O4 as a cathode material for lithium-ion batteries. *Journal of Materials Chemistry A* **3,** 2353–2360 (2015).

21. Guan, P. *et al.* Recent progress of surface coating on cathode materials for high-performance lithium-ion batteries. *Journal of Energy Chemistry* **43,** 220–235 (2020).

22. Märker, K. *et al.* Evolution of Structure and Lithium Dynamics in LiNi0.8Mn0.1Co0.1O2 (NMC811) Cathodes during Electrochemical Cycling. *Chemistry of Materials* **31,** 2545–2554 (2019).

23. Heenan, T. M. *et al.* Identifying the Origins of Microstructural Defects Such as Cracking within Ni-Rich NMC811 Cathode Particles for Lithium-Ion Batteries. *Advanced Energy Materials* **10** (2020).

24. Purwanto, A. *et al.* NCA cathode material: Synthesis methods and performance enhancement efforts. *Materials Research Express* **5** (2018).

25. Myung, S. T. *et al.* Nickel-Rich Layered Cathode Materials for Automotive Lithium-Ion Batteries: Achievements and Perspectives. *ACS Energy Letters* **2,** 196–223 (2017).

26. Goodenough, J. B. *et al.* The Li-ion rechargeable battery: A perspective. *Journal of the American Chemical Society* **135,** 1167–1176 (2013).

27. Tarascon, J.-M. *et al.* Issues and challenges facing rechargeable lithium batteries. *Nature,* 359–367 (2001).

28. Li, M. *et al.* 30 Years of Lithium-Ion Batteries. *Advanced Materials* **30** (2018).

29. Lin, D. *et al.* Reviving the lithium metal anode for high-energy batteries. *Nature Nanotechnology* **12,** 194–206 (2017).

30. Masias, A. *et al.* Elastic, plastic, and creep mechanical properties of lithium metal. *Journal of Materials Science* **54,** 2585–2600 (2019).

31. Ling, C. *et al.* Study of the electrochemical deposition of Mg in the atomic level: Why it prefers the non-dendritic morphology. *Electrochimica Acta* **76,** 270–274 (2012).

32. Dologlou, E. Self-Diffusion in solid lithium. *Glass Physics and Chemistry* **36,** 570–574 (2010).

33. Monroe, C. *et al.* The Effect of Interfacial Deformation on Electrodeposition Kinetics. *Journal of The Electrochemical Society* **151,** A880 (2004).

34. Monroe, C. *et al.* Dendrite Growth in Lithium/Polymer Systems. *Journal of The Electrochemical Society* **150,** A1377 (2003).

35. Brissot, C. *et al.* In Situ Concentration Cartography in the Neighborhood of Dendrites Growing in Lithium/Polymer-Electrolyte/Lithium Cells. *Journal of The Electrochemical Society* **146,** 4393–4400 (1999).

36. Chazalviel, J.-N. Electrochemical aspects of the generation of ramified metallic electrodeposits. *Physical Review A* **42,** 15 (1990).

37. Ely, D. R. *et al.* Heterogeneous Nucleation and Growth of Lithium Electrodeposits on Negative Electrodes. *Journal of The Electrochemical Society* **160,** A662–A668 (2013).

38. Bai, P. *et al.* Transition of lithium growth mechanisms in liquid electrolytes. *Energy and Environmental Science* **9,** 3221–3229 (2016).

39. Jana, A. *et al.* Lithium dendrite growth mechanisms in liquid electrolytes. *Nano Energy* **41,** 552–565 (2017).

40. Jana, A. *et al.* Electrochemomechanics of lithium dendrite growth. *Energy and Environmental Science* **12,** 3595–3607 (2019).

41. Pei, A. *et al.* Nanoscale Nucleation and Growth of Electrodeposited Lithium Metal. *Nano Letters* **17,** 1132–1139 (2017).

42. Zheng, G. *et al.* Interconnected hollow carbon nanospheres for stable lithium metal anodes. *Nature Nanotechnology* **9,** 618–623 (2014).

43. Tatsuma, T. *et al.* Inhibition effect of covalently cross-linked gel electrolytes on lithium dendrite formation. *Electrochimica Acta* **46,** 1201–1205 (2001).

44. Jagger, B. *et al.* Solid Electrolyte Interphases in Lithium Metal Batteries. *Joule* **7,** 2228–2244 (2023).

45. Zhang, X. *et al.* Pressure-Driven Interface Evolution in Solid-State Lithium Metal Batteries. *Cell Reports Physical Science* **1** (2020).

46. Verma, A. *et al.* Microstructure and Pressure-Driven Electrodeposition Stability in Solid-State Batteries. *Cell Reports Physical Science* **2,** 100301 (2021).

47. Shen, X. *et al.* How Does External Pressure Shape Li Dendrites in Li Metal Batteries? *Advanced Energy Materials* **11,** 1–9 (2021).

48. Fang, C. *et al.* Pressure-tailored lithium deposition and dissolution in lithium metal batteries. *Nature Energy* (2021).

49. Doux, J. M. *et al.* Stack Pressure Considerations for Room-Temperature All-Solid-State Lithium Metal Batteries. *Advanced Energy Materials* **10** (2020).

50. Wood, K. N. *et al.* Dendrites and pits: Untangling the complex behavior of lithium metal anodes through operando video microscopy. *ACS Central Science* **2,** 790–801 (2016).

51. Li, N. W. *et al.* Passivation of Lithium Metal Anode via Hybrid Ionic Liquid Electrolyte toward Stable Li Plating/Stripping. *Advanced Science* **4** (2017).

52. Shen, X. *et al.* The Failure of Solid Electrolyte Interphase on Li Metal Anode: Structural Uniformity or Mechanical Strength? *Advanced Energy Materials* **10** (2020).

53. Wang, M. *et al.* Effect of LiFSI Concentrations to Form Thickness- and Modulus-Controlled SEI Layers on Lithium Metal Anodes. *Journal of Physical Chemistry C* **122,** 9825–9834 (2018).

54. Hobold, G. M. *et al.* Beneficial vs. inhibiting passivation by the native lithium solid electrolyte interphase revealed by electrochemical Li+ exchange. *Energy and Environmental Science* (2023).

55. Peled, E. *et al.* Advanced Model for Solid Electrolyte Interphase Electrodes in Liquid and Polymer Electrolytes. *Journal of The Electrochemical Society* **144,** L208–L210 (1997).

56. Li, Y. *et al.* Atomic structure of sensitive battery materials and interfaces revealed by cryo–electron microscopy. *Science* **358,** 506–510 (2017).

57. Liu, Y. *et al.* Solubility-mediated sustained release enabling nitrate additive in carbonate electrolytes for stable lithium metal anode. *Nature Communications* **9** (2018).

58. Cao, X. *et al.* Monolithic solid–electrolyte interphases formed in fluorinated orthoformate-based electrolytes minimize Li depletion and pulverization. *Nature Energy* **4,** 796–805 (2019).

59. Yu, Z. *et al.* Molecular design for electrolyte solvents enabling energy-dense and long-cycling lithium metal batteries. *Nature Energy* **5,** 526–533 (2020).

60. Han, B. *et al.* Poor Stability of Li2CO3 in the Solid Electrolyte Interphase of a Lithium-Metal Anode Revealed by Cryo-Electron Microscopy. *Advanced Materials* **33,** 1–10 (2021).

61. Zachman, M. J. *et al.* Cryo-STEM mapping of solid–liquid interfaces and dendrites in lithium-metal batteries. *Nature* **560,** 345–349 (2018).

62. Pang, Q. *et al.* An In Vivo Formed Solid Electrolyte Surface Layer Enables Stable Plating of Li Metal. *Joule* **1,** 871–886 (2017).

63. Shadike, Z. *et al.* Identification of LiH and nanocrystalline LiF in the solid–electrolyte interphase of lithium metal anodes. *Nature Nanotechnology* (2021).

64. Peled, E. *et al.* Review—SEI: Past, Present and Future. *Journal of The Electrochemical Society* **164,** A1703–A1719 (2017).

65. Bedrov, D. *et al.* Li+ Transport and Mechanical Properties of Model Solid Electrolyte Interphases (SEI): Insight from Atomistic Molecular Dynamics Simulations. *Journal of Physical Chemistry C* **121,** 16098–16109 (2017).

66. Weadock, N. *et al.* Determination of mechanical properties of the SEI in sodium ion batteries via colloidal probe microscopy. *Nano Energy* **2,** 713–719 (2013).

67. Yoon, I. *et al.* Measurement of mechanical and fracture properties of solid electrolyte interphase on lithium metal anodes in lithium ion batteries. *Energy Storage Materials* **25,** 296–304 (2020).

68. McBrayer, J. D. *et al.* Mechanical studies of the solid electrolyte interphase on anodes in lithium and lithium ion batteries. *Nanotechnology* **32** (2021).

69. Zhang, Z. *et al.* Operando Electrochemical Atomic Force Microscopy of Solid-Electrolyte Interphase Formation on Graphite Anodes: The Evolution of SEI Morphology and Mechanical Properties. *ACS Applied Materials and Interfaces* **12,** 35132–35141 (2020).

70. Shin, H. *et al.* Component-structure-dependent elasticity of solid electrolyte interphase layer in Li-ion batteries: Experimental and computational studies. *Journal of Power Sources* **277,** 169–179 (2015).

71. Williams, B. P. *et al.* Li+Ion Transport at the Lithium Metal Anode: A Fundamental Picture and Future Perspectives. *Journal of Physical Chemistry C* **126,** 10644–10652 (2022).

72. Peled, E. *et al.* in *Handbook of Battery Materials* 419–456 (1998).

73. Sun, S. Y. *et al.* Understanding the transport mechanism of lithium ions in solid-electrolyte interphase in lithium metal batteries with liquid electrolytes. *Materials Today* **77,** 39–65 (2024).

74. Shi, S. *et al.* Direct calculation of Li-ion transport in the solid electrolyte interphase. *Journal of the American Chemical Society* **134,** 15476–15487 (2012).

75. Zhang, S. *et al.* Understanding lithium transport in SEI films: a nonequilibrium molecular dynamics simulation. *Molecular Simulation* **46,** 573–580 (2020).

76. Shi, S. *et al.* Defect thermodynamics and diffusion mechanisms in Li2CO 3 and implications for the solid electrolyte interphase in Li-ion batteries. *Journal of Physical Chemistry C* **117,** 8579–8593 (2013).

77. Lu, Y. *et al.* The timescale identification decoupling complicated kinetic processes in lithium batteries. *Joule* **6,** 1172–1198 (2022).

78. Leskes, M. *et al.* Surface-Sensitive NMR Detection of the Solid Electrolyte Interphase Layer on Reduced Graphene Oxide. *Journal of Physical Chemistry Letters* **8,** 1078–1085 (2017).

79. Zheng, J. *et al.* Regulating electrodeposition morphology of lithium: Towards commercially relevant secondary Li metal batteries. *Chemical Society Reviews* **49,** 2701–2750 (2020).

80. Harlow, J. E. *et al.* A Wide Range of Testing Results on an Excellent Lithium-Ion Cell Chemistry to be used as Benchmarks for New Battery Technologies. *Journal of The Electrochemical Society* **166,** A3031–A3044 (2019).

81. Cheng, Y. *et al.* Lithium Host:Advanced architecture components for lithium metal anode. *Energy Storage Materials* **38,** 276–298 (2021).

82. Park, S. H. *et al.* Toward high-performance anodeless batteries based on controlled lithium metal deposition: A review. *Journal of Materials Chemistry A* (2021).

83. Pande, V. *et al.* Computational Screening of Current Collectors for Enabling Anode-Free Lithium Metal Batteries. *ACS Energy Letters* **4,** 2952–2959 (2019).

84. Yan, K. *et al.* Selective deposition and stable encapsulation of lithium through heterogeneous seeded growth. *Nature Energy* **1** (2016).

85. Lewis, J. A. *et al.* The promise of alloy anodes for solid-state batteries. *Joule* (2022).

86. Lohrberg, O. *et al.* Benchmarking and Critical Design Considerations of Zero-Excess Li-Metal Batteries. *Advanced Functional Materials,* 2214891 (2023).

87. Lin, Y. *et al.* Impact of the fluorination degree of ether-based electrolyte solvents on Li-metal battery performance. *Journal of Materials Chemistry A* **12,** 2986–2993 (2023).

88. Weber, R. *et al.* Long cycle life and dendrite-free lithium morphology in anode-free lithium pouch cells enabled by a dual-salt liquid electrolyte. *Nature Energy* **4,** 683–689 (2019).

89. Cao, X. *et al.* Review—Localized High-Concentration Electrolytes for Lithium Batteries. *Journal of The Electrochemical Society* **168,** 010522 (2021).

90. Ren, X. *et al.* Enabling High-Voltage Lithium-Metal Batteries under Practical Conditions. *Joule* **3,** 1662–1676 (2019).

91. Kang, D. *et al.* Artificial Solid-Electrolyte Interphase for Lithium Metal Batteries. *Batteries and Supercaps* **4,** 445–455 (2021).

92. Kang, D. *et al.* Rearrange SEI with artificial organic layer for stable lithium metal anode. *Energy Storage Materials* **24,** 618–625 (2020).

93. Lin, D. *et al.* Conformal Lithium Fluoride Protection Layer on Three-Dimensional Lithium by Nonhazardous Gaseous Reagent Freon. *Nano Letters* **17,** 3731–3737 (2017).

94. Wang, L. *et al.* Long lifespan lithium metal anodes enabled by Al2O3 sputter coating. *Energy Storage Materials* **10,** 16–23 (2018).

95. Janek, J. *et al.* A solid future for battery development. *Nature Energy* **1** (2016).

96. Pasta, M. *et al.* 2020 roadmap on solid-state batteries. *JPhys Energy* **2** (2020).

97. Janek, J. *et al.* Challenges in speeding up solid-state battery development. *Nature Energy* (2023).

98. Yu, X. *et al.* Battery Safety: From Lithium-Ion to Solid-State Batteries. *Engineering* **21,** 9–14 (2023).

99. Banerjee, A. *et al.* Interfaces and Interphases in All-Solid-State Batteries with Inorganic Solid Electrolytes. *Chemical Reviews* **120,** 6878–6933 (2020).

100. Ning, Z. *et al.* Visualizing plating-induced cracking in lithium-anode solid-electrolyte cells. *Nature Materials* (2021).

101. Zhang, Q. *et al.* Sulfide-Based Solid-State Electrolytes: Synthesis, Stability, and Potential for All-Solid-State Batteries. *Advanced Materials* **31** (2019).

102. Xu, L. *et al.* Interfaces in Solid-State Lithium Batteries. *Joule* **2,** 1991–2015 (2018).

103. Famprikis, T. *et al.* Fundamentals of inorganic solid-state electrolytes for batteries. *Nature Materials* **18,** 1278–1291 (2019).

104. Koerver, R. *et al.* Chemo-mechanical expansion of lithium electrode materials-on the route to mechanically optimized all-solid-state batteries. *Energy and Environmental Science* **11,** 2142–2158 (2018).

105. Wang, M. *et al.* Correlating the interface resistance and surface adhesion of the Li metal-solid electrolyte interface. *Journal of Power Sources* **377,** 7–11 (2018).

106. Wenzel, S. *et al.* Interfacial reactivity and interphase growth of argyrodite solid electrolytes at lithium metal electrodes. *Solid State Ionics* **318,** 102–112 (2018).

107. Wu, J. *et al.* Reducing the thickness of solid-state electrolyte membranes for high-energy lithium batteries. *Energy & Environmental Science* **14,** 12–36 (2021).

108. Boaretto, N. *et al.* Lithium solid-state batteries: State-of-the-art and challenges for materials, interfaces and processing. *Journal of Power Sources* **502** (2021).

109. Chen, R. *et al.* The Thermal Stability of Lithium Solid Electrolytes with Metallic Lithium. *Joule* **4,** 812–821 (2020).

110. Berthier, C. *et al.* Microscopic Investigation of Ionic Conductivity in Alkali Metal Salts- Poly(ethylene oxide) Adducts. *Solid State Ionics,* 91–95 (1983).

111. Wu, F. *et al.* Polymer electrolytes and interfaces toward solid-state batteries: Recent advances and prospects. *Energy Storage Materials* **33,** 26–54 (2020).

112. Liu, Q. *et al.* Challenges and perspectives of garnet solid electrolytes for all solid-state lithium batteries. *Journal of Power Sources* **389,** 120–134 (2018).

113. Ohta, S. *et al.* High lithium ionic conductivity in the garnet-type oxide Li7-X La3(Zr2-X, NbX)O12 (X = 0-2). *Journal of Power Sources* **196,** 3342–3345 (2011).

114. Li, X. *et al.* Air-stable Li3InCl6 electrolyte with high voltage compatibility for all-solid-state batteries. *Energy and Environmental Science* **12,** 2665–2671 (2019).

115. Bates, J. B. *et al.* Fabrication and characterization of amorphous lithium electrolyte thin films and rechargeable thin-film batteries. *Journal of Power Sources,* 103 (1993).

116. Minnmann, P. *et al.* Editors' Choice—Quantifying the Impact of Charge Transport Bottlenecks in Composite Cathodes of All-Solid-State Batteries. *Journal of The Electrochemical Society* **168,** 040537 (2021).

117. Kim, S. *et al.* Thin Solid Electrolyte Separators for Solid-State Lithium-Sulfur Batteries. *Nano Letters* **22,** 10176–10183 (2022).

118. Shin, B. R. *et al.* Comparative study of TiS2/Li-In all-solid-state lithium batteries using glass-ceramic Li3PS4and Li10GeP2S12 solid electrolytes. *Electrochimica Acta* **146,** 395–402 (2014).

119. Yu, S. *et al.* Elastic Properties of the Solid Electrolyte Li7La3Zr2O12 (LLZO). *Chemistry of Materials* **28,** 197–206 (2016).

120. Zhu, Y. *et al.* Origin of Outstanding Stability in the Lithium Solid Electrolyte Materials: Insights from Thermodynamic Analyses Based on First-Principles Calculations. *ACS Applied Materials and Interfaces* **7,** 23685–23693 (2015).

121. Lau, J. *et al.* Sulfide Solid Electrolytes for Lithium Battery Applications. *Advanced Energy Materials* **8** (2018).

122. Kamaya, N. *et al.* A lithium superionic conductor. *Nature Materials* **10,** 682–686 (2011).

123. Deiseroth, H. J. *et al.* Li6PS5X: A class of crystalline Li-rich solids with an unusually high Li+ mobility. *Angewandte Chemie - International Edition* **47,** 755–758 (2008).

124. Wenzel, S. *et al.* Direct Observation of the Interfacial Instability of the Fast Ionic Conductor Li10GeP2S12 at the Lithium Metal Anode. *Chemistry of Materials* **28,** 2400–2407 (2016).

125. Otto, S.-K. *et al.* In Situ Investigation of Lithium Metal-Solid Electrolyte Anode Interfaces with ToF-SIMS. *Advanced Materials Interfaces,* 2102387 (2022).

126. Hanghofer, I. *et al.* Substitutional disorder: Structure and ion dynamics of the argyrodites Li6PS5Cl, Li6PS5Br and Li6PS5I. *Physical Chemistry Chemical Physics* **21,** 8489–8507 (2019).

127. Adeli, P. *et al.* Boosting Solid-State Diffusivity and Conductivity in Lithium Superionic Argyrodites by Halide Substitution. *Angewandte Chemie* **131,** 8773–8778 (2019).

128. Adeli, P. *et al.* Influence of Aliovalent Cation Substitution and Mechanical Compression on Li-Ion Conductivity and Diffusivity in Argyrodite Solid Electrolytes. *Chemistry of Materials* **33,** 146–157 (2021).

129. Guo, H. *et al.* High-entropy sulfide argyrodite electrolytes for all-solid-state lithium-sulfur batteries. *Cell Reports Physical Science* **5,** 102228 (2024).

130. Van der Maas, E. *et al.* Investigation of Structure, Ionic Conductivity, and Electrochemical Stability of Halogen Substitution in Solid-State Ion Conductor Li3YBrxCl6-x. *Journal of Physical Chemistry C* **127,** 125–132 (2023).

131. Tan, D. H. *et al.* Elucidating Reversible Electrochemical Redox of Li6PS5Cl Solid Electrolyte. *ACS Energy Letters,* 2418–2427 (2019).

132. Balaish, M. *et al.* Processing thin but robust electrolytes for solid-state batteries. *Nature Energy* **6,** 227–239 (2021).

133. Li, J. *et al.* Processing-structure-property relationships in practical thin solid-electrolyte separators for all-solid-state batteries. *JPhys Energy* **6** (2024).

134. Riegger, L. M. *et al.* Evolution of the Interphase between Argyrodite-Based Solid Electrolytes and the Lithium Metal Anode-The Kinetics of Solid Electrolyte Interphase Growth. *Chemistry of Materials* **35,** 5091–5099 (2023).

135. Aktekin, B. *et al.* SEI growth on Lithium metal anodes in solid-state batteries quantified with coulometric titration time analysis. *Nature Communications* **14** (2023).

136. Simon, F. J. *et al.* Development of a Wire Reference Electrode for Lithium All-Solid-State Batteries with Polymer Electrolyte: FEM Simulation and Experiment. *Journal of The Electrochemical Society* **165,** A1363–A1371 (2018).

137. Koh, H. *et al.* Understanding Ion-Beam Damage to Air-Sensitive Lithium Metal With Cryogenic Electron and Ion Microscopy. *Microscopy and Microanalysis* **29,** 1350–1356 (2023).

138. Tsukasaki, H. *et al.* Deterioration process of argyrodite solid electrolytes during exposure to humidity-controlled air. *Journal of Power Sources* **524** (2022).

139. Narayanan, S. *et al.* Effect of current density on the solid electrolyte interphase formation at the lithium-Li6PS5Cl interface. *Nature Communications* **13,** 7237 (2022).

140. Du, F. *et al.* Room-temperature, all-solid-state lithium metal batteries enabled by a moderate-temperature formation method. *Journal of Materials Science* **57,** 1271–1280 (2022).

141. Lee, J. Z. *et al.* Cryogenic Focused Ion Beam Characterization of Lithium Metal Anodes. *ACS Energy Letters* **4,** 489–493 (2019).

142. Porz, L. *et al.* Mechanism of Lithium Metal Penetration through Inorganic Solid Electrolytes. *Advanced Energy Materials* **7** (2017).

143. Kazyak, E. *et al.* Li Penetration in Ceramic Solid Electrolytes: Operando Microscopy Analysis of Morphology, Propagation, and Reversibility. *Matter* **2,** 1025–1048 (2020).

144. Choudhary, K. *et al.* Operando X-ray diffraction in transmission geometry « at home » from tape casted electrodes to all-solid-state battery. *Journal of Power Sources* **553** (2023).

145. Hao, S. *et al.* 3D Imaging of Lithium Protrusions in Solid-State Lithium Batteries using X-Ray Computed Tomography. *Advanced Functional Materials* **31** (2021).

146. Hao, S. *et al.* Tracking lithium penetration in solid electrolytes in 3D by in-situ synchrotron X-ray computed tomography. *Nano Energy* **82** (2021).

147. Wu, X. *et al.* Operando Visualization of Morphological Dynamics in All-Solid-State Batteries. *Advanced Energy Materials* **9** (2019).

148. Scharf, J. *et al.* Bridging nano- and microscale X-ray tomography for battery research by leveraging artificial intelligence. *Nature Nanotechnology* **17,** 446–459 (2022).

149. Krauskopf, T. *et al.* The Fast Charge Transfer Kinetics of the Lithium Metal Anode on the Garnet-Type Solid Electrolyte Li6.25Al0.25La3Zr2O12. *Advanced Energy Materials* **10** (2020).

150. McConohy, G. *et al.* Mechanical regulation of lithium intrusion probability in garnet solid electrolytes. *Nature Energy* **8,** 241–250 (2023).

151. Nagao, M. *et al.* In situ SEM study of a lithium deposition and dissolution mechanism in a bulk-type solid-state cell with a Li2S-P2S5 solid electrolyte. *Physical Chemistry Chemical Physics* **15,** 18600–18606 (2013).

152. Burnett, T. L. *et al.* Large volume serial section tomography by Xe Plasma FIB dual beam microscopy. *Ultramicroscopy* **161,** 119–129 (2016).

153. Siniscalchi, M. *et al.* Initiation of dendritic failure of LLZTO via sub-surface lithium deposition. *Energy and Environmental Science* **17,** 2431–2440 (2024).

154. Luo, S. *et al.* Nanostructure of the Interphase Layer between a Single Li Dendrite and Sulfide Electrolyte in All-Solid-State Li Batteries. *ACS Energy Letters,* 3064–3071 (2022).

155. Lewis, J. A. *et al.* Interphase Morphology between a Solid-State Electrolyte and Lithium Controls Cell Failure. *ACS Energy Letters* **4,** 591–599 (2019).

156. Sheng, O. *et al.* In Situ Construction of a LiF-Enriched Interface for Stable All-Solid-State Batteries and its Origin Revealed by Cryo-TEM. *Advanced Materials* **32** (2020).

157. Cheng, D. *et al.* Unveiling the Stable Nature of the Solid Electrolyte Interphase between Lithium Metal and LiPON via Cryogenic Electron Microscopy. *Joule* **4,** 2484–2500 (2020).

158. Alt, C. D. *et al.* Quantifying multiphase SEI growth in sulfide solid electrolytes. *Joule* (2024).

159. Wood, K. N. *et al.* Operando X-ray photoelectron spectroscopy of solid electrolyte interphase formation and evolution in Li2S-P2S5 solid-state electrolytes. *Nature Communications* **9** (2018).

160. Lombardo, T. *et al.* Bridging the Gap: Electrode Microstructure and Interphase Characterization by Combining ToF-SIMS and Machine Learning. *Advanced Materials Interfaces* **10** (2023).

161. Walther, F. *et al.* Visualization of the Interfacial Decomposition of Composite Cathodes in Argyrodite-Based All-Solid-State Batteries Using Time-of-Flight Secondary-Ion Mass Spectrometry. *Chemistry of Materials* **31,** 3745–3755 (2019).

162. Zheng, C. *et al.* Unprecedented Self-Healing Effect of Li6PS5Cl-Based All-Solid-State Lithium Battery. *Small* **17** (2021).

163. Zhou, Y. *et al.* Observation of Interfacial Degradation of Li6PS5Cl against Lithium Metal and LiCoO2 via In Situ Electrochemical Raman Microscopy. *Batteries and Supercaps* **3,** 647–652 (2020).

164. Tan, J. *et al.* A Growing Appreciation for the Role of LiF in the Solid Electrolyte Interphase. *Advanced Energy Materials* **11** (2021).

165. Aspinall, J. *et al.* The impact of magnesium content on lithium-magnesium alloy electrode performance with argyrodite solid electrolyte. *Nature Communications* **15,** 4511 (2024).

166. Aspinall, J. *et al.* Effect of Microstructure on the Cycling Behavior of Li-In Alloy Anodes for Solid-State Batteries. *ACS Energy Letters* **9,** 578–585 (2024).

167. Goodhew, P. J. *et al. Electron Microscopy and Analysis* Third (Taylor & Francis, London, 2001).

168. Goldstein, J. *et al. Scanning Electron Microscopy and X-Ray Microanalysis* Third (Springer Science & Business Media, 2003).

169. Williams, D. B. *et al. Transmission Electron Microscopy* (Springer US, Boston, MA, 2009).

170. Nellist, P. *et al.* Incoherent imaging using dynamically scattered coherent electrons. *Ultramicroscopy* **78,** 111–124 (1999).

171. Barnaby, • . *et al.* 4D STEM with a direct electron detector.

172. Ophus, C. Four-Dimensional Scanning Transmission Electron Microscopy (4D-STEM): From Scanning Nanodiffraction to Ptychography and Beyond. *Microscopy and Microanalysis* (2019).

173. Li, G. *et al.* 4D-STEM Ptychography for Electron-Beam-Sensitive Materials. *ACS Central Science* **8,** 1579–1588 (2022).

174. Savitzky, B. H. *et al.* py4DSTEM : A Software Package for Four-Dimensional Scanning Transmission Electron Microscopy Data Analysis. *Microscopy and Microanalysis* **27,** 712–743 (2021).

175. *Introduction to focused ion beams : instrumentation, theory, techniques and practice* (eds Giannuzzi, L. A. *et al.*) (Springer-Science + Business Media Inc., New York, 2010).

176. Arey, B. *et al.* Advantages of using Plasma FIB Over a Gallium LMIS Source. *Microscopy and Microanalysis* **21,** 2001–2002 (2015).

177. Townsend, P. D. Ion implantation and integrated optics. *Journal of Physics E: Scientific Instruments* **10,** 197–203 (1977).

178. Nastasi, M. *et al. Ion-Solid Interactions: Fundamentals and Applications* (Cambridge University Press, Cambridge).

179. Dubochet, J. On the Development of Electron Cryo-Microscopy (Nobel Lecture). *Angewandte Chemie International Edition* **57,** 10842–10846 (2018).

180. Wang, X. *et al.* Cryogenic Electron Microscopy for Characterizing and Diagnosing Batteries. *Joule* **2,** 2225–2234 (2018).

181. Talmon, Y. Thermal and radiation damage to frozen hydrated specimens. *Journal of Microscopy* **125,** 227–237 (1982).

182. Egerton, R. F. Radiation damage to organic and inorganic specimens in the TEM. *Micron* **119,** 72–87 (2019).

183. Chen, Q. *et al.* Imaging Beam-Sensitive Materials by Electron Microscopy. *Advanced Materials* **32** (2020).

184. Jiang, N. Electron beam damage in oxides: A review. *Reports on Progress in Physics* **79** (2015).

185. Egerton, R. F. Control of radiation damage in the TEM. *Ultramicroscopy* **127,** 100–108 (2013).

186. Egerton, R. F. Mechanisms of radiation damage in beam-sensitive specimens, for TEM accelerating voltages between 10 and 300 kV. *Microscopy Research and Technique* **75,** 1550–1556 (2012).

187. Michael, J. R. *Gallium phase formation in Cu during 30kV Ga+ FIB milling* in *Microscopy and Microanalysis* **12** (2006), 1248–1249.

188. Thompson, K. *et al. Minimization of Ga induced FIB damage using low energy clean-up* in *Microscopy and Microanalysis* **12** (2006), 1736–1737.

189. Mayer, J. *et al.* TEM Sample Preparation and FIB-Induced Damage. *MRS Bulletin* **32** (2007).

190. Lazanas, A. C. *et al.* Electrochemical Impedance Spectroscopy-A Tutorial. *ACS Measurement Science Au* (2022).

191. Lee, H. J. *et al.* LiNi0.5Mn1.5O4Cathode Microstructure for All-Solid-State Batteries. *Nano Letters* **22,** 7477–7483 (2022).

192. Sun, Y. *et al.* Visualizing the Li distribution in an all-solid-state battery composite electrode using combined plasma focused-ion beam microscopy and secondary-ion mass spectroscopy. *Micron* **190,** 103746 (2025).

193. Shi, T. *et al.* Characterization of mechanical degradation in an all-solid-state battery cathode. *Journal of Materials Chemistry A* **8,** 17399–17404 (2020).

194. Gong, Y. *et al.* Three-dimensional atomic-scale observation of structural evolution of cathode material in a working all-solid-state battery. *Nature Communications* **9** (2018).

195. Perrenot, P. *et al.* Operando Focused Ion Beam-Scanning Electron Microscope (FIB-SEM) Revealing Microstructural and Morphological Evolution in a Solid-State Battery. *ACS Energy Letters* **9,** 3835–3840 (2024).

196. Kelley, R. *et al.* Xe+ FIB Milling and Measurement of Amorphous Silicon Damage. *Microscopy and Microanalysis* **19,** 862–863 (2013).

197. Fuchs, T. *et al.* Imaging the microstructure of lithium and sodium metal in anode-free solid-state batteries using electron backscatter diffraction. *Nature Materials* (2024).

198. Fuchs, T. *et al.* Current-Dependent Lithium Metal Growth Modes in "Anode-Free" Solid-State Batteries at the Cu-LLZO Interface. *Advanced Energy Materials* **13** (2023).

199. Wang, Y. *et al.* Stable Anode-Free All-Solid-State Lithium Battery through Tuned Metal Wetting on the Copper Current Collector. *Advanced Materials* **35** (2023).

200. Su, J. *et al.* Interfacial modification between argyrodite-type solid-state electrolytes and Li metal anodes using LiPON interlayers. *Energy and Environmental Science* **15,** 3805–3814 (2022).

201. Wang, M. J. *et al.* Enabling "lithium-free" manufacturing of pure lithium metal solid-state batteries through in situ plating. *Nature Communications* **11** (2020).

202. Zhang, Z. *et al.* Interface Re-Engineering of Li10GeP2S12 Electrolyte and Lithium anode for All-Solid-State Lithium Batteries with Ultralong Cycle Life. *ACS Applied Materials and Interfaces* **10,** 2556–2565 (2018).

203. Wang, Y. *et al.* Mechanical Milling – Induced Microstructure Changes in Argyrodite LPSCl Solid-State Electrolyte Critically Affect Electrochemical Stability. *Advanced Energy Materials* (2024).

204. Michael, J. R. *et al.* Focused Ion Beam Preparation of Low Melting Point Metals: Lessons Learned From Indium. *Microscopy and Microanalysis* **28,** 603–610 (2022).

205. Seymour, I. D. *et al.* Suppressing void formation in all-solid-state batteries: the role of interfacial adhesion on alkali metal vacancy transport. *Journal of Materials Chemistry A* **9,** 19901–19913 (2021).

206. Aspinall, J. *et al.* EBSD-coupled indentation: nanoscale mechanics of lithium metal. *Materials Today Energy* **30** (2022).

207. Cain, T. W. *et al.* The development of β phase Mg–Li alloys for ultralight corrosion resistant applications. *npj Materials Degradation* **4,** 17 (2020).

208. Hänsel, C. *et al.* The Stack Pressure Dilemma in Sulfide Electrolyte Based Li Metal Solid-State Batteries : A Case Study with Li6PS5Cl Solid Electrolyte. *Advanced Materials Interfaces* **2100206,** 1–7 (2021).

209. Shin, D. *et al.* Preferential Lithium Plating in the Interfacial Void Region in All-Solid-State Batteries via Pressure Gradient-Driven Lithium-Ion Flux. *ACS Energy Letters,* 1035–1042 (2024).

210. Santhosha, A. L. *et al.* The Indium-Lithium Electrode in Solid-State Lithium-Ion Batteries: Phase Formation, Redox Potentials, and Interface Stability. *Batteries & Supercaps* **2,** 524–529 (2019).

211. Jing, W. *et al.* Li-Indium alloy anode for high-performance Li-metal batteries. *Journal of Alloys and Compounds* **924,** 166517 (2022).

212. Ziegler, J. F. *et al.* SRIM – The stopping and range of ions in matter (2010). *Nuclear Instruments and Methods in Physics Research Section B: Beam Interactions with Materials and Atoms* **268,** 1818–1823 (2010).

213. Mallakpour, F. *et al.* Length-scale-dependent stress relief mechanisms in indium at high homologous temperatures. *Journal of Materials Research* **36,** 2444–2455 (2021).

214. Riphaus, N. *et al.* Slurry-Based Processing of Solid Electrolytes: A Comparative Binder Study. *Journal of The Electrochemical Society* **165,** A3993–A3999 (2018).

215. Schneider, C. A. *et al.* NIH Image to ImageJ: 25 years of image analysis. *Nature Methods* **9,** 671–675 (2012).

216. Gorman, B. *et al.* FIB / FESEM Investigations of Polymer / Inorganic Composites. *Microscopy and Microanalysis* **12,** 1000–1001 (2006).

217. Cao, D. *et al.* Lithium Dendrite in All-Solid-State Batteries: Growth Mechanisms, Suppression Strategies, and Characterizations. *Matter* **3,** 57–94 (2020).

218. Lee, Y. G. *et al.* High-energy long-cycling all-solid-state lithium metal batteries enabled by silver–carbon composite anodes. *Nature Energy* **5,** 299–308 (2020).

219. Spencer-Jolly, D. *et al.* Structural changes in the silver-carbon composite anode interlayer of solid-state batteries. *Joule* (2023).

220. Pang, B. *et al.* Ag nanoparticles incorporated interlayer enables ultrahigh critical current density for Li6PS5Cl-based all-solid-state lithium batteries. *Journal of Power Sources* **563,** 232836 (2023).

221. Wu, C. *et al.* Understanding the Chemomechanical Function of the Silver–Carbon Interlayer in Sheet-type All-Solid-State Lithium–Metal Batteries. *Nano Letters* **23,** 4415–4422 (2023).

222. Wang, Z. *et al.* Lithium anode interlayer design for all-solid-state lithium-metal batteries. *Nature Energy* **9,** 251–262 (2024).

223. Zhang, Z. *et al.* Capturing the swelling of solid-electrolyte interphase in lithium metal batteries. *Science* **375,** 66–70 (2022).

224. Zhang, X. *et al.* Cryo-ultramicrotomy enables TEM characterization of global lithium/polymer interfaces. *Energy & Environmental Science* **17,** 1436–1447 (2024).

225. Parmenter, C. D. *et al.* Cryo-FIB-lift-out: practically impossible to practical reality. *Journal of Microscopy* **281,** 157–174 (2021).

226. Vitale, S. M. *et al.* Using Xe Plasma FIB for High-Quality TEM Sample Preparation. *Microscopy and Microanalysis* **28,** 646–658 (2022).

227. Wang, Z. *et al.* Revealing the Distribution of Lithium Compounds in Lithium Dendrites by Four-Dimensional Electron Microscopy Analysis. *Nano Letters* (2024).

228. Hugenschmidt, M. *et al.* Low-Dose 4D-STEM Tomography for Beam-Sensitive Nanocomposites. *ACS Materials Letters* **6,** 165–173 (2024).

229. Bustillo, K. C. *et al.* 4D-STEM of Beam-Sensitive Materials. *Accounts of Chemical Research* **54,** 2543–2551 (2021).

230. Liang, Y. *et al.* In situ XPS investigation of the SEI formed on LGPS and LAGP with metallic lithium. *Chemical Communications* (2024).

231. Burton, M. *et al.* The Role of Phosphorous in the Solid Electrolyte Interphase of Argyrodite Solid Electrolytes (2024).

232. Wenzel, S. *et al.* Interphase formation and degradation of charge transfer kinetics between a lithium metal anode and highly crystalline Li7P3S11 solid electrolyte. *Solid State Ionics* **286,** 24–33 (2016).

233. Graham, D. J. *et al.* Information from complexity: Challenges of TOF-SIMS data interpretation. *Applied Surface Science* **252,** 6860–6868 (2006).

234. Hood, Z. D. *et al.* Elucidating Interfacial Stability between Lithium Metal Anode and Li Phosphorus Oxynitride via in Situ Electron Microscopy. *Nano Letters* **21,** 151–157 (2021).

235. Wang, C.-M. *et al.* Ab initio Study on Lithium Anode Interface Instability and Stabilization of Superionic Li3InCl6 and Li6PS5Cl Solid Electrolytes. *arxiv* (2024).

236. Gražulis, S. *et al.* Crystallography Open Database – an open-access collection of crystal structures. *Journal of Applied Crystallography* **42,** 726–729 (2009).

237. Wantanabe, M. *et al.* Analysis of Spectrum-Imaging Datasets in Atomic-Resolution Electron Microscopy. *Microscopy and Microanalysis* **23,** 5–7 (2009).

238. Ryu, J. *et al.* Dimensionality reduction and unsupervised clustering for EELS-SI. *Ultramicroscopy* **231** (2021).

239. Uesugi, F. *et al.* Non-negative matrix factorization for mining big data obtained using four-dimensional scanning transmission electron microscopy. *Ultramicroscopy* **221** (2021).

240. Shiga, M. *et al.* Sparse modeling of EELS and EDX spectral imaging data by nonnegative matrix factorization. *Ultramicroscopy* **170,** 43–59 (2016).

241. Peters, J. J. P. *et al.* Event-responsive scanning transmission electron microscopy. *Science* **385,** 549–553 (2024).

242. Aidukas, T. *et al.* High-performance 4-nm-resolution X-ray tomography using burst ptychography. *Nature* **632,** 81–88 (2024).

243. Savitzky, B. H. *et al.* Accuracy, Reproducibility, and Calibration in 4D-STEM. *Microscopy and Microanalysis* **28,** 470–472 (2022).

244. Fairley, N. *et al.* Systematic and collaborative approach to problem solving using X-ray photoelectron spectroscopy. *Applied Surface Science Advances* **5,** 100112 (2021).

245. OpenAI. *ChatGPT* 2024.